Title
Synthesis and Characterization of Poly(3-alkylthiophene)-containing Block Copolymers

Author
Ho, Victor

Publication Date
2014

Synthesis and Characterization of Poly(3-alkylthiophene)-containing Block Copolymers

by

Victor Ho

A dissertation submitted in partial satisfaction of the

requirements for the degree of

Doctor of Philosophy

in

Chemical Engineering

in the

Graduate Division

of the

University of California, Berkeley

Committee in charge:

Professor Rachel A. Segalman, Chair
Professor Nitash P. Balsara
Professor Ana Claudia Arias

Spring 2014

Synthesis and Characterization of Poly(3-alkylthiophene)-containing Block Copolymers

By Victor Ho

Abstract

Synthesis and Characterization of Poly(3-alkylthiophene)-containing Block Copolymers

by

Victor Ho

Doctor of Philosophy in Chemical Engineering

University of California, Berkeley

Professor Rachel A. Segalman, Chair

Conjugated polymers have been widely studied for their use in lightweight, flexible, and solution-processable electronic devices. However, the optimization of such polymer-based devices has been largely Edisonian in nature due to both a poor understanding of and an inability to control the complex hierarchical structure observed in semicrystalline polymers. In this thesis, we show that simple chemical modifications to commonly-studied conjugated polymers can have a large effect on the observed structure ranging from the unit cell to that on the order of device features. In particular, the self-assembly of block copolymers in which one of the components is optoelectronically-active is presented as a facile method to obtain nanostructured materials. For the work in this thesis, we will focus on poly(3-alkylthiophenes), a widely studied class of conjugated polymers due to their favorable optoelectronic properties, high solubility in organic solvents, and susceptibility to simple chemical modification.

Although the synthesis of conjugated block copolymers has been presented in the past, complexities arising from crystallization of the conjugated moiety have dominated the observed solid state morphologies. Specifically, the crystallization of the semicrystalline block dictates the block copolymer microphase separation, a well-known phenomenon in the literature for non-conjugated semicrystalline block copolymers, which has resulted in solid state morphologies that do not differ significantly from that of the semiconducting homopolymer. To address this, we first show that the side chain chemistry controls the thermal transitions and optoelectronic properties in poly(3-alkylthiophenes). Such control over the crystallization kinetics provides an experimentally convenient approach to investigate the importance of the crystalline structure over a wide range of length scales on the optoelectronic properties. Furthermore, the ability to control the thermal transition temperatures can be used to directly manipulate, and thereby balance, the competition between the driving forces for crystallization and self-assembly. As evidence, the nanoscale structure is shown to be directly controlled via synthesis of block copolymers in which one block is the low melting temperature semiconducting polymer, poly(3-(2-ethylhexyl)thiophene). A wide range of morphologies with curved interfaces are observed which, in the past, have been precluded by the crystallization of poly(3-alkylthiophenes) with unbranched aliphatic side chains such as poly(3-hexylthiophene). Importantly, confinement of the conjugated polymer to nanoscale domains is not detrimental to the crystallinity or to charge transport over device-scale dimensions. Additionally, this approach is shown to be effective for a

number of different chemistries providing a flexible methodology for obtaining periodic, semiconducting domains on the nanoscale. Together, these simple synthetic strategies can be used to tune the morphology of various length scales of thin film active layers and provide synthetic rules for design of novel semiconducting polymer systems.

Table of Contents

List of Figures

List of Tables

Chapter 1: Introduction

Nanostructuring organic electronics has been proposed as an approach to potentially improve the operation of devices. As the physics of relevant physical processes span length scales ranging from the ångström to the micron, it is important to provide predictive design rules for structure-property relationships and approaches to control the morphology at all of these length scales. Block copolymers in which at least one of the components is semiconducting provides the opportunity to predictively nanostructure organic electronic active layers using only the chemistry of the macromolecule and simple processing techniques. However, this approach is complicated by the non-ideal melt phase structure of many conjugated polymers and the propensity for these molecules to undergo crystallization above room temperature.

In this chapter, we first briefly present physical processes fundamental to the operation of organic electronic devices. The importance of structural control over length scales ranging from ångströms to hundreds of nanometers will be evident, and the case will be made for using functional block copolymers as nanopatterned organic electronic active layers. However, challenges in the self-assembly of semiconducting block copolymers persist in this relatively nascent field and these will be discussed in detail.

1.1 Role of Morphology on Charge Transport

Organic electronics are attractive for their potential role as light-weight and flexible devices which can be fabricated from low-cost raw materials using well-established processing techniques. Organic semiconductors, unlike their non-conjugated counterparts, rely on the delocalization of π-electrons over length scales larger than that of a single molecule or monomeric repeat unit. Typically, this delocalization is effected through the synthesis of conjugated aromatic units which results in rigid, planar molecules that are frequently (semi)crystalline. Molecules can be either small molecules or polymeric; those that will be discussed in this chapter, which form only a small subset of commonly-studied materials, are presented in Figure 1.

While many organic complex optoelectronic devices have been developed or proposed, including thermoelectric modules, electrochemical light emitting diodes, and emitting field effect transistors, we will focus on the fundamental processes that govern the operation of more traditional architectures, in particular thin film field-effect transistors (FETs) and photovoltaics (PVs). Though this decision appears to restrict the scope of this thesis, a fundamental understanding of important structure-property relationships in these devices can be broadly applied to more complex geometries and architectures. Importantly, it will be clear that the physical processes in these systems are inherently tied to the structure ranging from the molecular through that of device dimensions. Specifically, charge transport in organic systems relies on the electronic coupling between adjacent molecules while simultaneously depending on the mesoscale structure for transport between electrodes. Similarly, the absorption of light in organic PV devices is dictated by the molecular and crystalline structure while splitting of the exciton requires consideration of the morphology at the 10-100 nm length scale. These processes and their specific relationship to structure at multiple length scales will be discussed in detail.

Polythiophene Poly(phenylene vinylene) Polyacetylene Polyfluorene

Pentacene Poly(2,5-bis(3-alkylthiophen-2-yl)thieno[3,2,-b]thiophene) (PBTTT)

Figure 1.1: Chemical structures of common conjugated organic molecules

Chemical structures of conjugated small molecules and polymers discussed in this chapter. For polymers, delocalization over the molecule results in mostly planar molecules with relatively large persistence lengths. In most cases, alkyl side chains which are commonly introduced to effect solubility in these molecules have been excluded for generality.

1.1.1 Charge transport

Charge transport is among the most fundamental processes in organic electronics. From high conductivities in accumulation layers of OFETs to efficient collection of free charge carriers in OPVs, the transport of holes and/or electrons is a crucial process in most organic electronic devices. As such, understanding the role of structure on charge transport at dimensions ranging from the molecular through that of device features has been intensely studied for many years. Although charge transport is well-understood in inorganic single crystals, structural disorder at multiple length scales, inherent in most organic small molecules and polymeric semiconductors, result in deviations from idealized, band-like transport.

At the molecular length scale to that of the crystalline unit cell, charge transport is dictated by the strength of interaction between neighboring molecules. While in inorganic semiconductors and metals, atoms in periodic structures are held together with covalent bonds, organic crystals interact through van der Waals interactions between neighboring molecules. In spite of the significantly lower strength of these interactions, at sufficiently low temperatures conjugated small molecules have been known to exhibit band-like transport. Schein *et al.* presented the first evidence of a hopping-band transition upon cooling single crystalline naphthalene to sub-77K temperatures.[1] As evidence of the transition, time of flight mobility measurements showed that upon freezing out many of the phonon modes and intramolecular vibrations the measured mobilities increased exponentially. At higher temperatures (>150K) scattering from lattice phonons decrease the contribution from this band-like motion and transport in the higher temperature regime was dominated by a very weakly thermally-activated process. Since this discovery, band-like transport has been observed in other materials using either temperature-dependent mobility[2-5] or Hall effect[6-7] measurements in addition to transient photoconductivity[1,8] techniques.

While the transport in the low temperature (band-like regime) can be understood in the context of conventional solid-state physics, as bandwidths decrease below approximately 0.1 eV[9] charge carriers are localized and transport is commonly described according to Marcus theory. In this theory, developed in 1956 for electron transfer of redox reactions in solution,[10] the self-exchange rates can be parameterized by the transfer integral, t, the reorganization energy, λ, and the change in the Gibbs free energy upon transfer (which is zero for transfer between energetically equivalent sites), $\Delta G°$,

$$k_{et} = \frac{4\pi^2}{h} t^2 \frac{1}{\sqrt{4\pi\lambda kT}} \exp\left[-\frac{\left(\lambda + \Delta G^\circ\right)^2}{4\lambda kT} \right] \tag{1.1}$$

The exchange rate is related to the mobility through the Einstein relation[11]

$$\mu \sim \frac{ea^2}{k_B T} k_{et} \tag{1.2}$$

where e is the charge of an electron and a is the transport distance. It can be seen from these equations that optimization of the charge mobility requires increasing the transfer integral and minimization of the reorganization energy. The former is defined as the matrix element of the linear operator describing intermolecular interactions acting on the wavefunctions for the charge-localized states of adjacent sites and can be quantified from first principles knowing the crystal structure of the solid. The latter physically describes both the degree of nuclear rearrangement of the molecules and the polarization of the surroundings upon electron transfer.[12-13] In this regime, it can be seen that the charge carrier mobility is dependent on parameters which are defined by the structure at the crystalline/molecular length scale and has been shown to be relevant to device performance.

It has been shown in conjugated polymers that in addition to thermally induced disorder which induces a band-hopping transition, static disorder can be present[14] which can be described by the degree of paracrystalline disorder.[15-16] This disorder results in the loss of correlations over relatively short distances in some organic systems such as poly(3-hexylthiophene) (P3HT) and poly(2,5-bis(3-tetradecylthiophen-2-yl)thieno[3,2,-b]thiophene) (PBTTT), and consequently introduces trap states within the band gap. A correlation between the presence of trap states with the charge transport is evident from the data, indicating that in these organic systems, the additional disorder within the crystalline domains can affect the charge mobility.[16]

While the mechanism for charge transport is necessarily dependent on the crystalline structure and disorder within, only in single crystal devices are these effects solely responsible for measured properties. Solution-processed devices will be polycrystalline, and the presence of grain boundaries and amorphous regions provide further barriers for charge transport that can in some instances dominate transport. A high angle grain boundary, one in which the angle between molecules in adjacent crystals is large, results in an inherently lower transfer integral at the boundary. Decreasing the misorientation across the boundary results in a lower activation barrier for electron hopping, and lower probability for disordered regions bridging domains.[14] Interestingly, it has been postulated[17] that although the intracrystalline transfer integral for a herringbone crystal structure is lower than a slip-stack, high-angle grain boundaries are less detrimental such that polycrystalline active layers may benefit from these packings. This concept underscores the connection between the crystalline and mesoscale structure for the overall device performance.

These mesoscale contributions are further complicated in conjugated polymers by the structural heterogeneity which results from the inherently semicrystalline nature of polymers. At room temperature, disordered amorphous regions can occupy a significant fraction (30% or more in P3HT depending on molecular weight)[18-19] of the active layer. These disordered regions typically have significantly lower charge transport mobilities, resulting in charge transport occurring principally through the ordered regions. Therefore qualitatively, one would expect that effective charge transport between crystallites and percolation of crystalline regions (or aggregates) over macroscopic length scales is necessary for high mobility devices in conjugated polymers. The mesophase structure, a function of casting conditions, solvent, and regioregularity, has been experimentally correlated with the performance of field-effect transistors in many organic polymers, though many comparisons remain qualitative.[20-25]

Street *et al.* have treated the presence of the disordered region and charge transport theoretically.[26] The density of states within crystallites was assumed to be band-like with a 2D density of states, and amorphous regions were treated by introducing a “band-tail” of low mobility states within the gap. Agreement between the model and experimental data requires the consideration of multiple length scales: the electronic density of states within both the crystalline and disordered region, the transport between crystallites modeled by either conduction along bridging tie-chains or tunneling across low-angle grain boundaries, and the presence and nature of percolated pathways between electrodes. Though the authors treat the crystalline regions as exhibiting band-like transport and disordered regions having much lower mobilities, which may not be absolutely correct in the context of recent work on disordered polymers,[27-28] the work highlights that all of these length scales are necessarily coupled for understanding the charge transport in conjugated polymeric systems.

1.1.2 Light Absorption and Exciton Diffusion

Generation of free charge carriers in organic photovoltaics follows a fundamentally different pathway from that of inorganic counterparts.[29-30] Whereas for inorganics, free electron and holes are generated upon excitation, light absorption in organics results in the formation of a highly localized Coulombically-bound electron-hole pair, termed an exciton. Importantly, this excited state has a finite lifetime, and in order to generate free charge carriers the electron-hole pair must be dissociated at the interface of an electron donor and acceptor. Therefore, optimization of the photocurrent requires maximizing the overlap of the absorption of the chromophore with the solar spectrum while simultaneously providing donor-acceptor interfaces for the dissociation of excitons.

Absorption of a photon and generation of an exciton is the first step in the operation of OPVs and can be the limiting step in thin film devices (less than approximately 30 nm) for which the absorbance may be low. Unlike the transport of charge carriers in organic semiconductors, for which the hierarchical structure from molecular to device geometries is relevant, the structural features that determine the absorbed wavelengths and the oscillator strengths are at the lower end of the range. Much of the recent advance in controlling the optical band gap of conjugated polymers has been realized by design of the electronic structure of the chromophore. This has been most successfully implemented through the synthesis of donor-acceptor repeat units in which the electron density of the highest occupied molecular orbital (HOMO) is localized on the donor moiety and density of the lowest unoccupied molecular orbital (LUMO) is primarily located on the acceptor portion. It has been proposed that the band gap of polymers is reduced from a preference for the quinoidal character in these polymers.[31-32] Rational design of the donor and acceptor moieties in these systems have led to controlled band gaps and provide among the highest power conversion efficiencies when used as the donor material in OPVs.[33-35]

Although the design of the chromophore at the electronic level has contributed greatly to the synthesis of low band gap polymers, the structure at longer length scales affects the observed band gap as well. In polymers, covalent bonding along the backbone allows for delocalization over multiple repeat units. Though a gross oversimplification, the increase in conjugation along the backbone will be expected to decrease the band gap of the polymer from a simple particle in a box analogy for which spacing between energy levels decreases with increasing box size (the exact scaling with length is not expected to follow the $1/L^2$ predicted by a particle in a box but the inverse relationship should hold). Therefore, starting from a monomeric unit and increasing the degree of polymerization will exhibit a red-shifting of the absorption spectrum as the degree of delocalization increases.[36-38] However, upon further extension of the oligomer, statistical distributions of twists or kinks in the backbone cause the band gap to asymptote as the average molecular orbital overlap of adjacent units (which scales approximately with the cosine of the torsion angle between adjacent monomers[39]) decreases.[40-41] Upon crystallization or aggregation, polymer chains will increase planarity and conjugation length which will result in a red-shift in the absorption spectrum and the appearance of a vibronic progression.[42-43] It should be noted that the band gap will not be completely eliminated even in the absence of conformational defects for a 1-D polyacetylene chain because the alternation of single and double bonds (a theoretically predicted necessity) results in the opening of a band gap.[44]

Light absorption and exciton generation is dependent on the local structure of the excited and neighboring molecules, but the transfer of these excitons into a charge transfer state at a donor-acceptor interface is dependent on the structure at a larger length scale. Exciton migration to the donor-acceptor interface follows a hopping mechanism which is commonly modeled in the context of Förester resonant energy transfer (FRET).[45] This mechanism presented by Förester in 1948 is used to describe the non-radiative transfer of excitation between a donor and acceptor dipole.[46] It should be noted that in this context, the terms donor and acceptor are applied to different molecules of the same chemical identity (*i.e.* the diffusion process can occur through a single material). The energy transfer rate, k_{FRET}, is defined as a function of the distance between donor and acceptor as

$$k_{FRET} = \frac{1}{\tau_o}\left(\frac{r}{R_o}\right)^6 \tag{1.3}$$

where τ_o is the lifetime of the exciton and R_o is the Förester self-transfer radius (the latter of which depends on the orientation of the dipoles and the integrated spectral overlap of the absorption and emission of the acceptor and donor, respectively). Such a transfer rate has been directly related to the macroscopic exciton diffusion coefficient for many organic molecules.[47]

To gain a physical intuition of the characteristic length scale for the exciton migration process, the exciton diffusion length, L_D, can be defined as the square root of the product of the diffusion coefficient and the lifetime of the excited state. The exciton diffusion length in organic photovoltaics is an important parameter because exciton harvesting should benefit from active layers that possess structures commensurate with this value. Therefore many experimental approaches have been developed for the measurement of such a value.[48-52] One of the most commonly used of these techniques is thickness-dependent photoluminescent quenching in which thin layers of the material of interest are fabricated on an exciton quencher and the transient or steady-state luminescence is measured upon excitation with a probe.[53] At thicknesses below that of the exciton diffusion length, no measureable photoluminescence is observed as all excitons can migrate to the interface before radiative decay; increasing the thickness results in an increased photoluminescence signal as excitons begin to relax before quenching. However, although this technique provides a relatively simple platform for measurement, the formation of continuous layers for ultrathin films is difficult and optical interference effects can be introduced by the quenching which are not present in the control film.[47] From these measurements, typical values for the exciton diffusion length are on order of 10-100 nm though some reported values for small molecules approach a micron.[53-54] It is important to note that measurements on the diffusion length in conjugated polymers are on the 1-10 nm length scale,[55-60] an appropriate length scale to consider for structure engineering in polymer-based OPV active layers.

1.2 Opportunities and Challenges in Semiconducting Block Copolymers

From examination of the important processes involved in organic electronic devices, it is clear that the structure at the molecular through the micron length scale need to be controlled to optimize device performance. Although ideas are broadly applicable to many organic electronic devices, the operation of OPVs provides a particularly illustrative example for the importance of simultaneous control of structure at multiple length scales. At the ångström to nanometer length scale, the crystallinity needs to be optimized to ensure that the absorption profile of the active layer has sufficient overlap with the solar spectrum and that charge carrier mobilities are sufficiently high to collect charge carriers. Simultaneously, at the 10-100 nm length scale, interfaces between the electron donating and accepting materials need to be dispersed throughout the active layer to ensure that excitons generated at any point in the active layer reach a donor-acceptor interface. Additionally at the 100 nm to micron length scale, domains of the donor and acceptor throughout the active layer should be continuous to ensure optimal collection of free charge carriers and to prevent the buildup of charge carriers in isolated regions. Therefore, the structure over at least four orders of magnitude must be optimized though all are coupled in OPV active layers.

Fabricating active layers with alternating *p*- and *n*-type layers has frequently been presented as a broad concept to control the structure of OPVs[61-62] on all of these length scales though such an approach has been applied to light-emitting diodes[63-64] and field-effect transistors[65-66] as well. Nanostructuring has been accomplished with a variety of techniques including nanoimprinting,[67-73] anodized alumina templating,[74-77] layer-by-layer,[78] and blends of conjugated nanoparticles formed from microemulsions[79-81] among others. Though all of these approaches have experienced some level of success, many have difficulty reaching the 1-20 nm length scale (the measured exciton diffusion length of many polymers) or rely on techniques that are expensive to scale-up. Block copolymers, macromolecules that consist of two or more polymers covalently bonded together, can address these difficulties as they self-assemble into periodic nanostructures on the appropriate length scale and can be solution-processed.[82-83] In the simplest description, chemical dissimilarity results in an enthalpic driving force for demixing of the two polymers, though the covalent attachment precludes phase separation over length scales larger than the radius of gyration of the polymer resulting in the formation of microphase separated domains (typically 10-100 nm in dimension).[84] While the enthalpic driving force works to minimize the interfacial energy between the components, the entropic penalty for chain stretching prevents complete elongation of polymer chains. Periodic phases such as body-centered cubic spheres, hexagonally-packed cylinders, and alternating lamellae can be observed depending on the balance between these driving forces. The phase diagram for these systems can be parameterized by the strength of segregation, χN, (where χ is the Flory-Huggins interaction parameter and N is the overall degree of polymerization of the block copolymer) and the composition of the molecule, f.

Recently, copolymers comprised of a donor polymer (typically P3HT) covalently bound to a polymer with higher electron affinity have been synthesized for OPV applications.[85-87] Although the power conversion efficiency of this class of polymers has reached nearly 3.0%,[87] the control over the nanostructure is complicated from non-idealities introduced by the chain shape and crystallinity of conjugated systems. In the melt, semiconducting polymers typically adopt semiflexible or rod-like chain shapes which, when incorporated into block copolymers, create large conformational asymmetries between the conjugated moiety and the other component (which follows Gaussian chain statistics). As such, the accessible nanoscale ordered phases and their location in phase space are complicated by these packing constraints. Furthermore, upon crystallization of the conjugated polymer, periodic microphases can be significantly distorted or destroyed. Confinement of the crystallization, a concept that has yet to be extensively applied to conjugated block polymers, requires careful design of the block copolymer chemistry to prevent breakout. Though donor-acceptor diblock copolymers and different molecular architectures have been presented in the literature this thesis will focus on linear diblock copolymers in which only one of the components is optoelectronically-active.

1.2.1 Chain Shape in the Melt

Many commonly studied and industrially relevant polymers such as polyethylene (PE), polyisoprene (PI), and poly(ethylene oxide) (PEO) have flexible backbones because backbone rotation does not pose significant barriers to thermal fluctuations and multiple orientations are present at room temperature.[88] In contrast, electron delocalization along the backbone of conjugated polymers results in energetic states that favor orbital overlap and thus result in planar molecules. Furthermore, bulky alkyl side chains, frequently introduced to effect solubility in organic conjugated molecules, can result in steric interactions between monomers further favoring a rigid rod configuration.

The persistence length, l_p, (defined as the distance over which average bond orientations become uncorrelated) in conjugated polymers is frequently measured in solution using light or neutron scattering techniques. As alluded to earlier, the persistence length of conjugated polymers can vary widely depending on the sterics of the alkyl side chain and the geometry of the backbone conformations, and thus values can vary widely within the same class of molecules in addition to those with different conjugated backbones. In the case of the former, the persistence length of poly(phenylene vinylene) (PPV) polymers in solution have been measured with light scattering.[43,89] It was shown that while the persistence length of the commonly used poly(2-methoxy-5-(2-ethylhexyloxy)-1,4-phenylene vinylene) (MEH-PPV) was 6.0 nm, a substitution of the methoxy and ethylhexyloxy groups for the bulkier cholestanoxy groups resulted in an increase to 40 nm. It was also confirmed that the polymer-solvent interactions were at nearly the theta condition from measurement of the second virial coefficient, indicating that solvent interactions were not solely responsible for the changes. For comparison, the persistence lengths of poly(9,9-bis(2-ethyhexyl)fluorene-2,7-diyl) and poly(3-hexylthiophene) were determined by small angle neutron scattering to be at 7 and 3 nm, respectively, indicating that for similar contour lengths, conjugated polymers can span the range from completely rigid to semiflexible rods.[90-91] Importantly, though these values vary by nearly an order of magnitude between chemistries, all values are at an order of magnitude larger than that of flexible polymers such as PE (l_p=0.57 nm), PI (l_p=0.35 nm), and PEO (l_p=0.41 nm).[92]

At contour lengths below the persistence length, conjugated molecules behave as strict rigid rods. The anisotropic shape of the molecule or segments of the molecule as well as potential anisotropic electrostatic interactions can result in packing constraints in the melt or concentrated solution that favor orientational ordering. Though liquid crystallinity is not universally observed in conjugated polymers, many notable examples exist which have been proven to contribute to improve structural ordering. Grell *et al.* presented one of the earliest examples of a thermotropic conjugated main chain liquid crystalline polymer, poly(9,9-dioctylfluorene) (PFO).[93] A single heating and slow cooling cycle on a rubbed polyimide layer was sufficient to observe dichoric ratios of 6.6 for linearly polarized absorption. As a note, the authors only reported the molecular weight from GPC against polystyrene standards, which should not be expected to scale in the same manner as a semiflexible rod so it is difficult to know in what regime the chain shape was expected to be. From this seminal work, polyfluorenes have been explored for application as highly emissive (polarized) electroluminescent active layers.[94] Similarly, the high hole mobility of PBTTT has been attributed to its melt phase liquid crystallinity, the result of the rigid fused rings along the backbone.[24,95] Annealing in the liquid crystalline smectic phase can result in domains as large as 200 nm and reported mobilities approaching 1 cm^2 V^{-1} s^{-1}. Moreover, other backbone chemistries such as PPVs and polyacetylene have been shown to exhibit thermotropic liquid crystallinity as well.[96-98] Although the rigid nature of the backbone, and liquid crystallinity that may result from it, does not pose technological challenges in itself, new complexities to the phase diagram arise, as discussed below.

1.2.2 Conformational Asymmetry in Diblock Copolymers

Early theoretical studies on block copolymer self-assembly assumed that each block scaled as Gaussian coils with identical statistical segment lengths.[84] From this assumption, phase diagrams have been constructed against which experimental results have been compared. Though these original works have been quantitatively modified to include considerations such as fluctuation effects,[99] theoretically the qualitative behavior is not significantly altered. However, as discussed in the previous subsection, conjugation results in relatively long persistence lengths such that polymer chains either scale as semiflexible or completely rigid rods. Differences in entropic stretching, geometric packing, and anisotropic intermolecular interactions introduce complexities in the phase behavior when compared to classical block copolymers.

As the conformation of the two blocks varies the relative penalty for stretching the respective chains changes and consequently causes deviations from the expected theoretical phase diagram. Even relatively small differences in conformational asymmetry for Gaussian coils result in shifting of phase boundaries towards higher fractions of the higher statistical segment length component as observed in polyolefin block copolymers.[100] The change in the location of the order-order transitions results from an attempt by the system to relax the stretching of the system with smaller statistical segment length. Qualitative agreement with experimental results were obtained by Matsen and Bates using self-consistent field theory (SCFT).[101] The theoretical phase diagram obtained for conformationally asymmetric block copolymers possesses the same ordered phases as the symmetric case, though the phase boundaries of ordered phases shift towards the component with larger statistical segment length. These cases underscore the importance of conformational asymmetry, though differences in chain conformation are small (2.0 was the largest ratio of the statistical segment lengths investigated in the theoretical study).

In this limit of Gaussian coils with conformational asymmetry although the spinodal curve and morphological phase boundaries shift, the phases present and their relative location to one another is not greatly affected. However, at the other extreme as one (or both) of the blocks is assumed to approach the behavior of a rigid rod, changes to the spatial packing of the rod block and functional form of the conformational entropy introduce geometric considerations not present in systems with low conformational asymmetry. Furthermore, additional liquid crystalline attractions can significantly affect the phase behavior, biasing the formation of phases with flat interfaces such as smectics over those with large curvature. These block copolymers are termed rod-coil block copolymers. The liquid crystalline attractions and conformational asymmetry are two additional degrees of freedom in the phase behavior of these rod-coil systems. The former is parameterized by the Maier-Saupe interaction parameter, μ, and the latter, termed ν, is captured quantitatively as the ratio of the sizes of the two blocks ($bN^{1/2}$ and aN for the coil and rod), respectively.

This deviation from flexible coils to completely rigid rods was first treated analytically by Semenov and Vasilenko.[102] They found that upon increasing χ the nematic phase transitions first to a monolayer smectic A and finally a bilayer smectic A. The transition from monolayer to bilayer can be understood intuitively by considering that such a transition would decrease the block copolymer interfacial area at the expense of increased stretching of the coil block. It should be noted that the authors neglected all orientational disorder such that nematic and smectic A phases were necessarily observed over the isotropic and smectic C phases, respectively, though it could be expected that as the strength of segregation decreases, a tilt to rod blocks may be induced to limit the stretching of the coil block. The nematic phase is not usually observed in flexible systems, and though the density distribution in smectic A (or C) phase resemble lamellar morphologies in flexible systems, they are unique in the molecular orientation within the rod-like domain. Even in such early work, it becomes evident that the geometry of this class of rod-coil block copolymers introduces new phases and considerations for phase stability.

Holyst and Schick treated rod-coil diblocks with a Landau expansion of the free energy,[103] similar to the work of Leibler.[84] Unlike Leibler, the rod blocks are treated conformationally as rigid rods and the stability of phases was considered against both density and orientational fluctuations. From such a treatment, liquid crystalline (nematic) phases could be considered. However, because free energy expansions were only taken out to quadratic order, the symmetry of microphase separated phases could not be determined and all phases unstable to density fluctuations were labeled as "lamellar". In spite of this limitation, behavior unlike that of coil-coil block copolymers is observed. Most noticeably, transitions from isotropic to nematic phases are observed at high rod volume fractions, the phase boundary of which is controlled by the magnitude of liquid crystalline ordering parameter. Interestingly even in the case of non-aligning rods, the phase behavior deviates from that of classical coil-coil block copolymers due solely to the conformational asymmetry. In the absence of liquid crystalline ordering parameters, the microphase separated melt is observed to be stable as low as $\chi N = 9$, which is a result of the reduced entropy of the rigid portion of the polymer compared to flexible coils. Furthermore, the minimum of the spinodal curve occurs at volume fractions of the rod component of 0.45 rather than at the symmetric condition. Though the authors do not discuss the origin of such a shift, Fredrickson and coworkers attribute it to the propensity for the system to display spontaneous curvature.[104] In short, at the symmetric condition the system would rather place stiffer component on the inside of a curved interface due to the reduced stretching penalty for these chains and a smaller volume fraction of the rod block is necessary to offset such curvature. Reenders and ten Brinke, expanded the Landau expansion to fourth order and seven phases were considered.[105] In addition to the classical block copolymer phases introduced by Leibler (lamellar, hexagonal, and body-centered cubic),[84] the nematic, smectic A, and smectic C phases were considered. The authors observed that in the absence of liquid-crystalline interactions the phase diagram is asymmetric, but BCC and hexagonal phases can be observed to exist in the coil-rich portion of the phase diagram. Upon sufficiently increasing the Maier-Saupe interaction parameter, the transition from the isotropic to the nematic eventually emcompasses the whole spinodal curve and, upon increasing χ, transitions from the isotropic to ordered phases is preempted by a transition to the nematic phase followed by spatial ordering. In these cases, the hexagonal, BCC, and the (non-smectic) lamellar phases are precluded due to the liquid crystallinity and the smectic C phase is the only ordered phase observed. Therefore, though similarities can exist between the rod-coil and coil-coil systems, these similarities disappear as the preference for liquid crystalline ordering overwhelms the penalty to stretching the opposing polymer.

Experimental work has shown similar qualitative behavior to that expected by theory. While seminal work on rod-coil block copolymers consisting of poly(hexylisocyanate)-*b*-polystyrene system was presented by Chen *et al.*, many of the phases observed, such as arrowhead, wavy lamellae, and zig-zag, were not predicted by theory.[106] These phases have since been determined to not be thermodynamically stable phases, and highly dependent on the casting conditions chosen. To address this, a rod-coil system with reversible thermodynamic transitions was developed by Olsen *et al*. [107-109] In this polymer system, the rod portion consists of a conjugated poly(2,5-diethylhexyloxy-1,4-phenylenevinylene) (DEH-PPV) block which exhibits smectic and nematic phases coupled to a flexible polyisoprene block grown via anionic polymerization. Qualitative agreement with the phase diagram of Holyst and Schick was observed for the weakly-segregated PPV-PI polymer. Specifically, transitions from the isotropic phase to the smectic could be observed to either occur directly or through a nematic region depending on the composition of the polymer. However, even at high coil fractions, only lamellar phases were observed in the weakly-segregated limit. Increasing the molecular weight (and consequently the strength of segregation)[110] resulted in the observation of hexagonally packed domains with square cross-sections, in qualitative agreement with Reenders *et al.*[105] Quantification of the Flory-Huggins and Maier-Saupe interaction parameters as functions of temperature allowed for a mapping of the three-dimensional phase space for the PPV-PI block copolymer.[109]

Though the three-dimensional phase diagram for a rod-coil system presented a step forward in knowledge of rod-coil thermodynamics, the phase behavior of rod-coil polymers is known to have four degrees of freedom, two of which (the liquid crystalline ordering and repulsion of dissimilar monomeric units) were experimentally coupled through temperature. Therefore, the phase diagram developed by Olsen *et al*. is a three-dimensional cross-section through a four-dimensional phase space, the final dimension of which is the ratio of the temperature-dependent functional forms of the Flory-Huggins and Maier-Saupe interaction parameters. To access new regions of phase space, explicitly those in which the liquid crystalline interactions do not dominate the phase diagram, novel chemistries were developed with increased Flory-Huggins interaction parameter. Ho *et al.* synthesized poly(2,5-diethylhexyloxy-1,4-phenylenevinylene)-*b*-poly(methyl metacrylate) (PPV-PMMA) which in addition to phases observed in the PPV-PI system, exhibited lamellar phases without smectic ordering within the PPV domains.[111] Further decreases in the relative strength of the liquid crystalline ordering was observed in a poly(2,5-diethylhexyloxy-1,4-phenylenevinylene)-*b*-poly(4-vinylpyridine) (PPV-P4VP) system in which even spherical phases were observed.[112] These phases were predicted in the phase diagram of Reenders and ten Brinke at low ratios of μ/χ.

While the work on rod-coil block copolymers is important for understanding the phase behavior of this class of molecules, as discussed in the previous section, many polymers used in organic electronic devices can exhibit semiflexible behavior at high degrees of polymerization. To cover this region of phase space, Singh *et al.* applied a Landau free energy expansion (to quadratic order) to polymers with variable rigidity.[104] Importantly, at the extremes for the block rigidity, the phase behavior for rod-coil[103] and flexible coil-coil copolymers[84] were recovered. For diblocks with intermediate degrees of rigidity, though the phase diagrams were found to be qualitatively similar to the rod-coil case, the stability of the ordered phase showed non-monotonic changes as the stiffness was increased, illustrating the complexity of entropic contributions in these systems. The destabilization of the ordered phase upon initial stiffening of the flexible coil is consistent with spontaneous curvature effects, while the sharp decrease is due to the reduced conformational entropy cost with very stiff chains. Although the authors further examined systems such as semiflexible-rod and semiflexible-semiflexible diblocks, the effects of changing the rigidity were less pronounced than when observing systems with large asymmetry.

More recently, a self-consistent Brownian dynamics approach was applied to semiflexible-flexible diblocks by Kumar and Ganesan for which the microphase separated morphologies could be determined.[113] Using the variability in the flexibility as a parameter, the authors are (similar to the Landau expansion presented above) able to interpolate between the coil-coil and the rod-coil results. However, as an extension of the previous results, the authors show that only a small increase in the persistence length results in a dramatic change in the rod-rich portion of the phase diagram, though the coil-rich polymers are able to overcome the geometric constraints of the semiflexible block and remains relatively unchanged. It is proposed (though the authors do not modify the Maier-Saupe interaction) that the behavior can be overcome with a large increase in liquid crystallinity which would force orientational ordering of the semiflexible component and consequently induce rod-coil phase behavior. Importantly, this work along with the analytical work of Singh *et al.* illustrates that, like the rod-coil theory, for less severely rigid molecules (but of higher rigidity than the polyolefin cases presented above), the phase behavior will deviate significantly from the expectations for coil-coil polymers due to orientational ordering. Qualitatively, the results from our understanding of the competition between orientational ordering and phase demixing from rod-coil theory can be applied to that of semiflexible-flexible coil block copolymer self-assembly.

1.2.3 Crystallization in Semicrystalline-Amorphous Block Copolymers

In addition to additional complications presented by the chain shape in the melt, at room temperature high degrees of π-stacking in these planar molecules will frequently result in crystallization (or aggregation) in the solid state. Crystallization in semicrystalline block copolymers introduces another mechanism for microphase separation in the solid state with the morphology dictated by the structure of the crystalline component. However, the large enthalpic driving force for crystallization compared with that for microphase separation in the melt can dominate the structure formation, and the ultimate morphology is the result of the competition between these driving forces. Such considerations are of particular importance if the electronic application requires control of structure on the 10-100 nm length scale as the expected melt morphology can be superseded by the crystalline structure of the homopolymer. It should be noted that although crystalline-crystalline block copolymers provide further complex and rich phase behavior, the remainder of this thesis will be focused on crystalline-amorphous linear diblock copolymers.

In the simplest case of structure formation in semicrystalline block copolymers, crystallization proceeds from the homogeneous melt or solution. In such a case, phase separation and the nanoscale structure will be dictated entirely by the crystallization and the morphology, regardless of the thermodynamics, will be kinetically frozen. Ashman *et al*. synthesized poly(ethylene oxide)/poly(propylene oxide) (PEO/PPO) diblock and triblock copolymers of low molecular weight such that the melt phase structure was isotropic.[114-115] Upon crystallization, PEO chains crystallized to form a structure with alternating layers of crystalline PEO and a disordered blend of PEO and PPO. While diblock copolymers exclusively formed extended chain crystals, PPO-PEO-PPO triblocks resulted in both extended and once-folded crystallites, depending on the volume fraction of the PPO.

While the alternating lamellar morphology is expected and been treated theoretically,[116-117] structure formation is complicated when crystallization proceeds from inhomogeneous states. The competition between phase separation and crystallization is well-illustrated when crystallization occurs in solution-cast films. Depending on the selectivity of the solvent, the crystallization can proceed from either a molecularly mixed phase, resulting in similar (alternating lamellar) structures to the PEO-PPO system, or from a demixed, inhomogeneous phase. Hirata *et al.* cast poly(ethylene oxide)-*b*-polyisoprene (PEO-PI) from a non-selective solvent, benezene, and a solvent selective for polyisoprene, ethyl benzene.[118] The authors propose hypothetical ternary phase diagrams in which illustrate that the binodal curves for crystallization and the formation of micelles dictate the morphology formed; the use of different solvent selectivity simply shifted the binodal curves relative to one another in concentration space. Specifically, when cast from benzene, samples could be crystallized from micellar morphologies (depending on the critical micelle concentration), though casting from ethyl benzene forced PEO domains to crystallize from the homogeneous solution. Spherulites were observed in systems under optical microscopy showing that the crystallization event templates the structure at higher length scales. From these results, it is clear that the ultimate morphology is not solely the result of thermodynamic considerations as kinetically trapped structures can be observed depending on solvent choice.

Such kinetic trapping of (potentially) thermodynamically unstable phases is observed in block copolymers containing the conjugated polymer poly(3-hexylthiophene) (P3HT). McCullough and coworkers developed a convenient synthetic scheme for the synthesis of telechelic regioregular P3HT with a variety of functionalities, including ethynyl and allyl groups.[119] From this scheme many different flexible blocks have been polymerized from macroinitiators of P3HT including poly(methyl acrylate), poly(*t*-butyl methacrylate), poly(methyl methacrylate), polystyrene, polyisoprene, and polylactide.[85,120-124] In these P3HT systems, thin films solution cast exhibit nanofibrillar morphologies, the native crystalline state for P3HT homopolymer. Though it is tempting to suggest that the crystallization may represent block copolymer microphase separated states, the absence of curved morphologies even at high coil fractions (85 mol% PtBMA), a lack of higher order scattering peaks and scaling of the domain sizes which do not follow the equilibrium expected power laws for confined crystallization all suggest that the morphology is dominated by the crystallization of the P3HT.[122] As the melting transition temperature for P3HT is above room temperature (T_m ~ 230°C),[125] casting from solution results in a processing pathway analogous to that which resulted in the disordered morphology in the PI-PS system. Namely, the crystallization temperature is extremely high, suggesting that the binodal curve for such a system should precede that of solution phase separation for systems of modest strengths of segregation. From knowledge available from the PI-PS system, the use of a different system with a very high strength of segregation or a more selective solvent for P3HT (to lower the crystallization temperature of the thiophene block) may allow for inverting the binodal curves.

To this point in the section, discussion has focused on systems crystallized from the homogeneous melt or dilute solution which do not exhibit the same periodic assemblies accessible to the melt phase (*e.g.* BCC spheres, hexagonally-packed cylinders). As such, the phase behavior is dominated by the semicrystalline structure of the homopolymer and periodic structures on the 10-100 nm length scale other than alternating lamellar have not been discussed. Crystallization from the melt may be expected to result in periodic assemblies akin to those observed in the melt phase self-assembly discussed in the previous section, though the process can proceed through one of a number of pathways. If the microphase separated melt is not sufficiently strongly segregated, crystallization will result in the formation of an alternating lamellar structure regardless of the equilibrium melt phase structure. In fact, spherulitic structures reminiscent of homopolymer semicrystalline morphologies have been observed in these conditions, suggesting that the crystallization disrupts the block copolymer morphology at long length scales as well. Such behavior has been observed in poly(ε-caprolactone) (PCL),[126] poly(ethylene oxide),[127-128] and polyethylene systems[129-130] possessing rubbery amorphous components with low strengths of segregation at crystallization. While the disorder-order transition occurs without a measureable induction time, crystallization in these systems proceeds through a nucleation process with an experimentally observable induction time. This is evident in the poly(ε-caprolactone)-*b*-polybutadiene (PCL-PB) system studied by Nojima *et al.*[126] At sufficiently low χN, quenching from the disordered melt below the crystallization and spinodal temperatures resulted in first the demixing and nanoscale ordering of the dissimilar components followed by crystallization. The crystallization process resulted in a time period over which both ordered states (melt phase morphology and the crystalline lamellar) were present. Floudas *et al.* report similar results from PEO-PI crystallized from non-lamellar geometries, including a cubic (likely BCC) or hexagonal phases.[127] Unlike the PCL-PB system (for which the ODT is below T_m), these phases persist upon melting of the crystalline lamellar system, evidence of the competition between the two mechanisms for phase separation.

In contrast with these weakly-segregated rubbery systems in which the enthalpy of crystallization dominates the solid state structure formed, either a sufficiently high strength of segregation or the vitrification of the amorphous component can result in the preservation of the melt phase morphology. This confined crystallization results in a controllable structure (ångström to nanometer length scale) within a larger (10 – 100 nm length scale) superstructure, an important consideration for application to nanostructure organic electronics. Early work on confined crystallization was limited to glassy amorphous phases.[131-132] In these cases, the microphase separated melt is cooled below the glass transition of the amorphous component, which traps the melt phase morphology. Crystallization then proceeds from the melt phase of the crystallizable component, which does not (significantly) disrupt the ordering of the melt phase morphology. In this manner, the crystalline lamellar phase can be suppressed and the cylindrical or spherical phases can be observed below the crystallization temperature .[133-137]

The importance of vitrification in maintaining the microphase separated structure can be observed with varying casting temperature relative to the thermal transition temperatures of the component blocks. Cohen *et al.* showed that for a polystyrene-*b*-hydrogenated polybutadiene (PS-hPB) polymer although in the melt the polymer phase separates into close-packed spheres, casting at 65°C resulted in the formation of a semicrystalline phase (as evidenced by a melting endotherm in the DSC) though no microphase morphology was observed.[138] Annealing of the block copolymer above the glass transition of polystyrene and the melting transition of polyethylene recovered the spherical morphology. Alternatively, casting of the polymer solution above the melting point for polyethylene and the glass transition temperature of polystyrene resulted in phase separation upon solvent evaporation followed by crystallization confined to the spherical domains upon cooling below the crystallization temperature of polyethylene.

It was later shown that crystallization could be confined to states with rubbery as well as glassy amorphous domains provided that the strength of segregation at the crystallization temperature is sufficient. Synthesis of systems, polyethylene-b-poly(3-methyl-1-butene) and (PE-PMB) polyethylene-*b*-poly(styrene-*r*-ethylene-*r*-butene) (PE-SEB), that are strongly segregated at the crystallization temperature of polyethylene exhibit crystallization within cylindrical and spherical domains.[139-140] Importantly, it was later shown that the crystallization could effectively disrupt the spherical structure when the degree of polymerization was decreased at constant volume fraction.[141] Furthermore, at intermediate strength of segregation for cylinder-forming block copolymers, the crystallization is neither strictly confined as the kinetics of crystallization are identical to those in which the structure is deformed by the crystallization. For these samples, the SAXS patterns were not significantly distorted upon crystallization, but electron micrographs showed a fraction of crystallites bridging distinct hexagonally-packed domains. Therefore, two distinct regimes dependent on the strength of segregation of the rubbery block define the phase space with a transitional "templating" regime in between.

More recently, these design rules for confinement of semicrystalline block copolymers developed for polyethylene, poly(ethylene oxide), and poly(ε-caprolactone) have been applied to poly(3-alkylthiophene)-containing block copolymers. Using a P3AT, poly(3-(2-ethylhexyl)thiophene) (P3EHT), with melting point depressed by nearly 150°C from that of P3HT, Segalman and coworkers showed that the crystallization of the thiophene domains could be confined to lamellar and spherical domains.[142] Due to the depressed melting transition of the thiophene block, samples could be taken into the melt and allowed to self-assemble without concern of degradation. Importantly, this technique allowed for the self-assembly of a wide range of block copolymers as a wider window for thermal annealing allowed for chemistries with lower χ to be considered. Poly(3-dodecylthiophene)-*b*-poly(methyl methacrylate) have also been shown to self-assemble,[143] exhibiting self-assembled morphologies in the semicrystalline state that are in sharp contrast with those synthesized with P3HT.[122] The self-assembly of optoelectronically-active block copolymers remains an ongoing area of research.

1.3 Controlling the Structure of Conjugated Polymers at Multiple Length Scales

In this thesis, we show that many of these length scales can be tuned by simple chemical modifications to commonly-studied conjugated polymers. In particular, the structure of poly(3-alkylthiophenes) (P3ATs), among the most widely-studied conjugated polymers will be examined over a wide range of length scales with block copolymer self-assembly. However, the understanding of conjugated block copolymer self-assembly will be examined in the context of fundamental properties such as the melting temperature and strength of segregation, such that application to other systems should be possible. In Chapter 2, we will show that the thermal properties of poly(3-alkylthiophenes) can be predictively tuned with changes to the side chain chemistry and copolymerization with particular consideration given to P3EHT, a less commonly-studied P3AT. The control over the thermal properties is an important consideration to prevent breakout in semicrystalline-amorphous block copolymers (Section 1.2.3). In Chapter 3 we show that the crystallization of P3EHT at room temperature provides a convenient temperature and time range for correlating the crystalline structure with macroscopic device properties. These experiments capture the importance of large length scale structure for charge transport (Section 1.1.1). Chapter 4 demonstrates that a depressed melting transition of the semiconducting component is a sufficient condition to allow for confined crystallization of P3AT-containing block copolymers. The composition of the block copolymer dictates the morphologies that are observed, and at high contents of the P3AT, a semiconducting matrix can be formed in the solid state. In Chapter 5, the melt and crystalline structure is investigated further in a P3AT-containing block copolymer, providing an outlook on the relevant parameters for controlling the morphology in the solid-state. Chapter 6 provides an outlook on how the ideas from this thesis can act as design rules for the control over multiple length scales ranging from the crystalline through 100 nm.

1.4 References

1. Schein, L. B.; Duke, C. B.; McGhie, A. R. Observation of the Band-Hopping Transition for Electrons in Naphthalene. *Phys Rev Lett* **1978,** *40* (3), 197.

2. Jurchescu, O. D.; Baas, J.; Palstra, T. T. M. Effect of impurities on the mobility of single crystal pentacene. *Appl Phys Lett* **2004,** *84,* 3061.

3. Podzorov, V.; Menard, E.; Borissov, A.; Kiryukhin, V.; Rogers, J. A.; Gershenson, M. E. Intrinsic Charge Transport on the Surface of Organic Semiconductors. *Phys Rev Lett* **2004,** *93* (8), 086602.

4. Xie, H.; Alves, H.; Morpurgo, A. F. Quantitative analysis of density-dependent transport in tetramethyltetraselenafulvalene single-crystal transistors: Intrinsic properties and trapping. *Phys Rev B* **2009,** *80* (24), 245305.

5. Liu, C.; Minari, T.; Lu, X.; Kumatani, A.; Takimiya, K.; Tsukagoshi, K. Solution-Processable Organic Single Crystals with Bandlike Transport in Field-Effect Transistors. *Adv Mater* **2011,** *23* (4), 523.

6. Podzorov, V.; Menard, E.; Rogers, J. A.; Gershenson, M. E. Hall Effect in the Accumulation Layers on the Surface of Organic Semiconductors. *Phys Rev Lett* **2005,** *95,* 226601.

7. Takeya, J.; Tasukagoshi, K.; Aoyagi, Y.; Takenobu, T.; Iwasa, Y. Hall Effect of Quasi-Hole Gas in Organic Single-Crystal Transistors. *Jpn J Appl Phys* **2005,** *44,* L1393.

8. Ostroverkhova, O.; Cooke, D. G.; Shcherbyna, S.; Egerton, R. F.; Hegmann, F. A.; Tykwinski, R. R.; Anthony, J. E. Bandlike transport in pentacene and functionalized pentacene thin films revealed by subpicosecond transient photoconductivity measurements. *Phys Rev B* **2005,** *71,* 035204.

9. Duke, C. B.; Schein, L. B. Is energy-band theory enough. *Phys Today* **1980,** *33,* 42.

10. Marcus, R. A. On the Theory of OxidationReduction Reactions Involving Electron Transfer. I. *J Chem Phys* **1956,** *24* (5), 966.

11. Lan, Y. K.; Huang, C. I. A Theoretical Study of the Charge Transfer Behavior of the Highly Regioregular Poly-3-hexylthiophene in the Ordered State. *J Phys Chem B* **2008,** *112* (47), 14857.

12. Mas-Torrent, M.; Rovira, C. Role of Molecular Order and Solid-State Structure in Organic Field-Effect Transistors. *Chem Rev* **2011,** *111*, 4833.

13. Beljonne, D.; Cornil, J.; Coropceanu, V.; da Silva Filho, D. A.; Geskin, V.; Lazzaroni, R.; Leclere, P.; Bredas, J. L., On the Transport, Optical, and Self-Assembly Properties of p-Conjugated Materials: A Combined Theoretical/Experimental Insight. In *Conjugated Polymers: Theory, Synthesis, Properties, and Characterization*, 3rd ed.; Skotheim, T. A.; Reynolds, J. R., Eds. CRC Press: Boca Raton, 2007.

14. Coropceanu, V.; Cornil, J.; da Silva Filho, D. A.; Olivier, Y.; Silbey, R.; Bredas, J. L. Charge Transport in Organic Semiconductors. *Chem Rev* **2007,** *107* (4), 926.

15. Rivnay, J.; Noriega, R.; Kline, R. J.; Salleo, A.; Toney, M. F. Quantitative analysis of lattice disorder and crystallite size in organic semiconductor thin films. *Phys Rev B* **2011,** *84*, 045203.

16. Noriega, R.; Rivnay, J.; Vandewal, K.; Koch, F. P. V.; Stingelin, N.; Smith, P.; Toney, M. F.; Salleo, A. A general relationship between disorder, aggregation and charge transport in conjugated polymers. *Nat Mater* **2013,** *12*, 1038.

17. Rivnay, J.; Jimison, L. H.; Northrup, J. E.; Toney, M. F.; Noriega, R.; Lu, S.; Marks, T. J.; Facchetti, A.; Salleo, A. Large modulation of carrier transport by grain-boundary molecular packing and microstructure in organic thin films. *Nat Mater* **2009,** *8*, 952.

18. Balko, J.; Lohwasser, R. H.; Sommer, M.; Thelakkat, M.; Thurn-Albrecht, T. Determination of the Crystallinity of Semicrystalline Poly(3-hexylthiophene) by Means of Wide-Angle X-ray Scattering. *Macromolecules* **2013,** *46* (24), 9642.

19. Lee, C. S.; Dadmun, M. D. Important thermodynamic characteristics of poly(3-hexyl thiophene). *Polymer* **2014,** *55* (1), 4.

20. Kline, R. J.; McGehee, M. D. Morphology and Charge Transport in Conjugated Polymers. *J Macromol Sci Polym Rev* **2006,** *46*, 27.

21. Kline, R. J.; McGehee, M. D.; Kadnikova, E. N.; Liu, J.; Frechet, J. M. J.; Toney, M. F. Dependence of Regioregular Poly(3-hexylthiophene) Film Morphology and Field-Effect Mobility on Molecular Weight. *Macromolecules* **2005,** *38* (8), 3312.

22. Yang, H.; Shin, T. J.; Yang, L.; Cho, K.; Ryu, C. Y.; Bao, Z. Effect of Mesoscale Crystalline Structure on the Field-Effect Mobility of Regioregular Poly(3-hexylthiophene) in Thin Film Transistors. *Adv Funct Mater* **2005,** *15* (4), 671.

23. Chang, J. F.; Sun, B.; Breiby, D. W.; Nielsen, M. M.; Solling, T. I.; Giles, M.; McCulloch, I.; Sirringhaus, H. Enhanced Mobility of Poly(3-hexylthiophene) Transistors by Spin-Coating from High-Boiling-Point Solvents. *Chem Mater* **2004,** *16*, 4772.

24. McCulloch, I.; Heeney, M.; Bailey, C.; Genevicius, K.; MacDonald, I.; Shkunov, M.; Sparrowe, D.; Tierney, S.; Wagner, R.; Zhang, W.; Chabinyc, M. L.; Kline, R. J.; McGehee, M. D.; Toney, M. F. Liquid-crystalline semiconducting polymers with high charge-carrier mobility. *Nat Mater* **2006,** *5*, 328.

25. Trznadel, M.; Pron, A.; Zagorska, M.; Chrzaszcz, R.; Pielichowski, J. Effect of Molecular Weight on Spectroscopic and Spectroelectrochemical Properties of Regioregular Poly(3-hexylthiophene). *Macromolecules* **1998,** *31* (15), 5051.

26. Street, R. A.; Northrup, J. E.; Salleo, A. Transport in polycrystalline polymer thin-film transistors. *Phys Rev B* **2005,** *71*, 165202.

27. Zhang, M.; Tsao, H. N.; Pisula, W.; Yang, C.; Mishra, A. K.; Mullen, K. Field-Effect Transistors Based on a Benzothiadiazole−Cyclopentadithiophene Copolymer. *J Am Chem Soc* **2007,** *129* (12), 3472.

28. Liu, J.; Zhang, R.; Sauve, G.; Kowalewski, T.; McCullough, R. D. Highly Disordered Polymer Field Effect Transistors: N-Alkyl Dithieno[3,2-b:2′,3′-d]pyrrole-Based Copolymers with Surprisingly High Charge Carrier Mobilities. *J Am Chem Soc* **2008,** *130* (39), 13167.

29. Bredas, J. L.; Norton, J. E.; Cornil, J.; Coropceanu, V. Molecular Understanding of Organic Solar Cells: The Challenges. *Accounts Chem Res* **2009,** *42* (11), 1691.

30. Kippelen, B.; Bredas, J. L. Organic Photovoltaics. *Energy Environ Sci* **2008,** *2*, 251.

31. Ajayaghosh, A. Donor-acceptor type low band gap polymers: polysquaraines and related systems. *Chem Soc Rev* **2003,** *32*, 181.

32. Kroon, R.; Lenes, M.; Hummelen, J. C.; Blom, P. W. M.; de Boer, B. Small Bandgap Polymers for Organic Solar Cells. *Polym Rev* **2008,** *48*, 531.

33. Liang, Y.; Xu, Z.; Xia, J.; Tsai, S.-T.; Wu, Y.; Li, G.; Ray, C.; Yu, L. For the Bright Future—Bulk Heterojunction Polymer Solar Cells with Power Conversion Efficiency of 7.4%. *Adv Mater* **2010,** *22* (20), E135.

34. He, Z.; Zhong, C.; Huang, X.; Wong, W.-Y.; Wu, H.; Chen, L.; Su, S.; Cao, Y. Simultaneous Enhancement of Open-Circuit Voltage, Short-Circuit Current Density, and Fill Factor in Polymer Solar Cells. *Adv Mater* **2011,** *23* (40), 4636.

35. You, J.; Dou, L.; Yoshimura, K.; Kato, T.; Ohya, K.; Moriarty, T.; Emery, K.; Chen, C.-C.; Gao, J.; Li, G.; Yang, Y. A polymer tandem solar cell with 10.6% power conversion efficiency. *Nat Commun* **2013,** *4*, 1446.

36. Nayler, P.; Whiting, M. C. Researches on Polyenes. Part III. The Synthesis and Light Absorption of Dimethylpolyenes. *J Chem Soc* **1955**, 3037.

37. Ten Hoeve, W.; Wynberg, H.; Havinga, E. E.; Meijer, E. W. Substituted 2,2':5',2'':5'',2''':5''',2'''':5'''',2''''': 5''''',2'''''':5'''''',2''''''':5''''''',2'''''''':5'''''''',2'''''''''-undecithiophenes, the longest characterized oligothiophenes. *J Am Chem Soc* **1991,** *113* (15), 5887.

38. Thienpont, H.; Rikken, G. L. J. A.; Meijer, E. W.; ten Hoeve, W.; Wynberg, H. Saturation of the hyperpolarizability of oligothiophenes. *Phys Rev Lett* **1990,** *65* (17), 2141.

39. Brédas, J. L.; Street, G. B.; Thémans, B.; André, J. M. Organic polymers based on aromatic rings (polyparaphenylene, polypyrrole, polythiophene): Evolution of the electronic properties as a function of the torsion angle between adjacent rings. *J Chem Phys* **1985,** *83* (3), 1323.

40. Barbarella, G.; Zambianchi, M.; Bongini, A.; Antolini, L. The deformability of the thiophene ring: A key to the understanding of the conformational properties of oligo- and polythiophenes. *Adv Mater* **1993,** *5* (11), 834.

41. Distefano, G.; Dal Colle, M.; Jones, D.; Zambianchi, M.; Favaretto, L.; Modelli, A. Electronic and geometric structure of methylthiophenes and selected dimethyl-2,2'-bithiophenes. *J Phys Chem* **1993,** *97* (14), 3504.

42. McCullough, R. D.; Lowe, R. D.; Jayaraman, M.; Anderson, D. L. Design, synthesis, and control of conducting polymer architectures: structurally homogeneous poly(3-alkylthiophenes). *J Org Chem* **1993,** *58* (4), 904.

43. Gettinger, C. L.; Heeger, A. J.; Drake, J. M.; Pine, D. J. A photoluminescence study of poly(phenylene vinylene) derivatives: The effect of intrinsic persistence length. *J Chem Phys* **1994,** *101*, 1673.

44. Roncali, J. Synthetic Principles for Bandgap Control in Linear p-Conjugated Systems. *Chem Rev* **1997,** *97*, 173.

45. Feron, K.; Belcher, W. J.; Fell, C. J.; Dastoor, P. C. Organic Solar Cells: Understanding the Role of Forster Resonance Energy Transfer. *International Journal of Molecular Sciences* **2012,** *13*, 17019.

46. Förester, T. Zwischenmolekulare Energiewanderung und Fluoreszenz. *Ann Phys* **1948,** *437* (1-2), 55.

47. Lunt, R. R.; Giebink, N. C.; Belak, A. A.; Benziger, J. B.; Forrest, S. R. Exciton diffusion lengths of organic semiconductor thin films measured by spectrally resolved photoluminescence quenching. *J Appl Phys* **2009,** *105*, 053711.

48. Markov, D. E.; Blom, P. W. M. Anisotropy of exciton migration in poly(p-phenylene vinylene). *Phys Rev B* **2006,** *74* (8), 085206.

49. Gregg, B. A.; Sprague, J.; Peterson, M. W. Long-Range Singlet Energy Transfer in Perylene Bis(phenethylimide) Films. *J Phys Chem B* **1997,** *101* (27), 5362.

50. Kroeze, J. E.; Savenije, T. J.; Vermeulen, M. J. W.; Warman, J. M. Contactless Determination of the Photoconductivity Action Spectrum, Exciton Diffusion Length, and Charge Separation Efficiency in Polythiophene-Sensitized TiO2 Bilayers. *J Phys Chem B* **2003,** *107* (31), 7696.

51. Stevens, M. A.; Silva, C.; Russell, D. M.; Friend, R. H. Exciton dissociation mechanisms in the polymeric semiconductors poly(9,9-dioctylfluorene) and poly(9,9-dioctylfluorene-co-benzothiadiazole). *Phys Rev B* **2001,** *63* (16), 165213.

52. Pettersson, L. A. A.; Roman, L. S.; Inganäs, O. Modeling photocurrent action spectra of photovoltaic devices based on organic thin films. *J Appl Phys* **1999,** *86* (1), 487.

53. Peumans, P.; Yakimov, A.; Forrest, S. R. Small molecular weight organic thin-film photodetectors and solar cells. *J Appl Phys* **2003,** *93,* 3693.

54. Bulovic, V.; Forrest, S. R. Study of localized and extended excitons in 3,4,9,10-perylenetetracarboxylic dianhydride (PTCDA) II. Photocurrent response at low electric fields. *Chem Phys* **1996,** *210* (1-2), 13.

55. Halls, J. J. M.; Pichler, K.; Friend, R. H.; Moratti, S. C.; Holmes, A. B. Exciton Diffusion and Dissociation in a PPV/C-60 heterojunction Photovoltaic Cell. *Appl Phys Lett* **1996,** *68* (3120-3122).

56. Haugeneder, A.; Neges, M.; Kallinger, C.; Spirkl, W.; Lemmer, U.; Feldmann, J.; Scherf, U.; Harth, E.; Gugel, A.; Mullen, K. Exciton diffusion and dissociation in conjugated polymer fullerene blends and heterostructures. *Phys Rev B* **1999,** *59*, 15346.

57. Scully, S. R.; McGehee, M. D. Effects of optical interference and energy transfer on exciton diffusion length measurements in organic semiconductors. *J Appl Phys* **2006,** *100,* 034907.

58. Markov, D. E.; Tanase, C.; Blom, P. W. M.; Wildeman, J. Simultaneous enhancement of charge transport and exciton diffusion in poly(p-phenylene vinylene) derivatives. *Phys Rev B* **2005,** *72,* 045217.

59. Huijser, A.; Savenije, T. J.; Shalav, A.; Siebbeles, L. D. A. An experimental study on the molecular organization and exciton diffusion in a bilayer of a porphyrin and poly(3-hexylthiophene). *J Appl Phys* **2008,** *104,* 034505.

60. Shaw, P. E.; Ruseckas, A.; Samuel, I. D. W. Exciton Diffusion Measurements in Poly(3-hexylthiophene). *Adv Mater* **2008,** *20,* 3516.

61. Chen, J.-T.; Hsu, C.-S. Conjugated polymer nanostructures for organic solar cell applications. *Polym Chem* **2011,** *2* (12), 2707.

62. Segalman, R. A.; McCulloch, B.; Kirmayer, S.; Urban, J. J. Block Copolymers for Organic Optoelectronics. *Macromolecules* **2009,** *42* (23), 9205.

63. Tao, Y.; Ma, B.; Segalman, R. A. Self-Assembly of Rod−Coil Block Copolymers and Their Application in Electroluminescent Devices. *Macromolecules* **2008,** *41* (19), 7152.

64. Ma, B.; Lauterwasser, F.; Deng, L.; Zonte, C. S.; Kim, B. J.; Fréchet, J. M. J.; Borek, C.; Thompson, M. E. New Thermally Cross-Linkable Polymer and Its Application as a Hole-Transporting Layer for Solution Processed Multilayer Organic Light Emitting Diodes. *Chem Mater* **2007,** *19* (19), 4827.

65. Cavallini, M.; D'Angelo, P.; Criado, V. V.; Gentili, D.; Shehu, A.; Leonardi, F.; Milita, S.; Liscio, F.; Biscarini, F. Ambipolar Multi-Stripe Organic Field-Effect Transistors. *Adv Mater* **2011,** *23* (43), 5091.

66. Huettner, S.; Sommer, M.; Hodgkiss, J.; Kohn, P.; Thurn-Albrecht, T.; Friend, R. H.; Steiner, U.; Thelakkat, M. Tunable Charge Transport Using Supramolecular Self-Assembly of Nanostructured Crystalline Block Copolymers. *ACS Nano* **2011,** *5* (5), 3506.

67. Yang, Y.; Mielczarek, K.; Aryal, M.; Zakhidov, A.; Hu, W. Nanoimprinted Polymer Solar Cell. *ACS Nano* **2012,** *6* (4), 2877.

68. Kim, M.-S.; Kim, J.-S.; Cho, J. C.; Shtein, M.; Kim, J.; Guo, L. J.; Kim, J. Flexible conjugated polymer photovoltaic cells with controlled heterojunctions fabricated using nanoimprint lithography. *Appl Phys Lett* **2007,** *90* (12).

69. Wiedemann, W.; Sims, L.; Abdellah, A.; Exner, A.; Meier, R.; Musselman, K. P.; MacManus-Driscoll, J. L.; Müller-Buschbaum, P.; Scarpa, G.; Lugli, P.; Schmidt-Mende, L. Nanostructured interfaces in polymer solar cells. *Appl Phys Lett* **2010,** *96* (26).

70. Aryal, M.; Buyukserin, F.; Mielczarek, K.; Zhao, X.-M.; Gao, J.; Zakhidov, A.; Hu, W. Imprinted large-scale high density polymer nanopillars for organic solar cells. *J Vac Sci Technol B* **2008,** *26* (6), 2562.

71. Zhou, M.; Aryal, M.; Mielczarek, K.; Zakhidov, A.; Hu, W. Hole mobility enhancement by chain alignment in nanoimprinted poly(3-hexylthiophene) nanogratings for organic electronics. *J Vac Sci Technol B* **2010,** *28* (6), C6M63.

72. Cheyns, D.; Vasseur, K.; Rolin, C.; Genoe, J.; Poortmans, J.; Heremans, P. Nanoimprinted semiconducting polymer films with 50 nm features and their application to organic heterojunction solar cells. *Nanotechnology* **2008,** *19* (42), 424016.

73. Zeng, W.; Chong, K. S. L.; Low, H. Y.; Williams, E. L.; Tam, T. L.; Sellinger, A. The use of nanoimprint lithography to improve efficiencies of bilayer organic solar cells based on P3HT and a small molecule acceptor. *Thin Solid Films* **2009,** *517* (24), 6833.

74. Hsu-Shen, W.; Li-Hua, L.; Shih-Yung, C.; Yuh-Lin, W.; Kung-Hwa, W. Ordered polythiophene/fullerene composite core–shell nanorod arrays for solar cell applications. *Nanotechnology* **2009,** *20* (7), 075201.

75. Chen, D.; Zhao, W.; Russell, T. P. P3HT Nanopillars for Organic Photovoltaic Devices Nanoimprinted by AAO Templates. *ACS Nano* **2012,** *6* (2), 1479.

76. Huesmann, D.; DiCarmine, P. M.; Seferos, D. S. Template-synthesized nanostructure morphology influenced by building block structure. *J Mater Chem* **2011,** *21* (2), 408.

77. Cao, J.; Sun, J.; Shi, G.; Chen, H.; Zhang, Q.; Wang, D.; Wang, M. Photovoltaic properties of polythiophene nano-tubule films. *Mater Chem Phys* **2003,** *82* (1), 44.

78. Benten, H.; Ogawa, M.; Ohkita, H.; Ito, S. Design of Multilayered Nanostructures and Donor–Acceptor Interfaces in Solution-Processed Thin-Film Organic Solar Cells. *Adv Funct Mater* **2008,** *18* (10), 1563.

79. Kietzke, T.; Neher, D.; Landfester, K.; Montenegro, R.; Guntner, R.; Scherf, U. Novel approaches to polymer blends based on polymer nanoparticles. *Nat Mater* **2003,** *2* (6), 408.

80. Kietzke, T.; Neher, D.; Kumke, M.; Montenegro, R.; Landfester, K.; Scherf, U. A Nanoparticle Approach To Control the Phase Separation in Polyfluorene Photovoltaic Devices. *Macromolecules* **2004,** *37* (13), 4882.

81. Snaith, H. J.; Friend, R. H. Photovoltaic devices fabricated from an aqueous dispersion of polyfluorene nanoparticles using an electroplating method. *Synthetic Met* **2004,** *147* (1–3), 105.

82. Bates, F. S.; Fredrickson, G. H. Block copolymers - Designer soft materials. *Phys Today* **1999,** *52* (2), 32.

83. Bates, F. S.; Fredrickson, G. H. Block Copolymer Thermodynamics: Theory and Experiment. *Annu Rev Phys Chem* **1990,** *41*, 525.

84. Leibler, L. Theory of Microphase Separation in Block Co-Polymers. *Macromolecules* **1980,** *13* (6), 1602.

85. Tao, Y.; McCulloch, B.; Kim, S.; Segalman, R. A. The relationship between morphology and performance of donor-acceptor rod-coil block copolymer solar cells. *Soft Matter* **2009,** *5* (21), 4219.

86. Zhang, Q.; Cirpan, A.; Russell, T. P.; Emrick, T. Donor−Acceptor Poly(thiophene-block-perylene diimide) Copolymers: Synthesis and Solar Cell Fabrication. *Macromolecules* **2009,** *42* (4), 1079.

87. Guo, C.; Lin, Y.-H.; Witman, M. D.; Smith, K. A.; Wang, C.; Hexemer, A.; Strzalka, J.; Gomez, E. D.; Verduzco, R. Conjugated Block Copolymer Photovoltaics with near 3% Efficiency through Microphase Separation. *Nano Lett* **2013,** *13* (6), 2957.

88. Hiemenz, P. C.; Lodge, T. P., *Polymer Chemistry*, 2nd ed.; CRC Press: Boca Raton, 2007.

89. Gettinger, C. L.; Heeger, A. J.; Drake, J. M.; Pine, D. J. The Effect of Intrinsic Rigidity on the Optical Properties of PPV Derivatives. *Mol Cryst Liq Crys A* **1994,** *256* (1), 507.

90. Fytas, G.; Nothofer, H. G.; Scherf, U.; Vlassopoulos, D.; Meier, G. Structure and Dynamics of Nondilute Polyfluorene Solutions. *Macromolecules* **2002,** *35* (2), 481.

91. McCulloch, B.; Ho, V.; Hoarfrost, M. L.; Stanley, C.; Do, C.; Heller, W. T.; Segalman, R. A. Polymer Chain Shape of Poly(3-alkylthiophenes) in Solution Using Small-Angle Neutron Scattering. *Macromolecules* **2013,** *46* (5), 1899.

92. Fetters, L. J.; Lohse, D. J.; Richter, L. J.; Witten, T. A.; Zirkel, A. Connection between Polymer Molecular Weight, Density, Chain Dimensions, and Melt Viscoelastic Properties. *Macromolecules* **1994,** *27* (17), 4639.

93. Grell, M.; Bradley, D. D. C.; Inbasekaran, M.; Woo, E. P. A Glass-Forming Conjugated Main-Chain Liquid Crystal Polymer for Polarized Electroiuminescence Applications. *Adv Mater* **1997,** *9* (10), 798.

94. Neher, D. Polyfluorene Homopolymers: Conjugated Liquid-Crystalline Polymers for Bright Blue Emission and Polarized Electroluminescence. *Macromol Rapid Comm* **2001,** *22* (17), 1365.

95. Chabinyc, M. L.; Toney, M. F.; Kline, R. J.; McCulloch, I.; Heeney, M. X-ray Scattering Study of Thin Films of Poly(2,5-bis(3-alkylthiophen-2-yl)thieno[3,2-b]thiophene). *J Am Chem Soc* **2007,** *129,* 3326.

96. Yang, S. H.; Hsu, C. S. Liquid Crystalline Conjugated Polymers and Their Applications in Organic Electronics. *J Polym Sci, Part A: Polym Chem* **2009,** *47,* 2713.

97. Olsen, B. D.; Jang, S. Y.; Luning, J. M.; Segalman, R. A. Higher order liquid crystalline structure in low-polydispersity DEH-PPV. *Macromolecules* **2006,** *39* (13), 4469.

98. Lam, J. W. Y.; Tang, B. Z. Liquid-crystalline and light-emitting polyacetylenes. *J Polym Sci, Part A: Polym Chem* **2003,** *41* (17), 2607.

99. Fredrickson, G. H.; Helfand, E. Fluctuation Effects in the Theory of Microphase Separation in Block Copolymers. *J Chem Phys* **1987,** *87*, 697.

100. Almdal, K.; Koppi, K. A.; Bates, F. S.; Mortensen, K. Multiple ordered phases in a block copolymer melt. *Macromolecules* **1992,** *25* (6), 1743.

101. Matsen, M. W.; Bates, F. S. Conformationally Asymmetric Block Copolymers. *J Polym Sci, Part B: Polym Phys* **1996,** *35* (6), 945.

102. Semenov, A. N.; Vasilenko, S. V. Theory of the nematic-semectic-A transition in a melt of macromolecules consisting of a rigid and a flexible block. *J Exp Theor Phys* **1986,** *63* (1), 70.

103. Holyst, R.; Schick, M. Correlations in a rigid-flexible diblock copolymer system. *J Chem Phys* **1991,** *96* (1), 730.

104. Singh, C.; Goulian, M.; Liu, A. J.; Fredrickson, G. H. Phase Behavior of Semiflexible Diblock Copolymers. *Macromolecules* **1994,** *27*, 2974.

105. Reenders, M.; ten Brinke, G. Composition and Orientational Ordering in Rod-Coil Diblock Copolymer Melts. *Macromolecules* **2002,** *35*, 3266.

106. Chen, J. T.; Thomas, E. L.; Ober, C. K.; Mao, G. Self-Assembled Smectic Phases in Rod-Coil Block Copolymers. *Science* **1996,** *273*, 343.

107. Olsen, B. D.; Segalman, R. A. Structure and thermodynamics of weakly segregated rod-coil block copolymers. *Macromolecules* **2005,** *38* (24), 10127.

108. Olsen, B. D.; Li, X. F.; Wang, J.; Segalman, R. A. Thin film structure of symmetric rod-coil block copolymers. *Macromolecules* **2007,** *40* (9), 3287.

109. Olsen, B. D.; Shah, M.; Ganesan, V.; Segalman, R. A. Universalization of the phase diagram for a model rod-coil diblock copolymer. *Macromolecules* **2008,** *41* (18), 6809.

110. Olsen, B. D.; Segalman, R. A. Nonlamellar phases in asymmetric rod-coil block copolymers at increased segregation strengths. *Macromolecules* **2007,** *40* (19), 6922.

111. Ho, C. C.; Lee, Y. H.; Dai, C. A.; Segalman, R. A.; Su, W. F. Synthesis and Self-assembly of Poly(diethylhexyloxy-p-phenylenevinylene)-b-poly(methyl methacrylate) Rod-Coil Block Copolymers. *Macromolecules* **2009,** *42* (12), 4208.

112. Sary, N.; Rubatat, L.; Brochon, C.; Hadziioannou, G.; Ruokolainen, J.; Mezzenga, R. Self-Assembly of Poly(diethylhexyloxy-p-phenylenevinylene)-bpoly(4-vinylpyridine) Rod-Coil Block Copolymer Systems. *Macromolecules* **2007,** *40*, 6990.

113. Kumar, N. A.; Ganesan, V. Communication: Self-assembly of semiflexible-flexible block copolymers. *J Chem Phys* **2012,** *136* (10).

114. Ashman, P. C.; Booth, C. Crystallinity and fusion of ethlene oxide/propylene oxide block copolymers: 1. Type PE copolymers. *Polymer* **1975,** *16*, 889.

115. Ashman, P. C.; Booth, C.; Cooper, D. R.; Price, C. Crystallinity and fusion of ethylene oxide/propylene oxide block copolymers: 2. Type PEP copolymers. *Polymer* **1975,** *16* (12), 897.

116. DiMarzio, E. A.; Guttman, C. M.; Hoffman, J. D. Calculation of Lamellar Thickness in a Diblock Copolymer, One of Whose Components Is Crystalline. *Macromolecules* **1980,** *13* (5), 1194.

117. Whitmore, M. D.; Noolandi, J. Theory of Crystallizable Block Copolymer Blends. *Macromolecules* **1988,** *21* (5), 1482.

118. Hirata, E.; Ijitsu, T.; Soen, T.; Hashimoto, T.; Kawai, H. Domain structure and crystalline morphology of AB and ABA type block copolymers of ethylene oxide and isoprene cast from solution. *Polymer* **1974,** *16*, 249.

119. Jeffries-El, M.; Sauv, G.; McCullough, R. D. Facile Synthesis of End-Functionalized Regioregular Poly(3-alkylthiophene)s via Modified Grignard Metathesis Reaction. *Macromolecules* **2005,** *38* (25), 10346.

120. Liu, J.; Sheina, E. E.; Kowalewski, T.; McCullough, R. D. Tuning the Electrical Conductivity and Self-Assembly of Regioregular Polythiophene by BlockCopolymerization : Nanowire Morphologies in New Di- and Triblock Copolymers. *Angew Chem Int Edit* **2002,** *41* (2), 329.

121. Iovu, M. C.; Jeffries-El, M.; Sheina, E. E.; Cooper, J. R.; McCullough, R. D. Regioregular poly(3-alkylthiophene) conducting block copolymers. *Polymer* **2005,** *46*, 8582.

122. Iovu, M. C.; Zhang, R.; Cooper, J. R.; Smilgies, D. M.; Javier, A. E.; Sheina, E. E.; Kowalewski, T.; McCullough, R. D. Conducting Block Copolymers of Regioregular Poly(3-hexylthiophene) and Poly(methacrylates): Electronic Materials with Variable Conductivities and Degrees of Interfibrillar Order. *Macromol Rapid Comm* **2007,** *28* (1816-1824).

123. Iovu, M. C.; Craley, C. R.; Jeffries-El, M.; Krankowski, A. B.; Zhang, R.; Kowalewski, T.; McCullough, R. D. Conducting Regioregular Polythiophene Block Copolymer Nanofibrils Synthesized by Reversible Addition Fragmentation Chain Transfer Polymerization (RAFT) and Nitroxide Mediated Polymerization (NMP). *Macromolecules* **2007,** *40* (14), 4733.

124. Boudouris, B. W.; Frisbie, C. D.; Hillmyer, M. A. Nanoporous Poly(3-alkylthiophene) Thin Films Generated from Block Copolymer Templates. *Macromolecules* **2008,** *41* (1), 67.

125. Ho, V.; Boudouris, B. W.; Segalman, R. A. Tuning Polythiophene Crystallization through Systematic Side Chain Functionalization. *Macromolecules* **2010,** *43* (19), 7895.

126. Nojima, S.; Kata, K.; Yamamoto, S.; Ashida, T. Crystallization of Block Copolymers. 1. Small-Angle X-ray Scattering Study of an eCaprolactone-Butadiene Diblock Copolymer. *Macromolecules* **1992,** *25* (8), 2237.

127. Floudas, G.; Ulrich, R.; Wiesner, U. Microphase separation in poly(isoprene-b-ethylene oxide) diblock copolymer melts. I. Phase state and kinetics of the order-to-order transitions. *J Chem Phys* **1999,** *110* (1), 652.

128. Floudas, G.; Vazaiou, B.; Schipper, F.; Ulrich, R.; Wiesner, U.; Iatrou, H.; Hadjichristidis, N. Poly(ethylene oxide-b-iosprene) Diblock Copolymer Phase Diagram. *Macromolecules* **2001,** *34* (9), 2947.

129. Rangarajan, P.; Register, R. A.; Fetters, L. J.; Bras, W.; Naylor, S.; Ryan, A. J. Crystallization of a Weakly Segregated Polyolefin Diblock Copolymer. *Macromolecules* **1995,** *28* (14), 4932.

130. Ryan, A. J.; Hamley, I. W.; Bras, W.; Bates, F. S. Structure Development in Semicrystalline Diblock Copolymers Cystallizing from the Ordered Melt. *Macromolecules* **1995,** *28*, 3860.

131. Douzinas, K. C.; Cohen, R. E. Chain Folding in EBEE Semicrystalline Diblock Copolymers. *Macromolecules* **1992,** *25*, 5030.

132. Hamley, I. W.; Fairclough, J. P. A.; Terrill, N. J.; Ryan, A. J.; Lipic, P. M.; Bates, F. S.; Towns-Andrews, E. Crystallization in Oriented Semicrystalline Diblock Copolymers. *Macromolecules* **1996,** *29*, 8835.

133. Loo, Y. L.; Register, R. A.; Ryan, A. J.; Dee, G. T. Polymer Crystallization Confined in One, Two, or Three Dimensions. *Macromolecules* **2001,** *34* (26), 8968.

134. Quiram, D. J.; Register, R. A.; Marchand, G. R.; Adamson, D. H. Chain Orientation in Block Copolymer Exhibiting Cylindrically Confined Crystallization. *Macromolecules* **1998,** *31* (15), 4891.

135. Chung, T. M.; Wang, T. C.; Ho, R. M.; Sun, Y. S.; Ko, B. T. Polymer Crystallization under Nanoscale 2D Spatial Confinement. *Macromolecules* **2010,** *43* (14), 6237.

136. Nojima, S.; Ohguma, Y.; Kadena, K.; Ishizone, T.; Iwasaki, Y.; Yamaguchi, K. Crystal Orientation of Poly(ε-caprolactone) Homopolymers Confined in Cylindrical Nanodomains. *Macromolecules* **2010,** *43* (8), 3916.

137. Loo, Y. L.; Register, R. A.; Adamson, D. H. Direct Imaging of Polyethylene Crystallites within Block Copolymer Microdomains. *J Polym Sci Pol Phys* **2000,** *38*, 2564.

138. Cohen, R. E.; Cheng, P. L.; Douzinas, K. C.; Kofinas, P.; Berney, C. V. Path-dependent Morphologies of a Diblock Copolymer of Polystyrene/Hydrogenated Polybutadiene. *Macromolecules* **1990,** *23* (1), 324.

139. Quiram, D. J.; Register, R. A.; Marchand, G. R. Crystallization of Asymmetric Diblock Copolymers from Microphase-Separated Melts. *Macromolecules* **1997,** *30* (16), 4551.

140. Loo, Y.-L.; Register, R. A.; Ryan, A. J. Polymer Crystallization in 25-nm Spheres. *Phys Rev Lett* **2000,** *84* (18), 4120.

141. Loo, Y. L.; Register, R. A.; Ryan, A. J. Modes of Crystallization in Block Copolymer Microdomains: Breakout, Template, and Confined. *Macromolecules* **2002,** *35* (6), 2365.

142. Ho, V.; Boudouris, B. W.; McCulloch, B. L.; Shuttle, C. G.; Burkhardt, M.; Chabinyc, M. L.; Segalman, R. A. Poly(3-alkylthiophene) Diblock Copolymers with Ordered Microstructures and Continuous Semiconducting Pathways. *J Am Chem Soc* **2011,** *133* (24), 9270.

143. Moon, H. C.; Bae, D.; Kim, J. K. Self-assembly of Poly(3-dodecylthiophene)-block-poly(methyl methacrylate) Copolymers Driven by Competition between Microphase Separation and Crystallization. *Macromolecules* **2012,** *45* (12), 5201.

Chapter 2: Controlling Thermal and Optoelectronic Properties of Poly(3-alkylthiophenes) with Side Chain Substitution and Copolymerization

Adapted from "Tuning Polythiophene Crystallization through Systematic Side Chain Functionalization," V. Ho, B.W. Boudouris, R.A. Segalman, *Macromolecules,* 2010, 43 (19), 7895-7899 (DOI: 10.1021/ma101697m) and "Control of thermal and optoelectronic properties in conjugated poly(3-alkylthiophenes)" V. Ho, B.S. Beckingham, H.H. Ng, R.A. Segalman, *MRS Communications,* in press (DOI: 10.1557/mrc.2014.9) with permission of the authors. *Reproduced by permission of The American Chemical Society and Materials Research Society*

Control over the solid state self-assembly of block copolymers containing poly(3-alkylthiophenes) (P3ATs) requires controlling the crystallization temperature of the thiophene moiety, as discussed in Section 1.2. In this chapter, we show that side chain functionalization of polythiophene can be used to tune thermal transitions over a range of 150 °C which creates a window where the structure may be controlled through thermal or solvent processing. First we report the molecular, structural, and optoelectronic properties of poly(3-(2-ethylhexyl)thiophene) (P3EHT), which indicate that it is semicrystalline and has comparable device behavior to two more common poly(3-alkylthiophenes) (P3ATs), poly(3-hexylthiophene) (P3HT) and poly(3-dodecylthiophene) (P3DDT). P3EHT absorbance spectra are similar to straight chain P3ATs and field-effect mobilities are measured to be on the same order of magnitude as P3DDT when the polymer is allowed to crystallize at room temperature. Importantly these similarities, in combination with the lower melting transition relative to P3HT, show that P3EHT may serve as a desirable candidate for synthesis of block copolymers that will self-assemble into periodic structures in the solid state.

Furthermore, we show that the 3EHT and 3HT monomers can be copolymerized and that the repeat units co-crystallize into a single unit cell. Depending on the composition of the copolymer, the thermal transitions can be smoothly varied between that of the two homopolymers. However, the crystal structure of copolymers of 3-alkylthiophenes is dictated by the composition of the copolymer. This dependence results in the adoption of a unit cell nearly identical to that of one the two homopolymers, which subsequently affects the optical properties. Notably, the composition of copolymers is a convenient handle to predictably control the thermal properties, crystalline morphology, and optical properties simultaneously.

2.1 Introduction

Poly(3-alkylthiophenes) (P3ATs) have been used broadly in organic electronic applications because they transport holes well (μ_h ~10^{-2} cm^2 $V^{-1}s^{-1}$), are processable into thin films from many common organic solvents, and they have relatively low band gaps (E_g ~1.9 eV) that can be tuned through chemical modification.[1-4] Originally introduced to increase solubility in polythiophenes, side chain alkyl substitutions allowed for synthesis of higher molecular weight polymers.[5-6] Since these initial efforts, side chain substitution has been used to tune the electronic properties of polythiophene,[7-9] improve polythiophene solubility in polar solvents,[10-11] and promote polymer interaction with inorganic species.[12] Some of these early results showed that the crystalline melting temperature is suppressed with the use of longer alkyl side chains;[13-14] however, little work has been performed to passivate rod-rod intermolecular interactions for control of nanoscale morphology. Poly(3-hexylthiophene) (P3HT) has become one of the most utilized active layer materials both in high performance organic field-effect transistors (OFETs)[15-16] and organic photovoltaic (OPV) devices.[17-19] However, it generally has not been possible to control the nucleation and growth of crystalline grains as the melting temperature of P3HT is extremely close to its degradation temperature.[20] To date, obtaining well-ordered morphologies over long ranges in P3HT thin films has proven difficult due to the rapid formation of thin lamellae (nanofibrils) when cast from solution[21-23] or cooling from the melt.[24] These strong rod-rod interactions also severely complicate phase behavior in multicomponent P3HT-containing systems, such as polymer-fullerene blends for OPV active layers.[25-28] Additionally, strong rod-rod interactions dominate the microphase separation in P3HT-containing block copolymers and prevent the formation of well-ordered domains commonly observed in all-coil block copolymers.[29-30] In fact, if passivation of rod self-alignment occurred, many previously unexplored microstructures could be found.

In addition to morphological control afforded by manipulation of the thermal transition, control of the optoelectronic properties is important for potential application to devices. The copolymerization of P3AT monomers has been presented as a convenient synthetic approach for controlling the thermal and optoelectronic properties simultaneously. In copolymers of poly(3-butylthiophene) and poly(3-octylthiophene), Jenekhe and coworkers have shown that both the melting transitions and (*h*00) lattice spacings are linear functions of composition and span the range between the two endpoints.[31] However, though the lattice spacings shift, the UV-vis absorbance edge aligns with that of both endpoints and no shift in the onset of absorption is observed (though a red-shift in the absorbance peak max is observed). More recently, copolymers of 3-(2-ethylhexyl)thiophene and 3-hexylthiophene have been synthesized by several groups. Zhang *et al.* showed that copolymers of P3EHT and P3HT resulted in melting transitions which were significantly depressed from that of P3HT and could be controlled through the relative composition.[32] Thompson and coworkers extended this work and observed that the open-circuit voltage of bulk heterojunctions with P3AT copolymers and PCBM spanned the range of the two components, though the complicated relationship between bulk heterojunction solar cell morphology and performance precludes definitive fundamental explanation for the observed optimal composition.[33]

In this chapter, we examine how chemistry affects the thermal, structural, and electronic properties in conjugated P3ATs. We first detail the properties of a less-studied P3AT, poly(3-(2-ethylhexyl)thiophene) (P3EHT) and compare its properties to two more common P3ATs, poly(3-hexylthiophene) and poly(3-dodecylthiophene) (P3DDT). The bulk and thin film microstructure of the polymers were studied using x-ray diffraction (XRD) and atomic force microscopy (AFM), respectively. Additionally, the optoelectronic properties of these materials are studied using thin film ultraviolet-visible (UV-Vis) absorption spectroscopy and field-effect transistor (FET) testbeds. These results demonstrate that P3EHT has comparable optical and charge transport properties to that of P3HT and P3DDT. Next, we show that the thermal and optical properties can be controlled predictably with the copolymerization of 3EHT and 3HT repeat units. Specifically, we show that the melting transitions of copolymers are dependent on the overall chemical composition. Importantly, though Hashimoto and coworkers[34] suggest that increasing the 3EHT content introduces crystalline defects that decrease the melting transition, we show in this work that both monomers must necessarily co-crystallize in order to observe universally accepted signatures of crystallinity in UV-vis, XRD, and DSC over the entire molar composition range. This inclusion of both repeat units within a single unit cell causes the lattice of P3EHT-*co*-P3HT to abruptly shift between that of P3HT and P3EHT homopolymers as the

3EHT content is increased, and we show that differences in the crystal structure can be correlated with the energy of the 0-0 transition (defined as the energy of the transition from the vibration-less ground state to the vibration-less first excited state) in UV-vis absorbance. This work presents a coherent illustration that more than just acting as a solubilizing unit the side chains play an important role on the melting transition temperature, the crystal structure, and the optical properties.

2.2 Experimental

2.2.1 General Methods

The ^{1}H NMR spectra were measured on either a Bruker AVQ-400 or AV-500 spectrometer using deuterated chloroform (Cambridge) solutions containing ~1 wt % polymer. Molecular weights and polydispersities were determined by gel permeation chromatography (GPC) data collected on either a Viscotek TDA 302 SEC with a set of three Styrogel HR columns (two HR3 and one HR4 columns) or four Viscotek T-columns (one of each of T6000, T5000, T4000, and T3000 columns) and a refractive index detector. THF at 35 °C was used as the mobile phase at a flow rate of 1 mL min^{-1} and the GPC was calibrated with polystyrene (PS) standards (Polymer Laboratories). Film thicknesses were estimated by scratching the polymer film and measuring the step change with a Veeco Dektak 150 profilometer.

2.2.2 Detailed Synthetic Procedure

Materials. All reagents and solvents were used as received from Sigma-Aldrich unless otherwise noted. Degassed tetrahydrofuran (THF) was purified by passage through an activated alumina column (Advanced Specialty Gas Equipment, 7x12 mesh) and was collected in flame-dried, air-free flask. Poly(3-alkylthiophenes) (P3ATs) were synthesized according to the GRIM procedure established in the literature.[35]

Synthesis of 3-(2-ethylhexyl)thiophene. A 500 mL 3-neck flask was flame-dried and back-filled with nitrogen. Magnesium (10.17 g, 0.42 mol) was added to flask, followed by addition of anhydrous THF and 2-ethylhexyl bromide (78.87 g, 0.41 mol) by cannula. After addition, solution was refluxed until all of the magnesium reacted. A suspension of 1,3-bis(diphenylphosphino)propane nickel(II) chloride (Ni(dppp)Cl_2, 1.62 g, 3.0 mmol) in 3-bromothiophene (50 g, 0.31 mol) was added dropwise by cannula to the solution at 0 °C. The reaction was allowed to proceed under nitrogen overnight at room temperature. Reaction quenched with 1 M acid, extracted with ether, and washed with water. Product was concentrated by rotary evaporation and purified by column chromatography (eluent hexanes). ^{1}H NMR (400 MHz, $CDCl_3$): δ_H 0.87 (t, 6H), 1.27 (m, 8H), 1.54 (t, 1H), 2.56 (d, 2H), 6.90 (m, 2H), 7.23 (m, 1H).

Synthesis of 2,5-dibromo-3-(2-ethylhexyl)thiophene. *N*-bromosuccinimide (29.5 g, 0.166 mol) was added to 3-alkylthiophene (14.8 g, 0.075 mol) in THF. The reaction was allowed to proceed under nitrogen for four hours at room temperature, quenched with water, and extracted with ether. The organic phase was washed with 10 wt% aqueous sodium thiosulfate, 10 wt% aqueous potassium hydroxide, and water. Product concentrated by rotary evaporation and purified by column chromatography (eluent hexanes). ^1H NMR (400 MHz, $CDCl_3$): δ_H 0.88 (t, 6H), 1.27 (m, 8H), 1.55 (t, 1H), 2.44 (d, 2H), 6.75 (s, 2H).

Representative Synthesis of Poly(3-(2-ethylhexyl)thiophene) (P3EHT-54). General procedure for synthesis of P3AT follows GRIM method presented by McCullough and coworkers. A 250 mL three neck flask was flame-dried and back-filled with nitrogen. 2,5-dibromo-3-(2-ethylhexyl)thinophene (5.05 g, 14.3 mmol) was added by syringe followed by addition of anhydrous THF. A solution of 2.0 M *tert*-butylmangesium chloride (7.00 mL, 14 mmol) in diethyl ether was added by syringe and the reaction solution was refluxed for 90 minutes. After cooling to room temperature, dry $Ni(dppp)Cl_2$ (47.4 mg, 0.088 mmol) was added and the solution was allowed to react for 45 minutes. Solution turned red upon addition of nickel catalyst and retained color for the duration of the reaction. The polymer was then precipitated in methanol and collected by vacuum filtration. The powder was then extracted with methanol, acetone, and chloroform with a Soxhlet apparatus. The final product was collected as a dark red powder from the chloroform phase by precipitation in methanol and was dried under vacuum overnight.

Representative Synthesis of Poly(3-(2-ethylhexyl)thiophene)-Poly(3-hexylthiophene) Random Copolymers. General procedure for synthesis of P3AT random copolymers follows GRIM method presented by McCullough and coworkers and adapted by others for random copolymerization. A 250 mL three neck flask was flame-dried and back-filled with nitrogen. 2,5-dibromo-3-(2-ethylhexyl)thiophene (2.48 g, 7.00 mmol) and 2,5-dibromo-3-hexylthiophene (2.60 g, 7.00 mmol) were added by syringe followed by addition of anhydrous THF. A solution of 2.0 M *tert*-butylmangesium chloride (7.00 mL, 14.0 mmol) in diethyl ether was added by syringe and the reaction solution was refluxed for 90 minutes. After cooling to room temperature, dry $Ni(dppp)Cl_2$ (119 mg, 0.22 mmol) was added and the solution was allowed to react for 45 minutes. Solution turned red upon addition of nickel catalyst and retained color for the duration of the reaction. The polymer was then precipitated in methanol and collected by vacuum filtration. The powder was then extracted with methanol, acetone, and chloroform with a Soxhlet apparatus. Hexanes was used for washing of P3EHT:P3HT-65 and P3HT. The final product was collected as a colored powder from the chloroform phase by precipitation in methanol and was dried under vacuum overnight.

2.2.3 Thermal and Structural Characterization

Differential scanning calorimetry (DSC) measurements were acquired using a Thermal Advantage Q20 calorimeter. An indium standard was used to calibrate the instrument and nitrogen was used as the purge gas. X-ray diffraction (XRD) data of the P3AT homopolymers were collected in the diffraction angular range of $3^\circ \le 2\theta \le 36^\circ$ by a Bruker-AXS D8 Discover microdiffractometer with a Cu Kα radiation source. The crystalline peaks were deconvoluted using GADDS processing software. Bulk wide angle X-ray scattering (WAXS) copolymer samples were prepared by melt pressing polymer into 1 mm thick aluminum washers and thermally annealed under nitrogen at 20°C below the melting transition for 10 minutes. Room temperature WAXS experiments were conducted at beamline 1-4 of the Stanford Synchrotron Radiation Laboratory (SSRL) equipped with a Rayonix165 CCD detector. Two-dimensional diffraction images were radially averaged calibrated using a silver behenate (AgBe) standard.

Atomic force microscopy (AFM) images were taken with a Veeco Metrology (previously Digital Instruments) Nanoscope IIIa Multimode microscope operating in tapping mode in the repulsive regime in ambient atmosphere. The probe tips were fabricated by Nanosensors (Pointprobe-Plus Silicon SPM Sensor tips, resonant frequency 146–236 kHz, and spring constant 21–98 N/m).

2.2.4 Optoelectronic Property Characterization

Ultraviolet-Visible (UV-Vis) Spectroscopy Measurements. UV-Vis measurements were made with Varian Cary 50 instrument between 300 and 900 nm. Thin films were prepared by spin coating at 1500 rpm from 1 wt% polymer solutions in chlorobenzene on either glass or silicon substrates. Films were annealed at 20°C below the melting transition under argon for 1 minute.

Organic Field-Effect Transistor Fabrication and Measurements. Bottom-gate, top-contact organic field-effect transistors (OFETs) were fabricated entirely in inert atmosphere glove box. To begin, a 10 mg P3AT per 1 mL anhydrous chloroform solution was deposited onto an 300 nm thermally grown Si/SiO_2 substrate (Silicon Valley Microelectronics) and spun-coat at a rate of 1000 rpm for 1 min. Top contacts were also deposited in the glove box by placing the samples to an Mbraun glove box evaporator (base pressure ~3 x 10^{-6} mbar) with a Sigma Instruments SQC-310 deposition controller. Gold (99.999%) contacts (80 nm final thickness) were evaporated onto the polymer films at a rate of 0.01–0.1 nm/sec as measured by a quartz crystal monitor (QCM). Current-voltage characteristics were measured using an Agilent HP 4156C Precision semiconductor parameter analyzer connected to Model 72A-24/10 probe tips (American Probe and Technologies) that were mounted on a Newport testing stage. Data was collected using and stored using home-written LabView source code. All measurements were acquired in an inert atmosphere glove box in the dark.

2.3 Results and Discussion

2.3.1 Poly(3-alkylthiophene) Homopolymer Synthesis and Characterization

Regioregular, low polydispersity P3ATs were prepared using the Grignard metathesis (GRIM) method developed by the McCullough group (Figure 2.1).[35-36] Low polydispersity samples of each P3AT homopolymer were synthesized and their properties are summarized in Table 2.1. Regioregularity was confirmed by ^1H NMR analysis and molecular weights of polymers were determined by end group analysis and GPC (against polystyrene standards) was used to ascertain polydispersity index. Molecular weights were controlled so that the number of thiophene repeat units is approximately matched across all three polymer series.

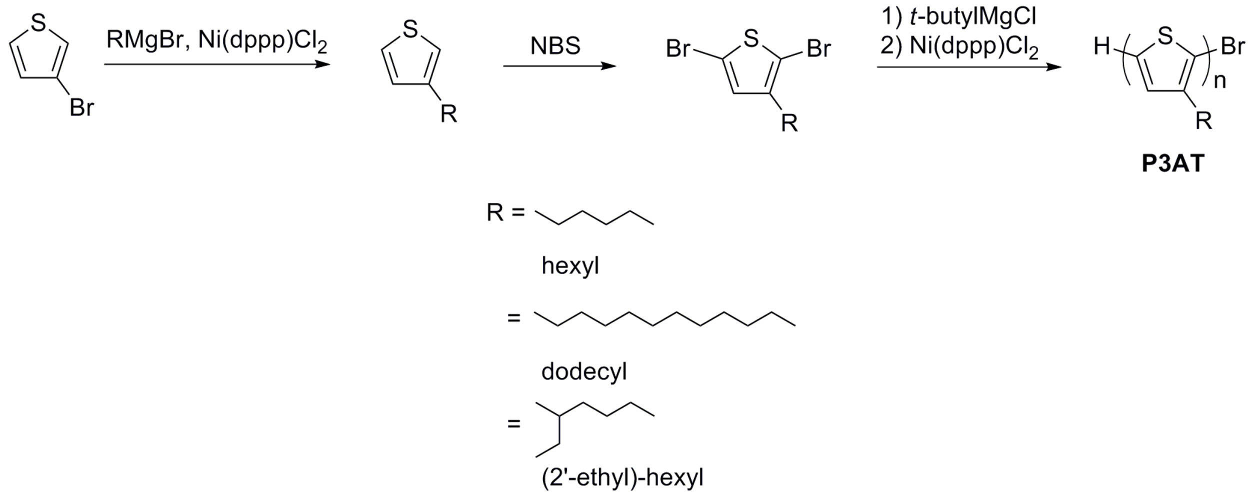

Figure 2.1: Synthetic scheme of P3AT by the GRIM method

Synthesis of poly(3-alkylthiophenes) by the Grignard Metathesis method developed by McCullough and coworkers. Note that the synthesis of copolymers follows the same scheme but with a mixture of the 2,5-dibromo-3-alkylthiophene in the reaction vessel (not pictured).

Table 2.1: Summary of P3AT homopolymer sample characteristics

Sample[a]	M_n (kg/mol)[b]	M_w/M_n[c]	T_m (°C)[d]	*FET Mobility*[f] ($\mathrm{cm^2\,V^{-1}s^{-1}}$)
P3HT-43	7.1	1.1	224	$1.5\text{x}10^{-3}$
P3HT-55	9.1	1.1	234	$2.3\text{x}10^{-4}$
P3HT-73	12.1	1.1	236	$1.3\text{x}10^{-3}$
P3DDT-30	7.5	1.3	157	$8.3\text{x}10^{-5}$
P3DDT-50	12.6	1.2	164	$1.6\text{x}10^{-4}$
P3DDT-79	19.9	1.2	169	$5.7\text{x}10^{-5}$
P3EHT-37	7.4	1.2	78[e]	$2.9\text{x}10^{-5}$
P3EHT-54	10.5	1.2	83[e]	$2.3\text{x}10^{-4}$
P3EHT-65	12.6	1.2	89[e]	$1.5\text{x}10^{-4}$

[a] P3AT-X indicates the polymer has an X average number of thiophene repeat units per chain. [b] As determined by ^{1}H NMR spectroscopy. [c] As determined by SEC versus polystyrene standards. [d] Main chain melting transition temperatures, as determined from DSC. [e] Melting temperature reported as the peak value of the highest temperature endotherm. Multimodal melting is evidence of the presence of melt-recrystallization in these samples. F Mobilities were calculated in the saturation regime and averaged over at least three devices.

Differential scanning calorimetry (DSC) data (Figure 2.2a) show that the alkyl chain architecture has a significant effect on the melting transition temperature of the polymers. Thermograms for P3HT indicate that the main chain melting transitions occur over the range 224-236 °C, depending on molecular weight of the polymer. When the number of alkyl groups in the side chain is increased from six to twelve in P3DDT, the melting transition decreases to between 157 and 169 °C. A broad secondary peak between 20 °C and 80 °C is consistent with previous literature reports of the melting of interdigitated dodecyl side chains.[37] Introducing the branched architecture of the 2-ethylhexyl side chain further depresses the main chain melting transition temperature. When annealed at temperatures below the melting transition temperature for at least an hour, P3EHT shows two distinct peaks between 70 and 90 °C. It should be noted that if P3EHT is not allowed sufficient time to crystallize (for example if a film is cast directly from solvent or a powder is measured immediately after drying from solvent), no melting is observed suggesting that this polymer has relatively slow crystallization kinetics which will be explored in the following chapter. Therefore, reports of the thermal transitions of P3EHT are highly dependent on thermal history.[34]

The multiple endotherms near the final melting in P3EHT is not unique to this particular P3AT as shoulders appear on the low temperature region of the melting endotherms of P3DDT and P3HT samples though they are not as well resolved. While tempting to assign such a behavior to side chain melting in P3EHT (as the temperature is near that of side chain melting in P3DDT), side chain crystallization is not expected due, in part, to the irregular geometry imparted by the stereocenter at the 2-carbon of the hexyl side chain. Multiple endotherms have been observed in other semicrystalline polymers in the past and the phenomenon has been attributed to a melt-recrystallization process in which smaller or less perfect crystallites present in the original sample melt and quickly recrystallize to form more thermodynamically stable crystallites.[38-40] Not all crystallites that melt recrystallize, and the difference between the heat absorbed by melting crystallites and heat released by chains recrystallizing results in the lower temperature endotherm. Upon further heating the newly formed crystallites will then melt at a higher temperature, accounting for the observation of the second endotherm. Furthermore, as expected for a melt-recrystallization process, the relative area of the endotherms in P3EHT can be manipulated with varying the scan rate, the crystallization temperature, and thermal annealing.[41]

While P3EHT has a depressed melting transition, its crystalline structure as determined by powder x-ray diffraction (XRD) (Figure 2.2b) is similar, though not identical, to that of P3HT.[42] Reflections for P3AT homopolymers can be found in Table 2.4 of the Appendix. The unit cells for P3HT and P3DDT have been presented in literature as orthorhombic cells with observable reflections from backbone spacing and π-π stacking.[23,43-44] The (100) reflection of P3HT, which measures distance between backbones across alkyl chains, is present at 3.6 nm^{-1}, corresponding to a lattice spacing of 1.74 nm; peaks consistent with the (200) and (300) reflections are present also. The (020) reflection, measuring the spacing of π-π stacking between thiophene rings, can be seen as a broad hump with a distinct peak at 15.9 nm^{-1}. As expected, P3DDT patterns show (100), (200), and (300) peaks at 2.5, 4.9, 7.3 nm^{-1} at larger domain spacings than those in P3HT patterns due to the longer side chain; a peak at 15.5 nm^{-1}, which corresponds to the (010) plane is consistent with the π-π stacking distance reported in the literature.[43-45] Powder XRD patterns (Figure 2.2b) demonstrate that P3EHT is semicrystalline, similar to the other polythiophene derivatives, and has a similar packing motif as that of P3HT

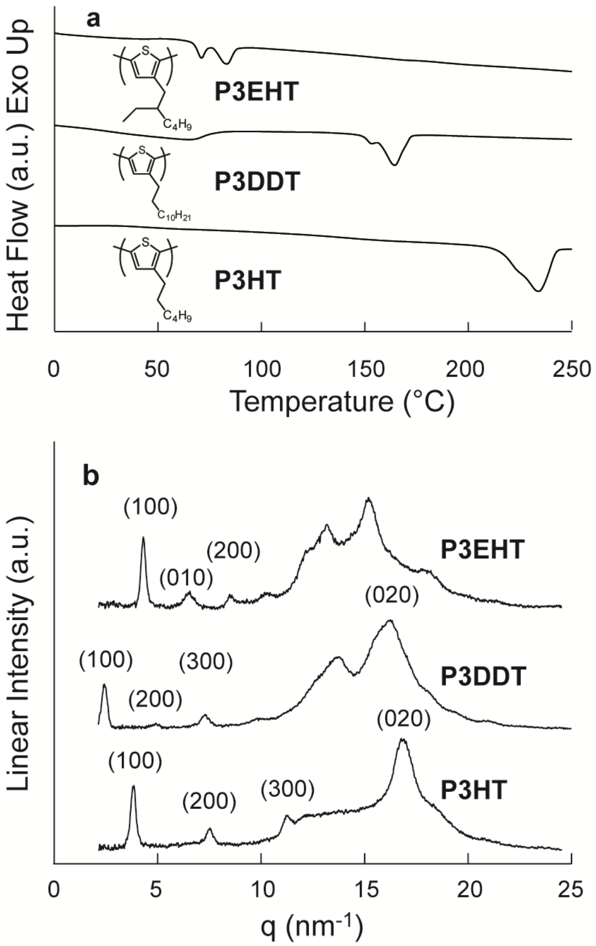

Figure 2.2: Differential scanning calorimetry and x-ray diffraction data for P3ATs

(a) DSC thermograms of representative P3HT, P3DDT, and P3EHT polymers at a heating rate of 10 °C/min. The chemical structures of the three polymers are inset in the figure. (b) XRD powder patterns for representative P3HT, P3DDT, and P3EHT. The prominent lamellae reflections are labeled as (*h*00). For P3HT and P3DDT, the (020) has been assigned to the *π*-*π* stacking direction of the commonly-reported orthorhombic unit cell.[46-47]

and P3DDT, but with a slightly different lattice. The (100) reflection of P3EHT is located at 4.1 nm^{-1}, which indicates slightly smaller lattice alkyl spacing than in P3HT. However, the (010) reflection is shifter to a lower q-value relative to both P3DDT and P3HT with a peak at 6.3 nm^{-1}. Though it is tempting to assign this peak to a reflection [namely, the (300)] of an integer multiple of the (100) reflection with half the magnitude of the currently proposed reciprocal lattice vector, a peak corresponding to a (100) reflection for such an assignment is not observed at lower angles and this reflection is found to be along a different reciprocal lattice direction from GIXD.[48] Furthermore, it should be noted that although the XRD patterns are similar to those found in P3HT samples with multiple polymorphs, temperature-resolved WAXS for P3EHT of multiple molecular weights do not show either solid-solid transitions or melting of different polymorphs.[41] Therefore the unit cell of P3EHT shows similarities with that of P3ATs with normal alkyl side chains, but it is slightly different, most notably in an expansion in the π-stacking direction.

In addition to DSC and XRD data, which confirm that all of the P3ATs in this study are in fact semicrystalline, tapping mode atomic force microscopy (AFM) images show the semicrystalline morphology of the P3ATs in thin film form a percolating network of nanofibrils (Figure 2.3), in agreement with literature reports.[22] In representative images, fibrils in P3HT-55 (Figure 2.3a) and P3EHT-37 (Figure 2.3b) have widths of ~32 nm and ~15 nm, respectively. Interestingly, the lengths of the P3HT nanowires are dramatically longer than in the P3EHT case. This difference in nanofibril length between P3ATs may affect the charge transport in these materials.

Despite the larger π-π packing distance of P3EHT (relative to P3HT and P3DDT) the optoelectronic properties show similar behavior upon crystallization, as evidenced by UV-Vis light absorption spectroscopy and field-effect transistor (FET) mobilities. As shown in Figure 2.4a, the global maximum absorbance values for P3HT and P3DDT solutions in chloroform are located at 450 nm while the P3EHT maximum is slightly blue shifted to 440 nm. This suggests that the branched alkyl chain architecture in P3EHT may introduce slight twists in the thiophene backbone, which occasionally disrupt conjugation.[49-50] Upon casting into thin films from chloroform the UV-Vis spectra of all the P3ATs were red-shifted and a vibronic shoulder became evident at lower energies (Figure 2.4b). The thin film absorption profiles for P3DDT and P3HT (Figure 2.4b) are identical, except that P3HT has a larger maximum absorption coefficient, consistent with previous reports.[24,51] P3EHT also shows a similar profile with an almost identical maximum absorption coefficient as P3DDT. However, the vibronic shoulder for P3EHT is blue-shifted 30 nm suggesting a decrease in the conjugation length in the solid state; this causes the optical band gap of P3EHT to be ~0.1 eV greater than the band gaps of P3HT and P3DDT. While not identical, the UV-vis absorption profiles obtained for P3EHT shows similar phenomenon upon crystallization as those of P3HT and P3DDT.

Charge transport in these materials was compared by fabricating OFETs with each of the polymers as the active layer, the results of which are summarized in Table 1. P3HT OFETs exhibited hole mobilities of μ_h ~10^{-3} $cm^2\ V^{-1}s^{-1}$, while P3DDT showed mobilities which were one order of magnitude lower on average, consistent with previous reports for relatively low molecular weight[52] P3HT and P3DDT. The hole mobility of P3DDT has been seen to be lower than P3HT due into the larger lattice spacing in both the (100) and (010) directions.[53] P3EHT showed similar hole mobilities (μ_h ~10^{-4} $cm^2\ V^{-1}s^{-1}$). Relative to P3HT, P3EHT has similar (100) spacing to P3HT, but a larger π-π-stacking distance. Therefore, it is not surprising that the overall

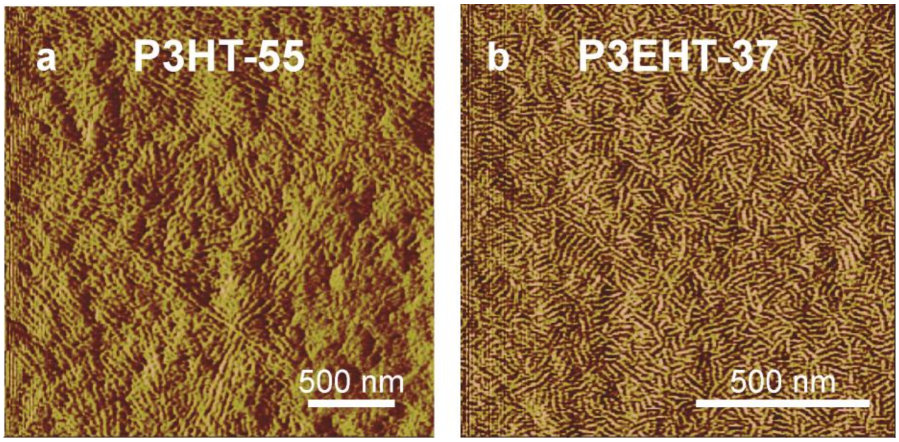

Figure 2.3: Atomic force microscopy images for P3HT and P3EHT

Atomic force microscopy tapping mode images of (a) P3HT-55 and (b) P3EHT-37 thin films showing the nanofibril microstructures present in both P3AT materials. Note that the lengths of the fibers in the P3HT sample are longer than in the P3EHT sample. Films were fabricated by spin-coating a 10 mg of polymer per 1 mL of chloroform solution at 1000 rpm for 1 min onto a silicon dioxide substrate. Final thin film thicknesses were ~80 nm as measured by profilometry.

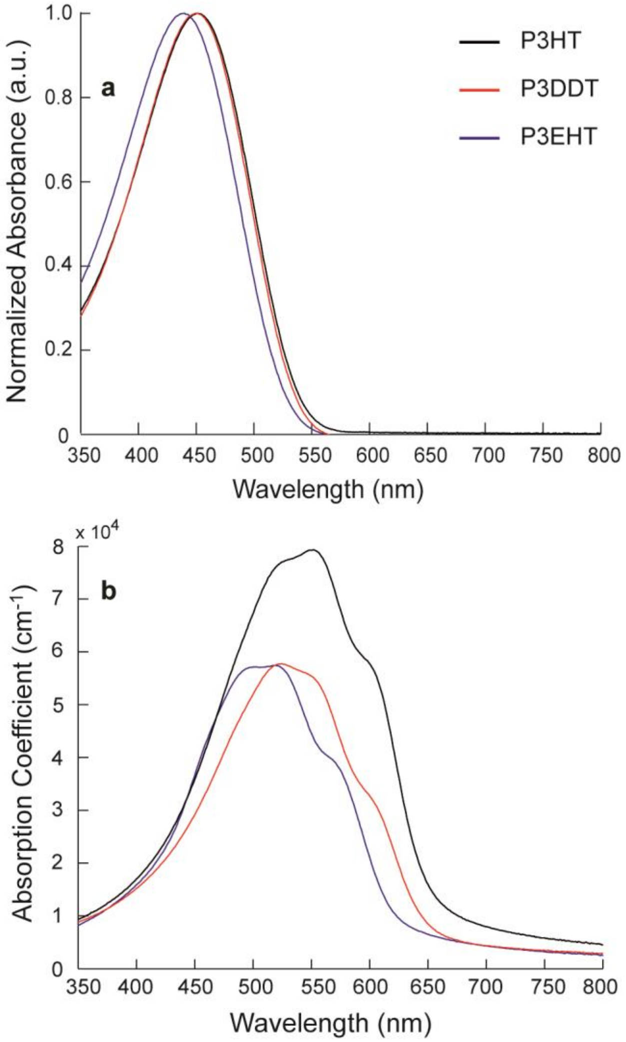

Figure 2.4: Solution and thin film UV-vis absorption spectra for P3AT homopolymers

UV-Vis light absorption profiles of P3HT (black), P3DDT (red), and P3EHT (blue) (a) in chloroform solutions and (b) cast as thin films. The solution concentration was 10 μg of polymer per 1 mL of chloroform. Thin films were fabricated by spin-coating from 10 mg of polymer per 1 mL of chloroform solutions at 2000 rpm for 1 min onto a glass substrate. All film thicknesses were ~60 nm, as measured by profilometry. The absorbance profile in both solution and thin film show that P3DDT and P3HT have the same optical band gap though P3EHT is blue-shifted. In solution this reflects a difference in the conjugation length of the P3ATs.

mobility of P3EHT is slightly lower than that of P3HT. It is surprising, however, to note that the incorporation of the bulkier, branched side chain and resultant increased (010) spacing does not appear to be any more detrimental to the field-effect mobility than increasing the straight chain length from to twelve carbons in P3DDT. Given that P3DDT has previously been demonstrated to have promising properties in both transistor and photovoltaic devices, this suggests that P3EHT will also be a promising material for these applications.

2.3.2 Poly(3-alkylthiophene) Copolymer Synthesis and Characterization

Though P3EHT and P3HT have quite different thermal and optical properties, the polymers share similarities in the crystal packing motifs (from XRD) and meso-scale (from AFM) which may allow for cocrystallization of the components, similar to reports of other P3AT copolymers.[31] Copolymers of 3-(2-ethylhexyl)thiophene and 3-hexylthiophene were synthesized via the GRIM polymerization route developed by McCullough and coworkers[35] with a varying monomer ratios. As presented in Table 2.2, all copolymers were synthesized with low polydispersities and similar molecular weights. It should be noted, that due to proximity of ^{1}H NMR analogous resonances of the 3HT and 3EHT repeat units, the number average molecular weights of copolymers could not be determined with NMR. Therefore, molecular weights are reported by GPC against polystyrene standards which are known to slightly over represent the true value;[54] care should be taken when comparing homopolymer data between Section 2.3.1 and that presented in this section. The compositions of copolymers were determined by relative areas of peaks corresponding to the aromatic proton of the thiophene ring in the ^{1}H NMR spectroscopy and range from 35 to 70 mol% 3EHT.

As expected, the melting transitions of random copolymers are highly dependent on the 3EHT to 3HT composition. Figure 2.5b shows the melting transition temperatures for all polymers as a function of 3EHT composition obtained from the second heating scan in differential scanning calorimetry (DSC) traces (Figure 2.5a). Importantly, though DSC endotherms of the random copolymers are broad, no samples exhibit a second melting transition as would be expected for phase separation (and crystallization) of the two components. The melting transition of P3HT is at 228°C, while that of the P3EHT homopolymer is significantly lower at 76°C. P3EHT:P3HT-19 displays a melting transition at 198°C, 30°C lower than homopolymer P3HT. Further increasing the 3EHT content to 35 and 48 mol% 3EHT results in a decrease to 157 and 132°C, respectively. In contrast to these large variations in melting temperature, transitions of P3EHT:P3HT-61 and P3EHT:P3HT-70 are both within 25°C of P3EHT homopolymer, though the minority repeat unit contents of copolymers are comparable to that of P3EHT:P3HT-35.

Crystallinity of copolymers over the entire composition window (from the DSC data) suggests, though does not prove, that the repeat units are cocrystallizing. For copolymers that exhibit non-crystallizable defects, the melting transition temperatures will typically decrease quickly, and at modest compositions of the non-crystallizing component the polymers will be amorphous and no endotherm will be observed on melting.[55] This is due in part to the decreasing probability of finding crystallizable segments of sufficient length to form thermodynamically stable crystallites.[56] If the both components are crystallizable but excluded from the opposing crystallite, a eutectic-like behavior is observed as exclusion defects in copolymers decrease the melting transition temperature from both compositional endpoints; this results in a minimum for the melting as a function of composition.[57] In contrast, if both components are included within

Table 2.2: Summary of copolymer sample characteristics

Sample[a]	*P3EHT mol%*[b]	M_n[c] (kg/mol)	M_w/M_n[c]	T_m (°C)[d]	E_{0-0} (eV)[e]
P3HT	0	10.3	1.08	228	2.03
P3EHT:P3HT-19	18.5	14.7	1.10	198	2.03
P3EHT:P3HT-35	34.7	9.5	1.10	157	2.02
P3EHT:P3HT-48	47.7	8.8	1.08	132	2.03
P3EHT:P3HT-63	62.7	8.8	1.06	102	2.12
P3EHT:P3HT-70	69.5	9.2	1.14	89	2.12
P3EHT	100	7.6	1.09	76	2.13

[a] Copolymers named according to 3EHT mol% composition. [b]As determined by ^{1}H NMR spectroscopy. [c] As determined by gel permeation chromatography. Values given in polystyrene equivalents. [d] Melting temperatures determined by DSC. [e] Values determined by fit to the Spano model (details in Supplementary Information).

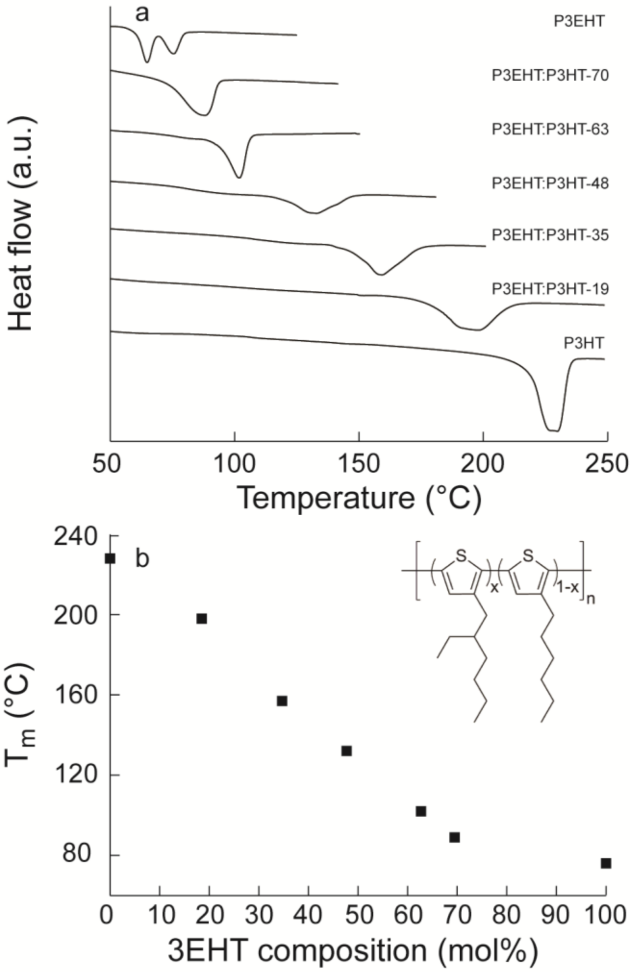

Figure 2.5: Thermal characterization of P3HT-P3EHT copolymers

(a) Differential scanning calorimetry heating traces (endotherm down) for copolymers showing a single melting transition for all copolymers. Traces are offset for clarity. Importantly though peaks are broad in most copolymers, the melting peaks shift systematically with the composition, and multiple endotherms indicative of phase separation are not observed in copolymer samples. (b) Melting temperatures as a function of 3EHT composition. The melting transition temperatures decrease monotonically with increasing 3EHT content. Chemical structure for P3EHT:P3HT-x is presented as an inset.

the crystallite, the melting transition temperature will be observed to decrease (due to enthalpic rather than entropic considerations)[58] less sharply and crystallization can occur over a much wider composition range.

Though the observation of semicrystallinity over the entire composition range is consistent with the co-inclusion scheme of crystallization, it is not in itself sufficient evidence as some polyester and polyamide copolymers of non-cocrystallizing components have been observed to be semicrystalline over a wide composition window.[57,59] Examination of the crystal structure of the copolymers can provide further evidence of co-crystallization and, more precisely, of isodimorphism. It is therefore imperative to investigate the crystalline structure in these polymers using wide-angle x-ray scattering (WAXS), presented in Figure 2.6. In the scattering profiles, most notably, a significantly large amorphous halo does not appear with increasing 3EHT suggesting that the degree of crystallinity does not decrease significantly across the composition, as observed in the case of defect exclusion for samples with large weight fractions of the non-crystallizable components.

Although the comparison of the degree of crystallinity is qualitative, examination of the crystal structure of the homopolymers and copolymers provides further evidence of inclusion. The different signatures in the WAXS for P3HT and P3EHT have been discussed in the previous section but are presented again for clarity and to underscore signatures of each unit cell. The pure P3HT profile (Figure 2.6) has peaks at 3.6, 7.3, 10.9 nm^{-1}, which correspond to the (h00) family of planes or the alkyl side chain spacing in P3ATs, and at a higher q value of 15.9 nm^{-1}, the (020) peak, corresponding to the π-π lattice dimension, is observed. In contrast, the pure P3EHT diffraction pattern exhibits reflections at 4.1 and 8.3 nm^{-1}, which are assigned to the alkyl chain dimension, and the non-integer peak at 6.3 nm^{-1} can be observed as well.

To understand the diffraction in copolymers, it is helpful to examine those with large mole fractions of 3HT and 3EHT separately. For copolymers with sufficiently high P3HT content (P3EHT:P3HT-19, P3EHT:P3HT-35, and P3EHT:P3HT-48), the copolymers adopt the P3HT orthorhombic unit cell as evidenced by nearly identical lattice spacings to that of pure P3HT and the lack of peaks between the (100) and (200) reflections. The (100) peaks for these copolymers have q-values of 4.1 nm^{-1} within experimental error, which is evidence that either the 3EHT units are not included in the P3HT crystallite or that incorporation of 3EHT repeat units does not increase the alkyl chain spacing of the adopted P3HT unit cell. This observation is not surprising even in the event of inclusion as side chain interdigitation in P3AT homopolymers is poor,[60] and the potential presence of a bulkier side chain may not provide the steric bulk required to disturb the spacing in this lattice dimension during growth of crystallites. However, the (020) reflection is shifted to lower q values for the P3EHT:P3HT-35 and P3EHT:P3HT-48 copolymers from 15.9 nm^{-1} for pure P3HT to 15.5 and 15.3 nm^{-1}, respectively. This corresponds to an increase in this lattice dimension from 3.95 Å for P3HT homopolymer to 4.11 Å at 48 mol% 3EHT. Furthermore, the breadth of the (020) peak increases with increased 3EHT content suggesting a decrease in the coherence length, likely dominated by paracrystallinity similar to observations in other semicrystalline polymers.[61-62] The systematic shift in the (020) peak to lower q with increased 3EHT content is strong evidence of inclusion, as P3EHT is known to exhibit a larger π-stacking distance (Figure 2.2b). Additionally, the increased paracrystalline disorder in that dimension suggests a broader distribution of spacings within the crystallite unit cell, potentially from the distribution of both 3HT and 3EHT repeat units in the crystallite. The hypothesis of both repeat units of the copolymer included within the crystallites becomes

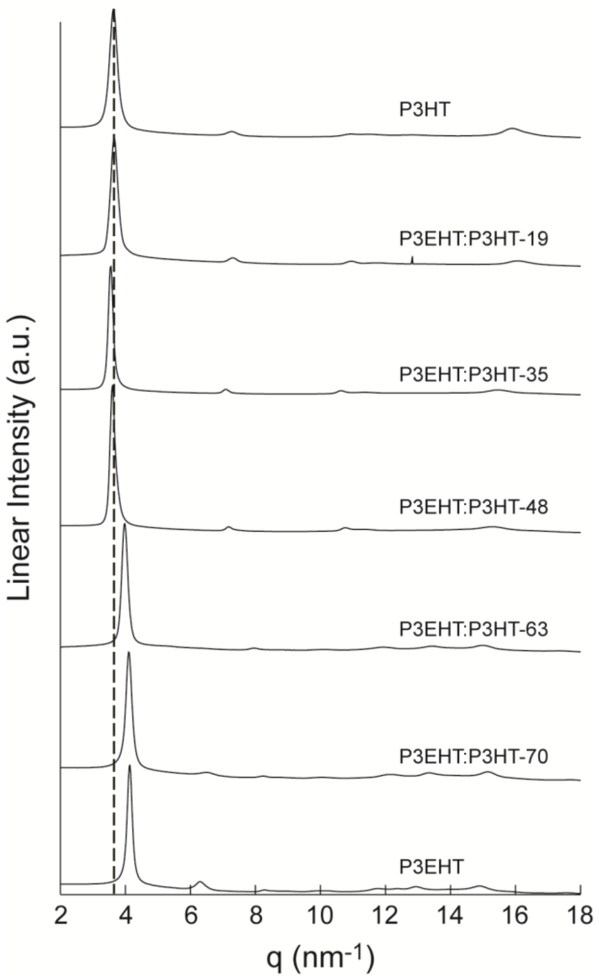

Figure 2.6: Wide-angle x-ray scattering profiles for P3EHT:P3HT copolymers

WAXS profiles for homopolymers and copolymers. Profiles are offset for clarity. Below 50 mol% P3EHT, the conventional orthorhombic P3HT unit cell is observed with no changes to the (*h*00) family of planes (the 100 is highlighted with the dashed line). A small shift to smaller q is observed in the (020) reflection of P3EHT:P3HT-35 and P3EHT:P3HT-48 suggesting a small expansion of the unit cell is necessary to accommodate the bulkier EHT side chain. Alternatively, above 63 mol% P3EHT, a shift in the (100) to higher q and higher order reflections are observed, indicative of the triclinic unit cell observed in homopolymer P3EHT.

stronger upon inspection of the 3EHT-rich copolymers. Unlike 3HT-rich copolymers, the crystal structures of the copolymers with higher compositions of 3EHT (P3HT:P3HT-63 and P3EHT:P3HT-70) are not identical to that of P3HT homopolymer. At 63 and 70 mol% 3EHT the (*h*00) family of planes lie at the same positions as P3EHT homopolymer, and reflections at non-integer multiples of the (100) peak are observed. Peaks at higher q are also observed at reciprocal spacings identical to the P3EHT homopolymer, providing further evidence that the copolymer adopts the P3EHT unit cell. Though it is tempting to suggest that the observation of identical diffraction patterns for the P3EHT:P3HT-70 and P3EHT homopolymer may indicate that the 3HT units are not incorporated into the crystalline P3EHT domains (such that the copolymer diffraction corresponds solely to pure P3EHT crystallites), the melting transition for the copolymers is not depressed as would be expected for the exclusion model of crystallization in random copolymers and the percent aggregates is not significantly decreased.[56] In fact, the monotonic decreasing melting transition temperature in addition to the change in the unit cell (isodimorphism)[63-64] has been observed in multiple systems that exhibit inclusion of both repeat units within crystallites including polyolefins,[65-67] isotactic polystyrene,[68] polyimides,[69] and polyamide[70] copolymers.

Interestingly, though isodimorphism has been observed in many semicrystalline polymers, the effect on optical properties has not been as studied as isodimorphism in conjugated polymers has not been as widely investigated. It is well-known that optoelectronic properties are inherently tied to the crystal structure of a material and the abrupt change in the unit cell should be accompanied by a change in the optical properties.[71-72] Figure 2.7 shows normalized UV-vis absorption profiles of random copolymer thin films. Though the difference in the absorption onset is clear from these data, fits to the model of the absorption from aggregates in the weak excitonic coupling regime developed by Spano provide a quantitative comparison between the absorption profiles.[73-75] The absorption data was fit to (Equation 2.1),

$$A \propto \sum_m \left(\frac{e^{-S} S^m}{m!} \right) \left(1 - \frac{We^{-S}}{2E_p} \sum_{n \neq m} \frac{S^n}{n!(n-m)} \right)^2 \exp\left(- \frac{\left(E - E_{0-0} - mE_p - \frac{1}{2} W S^m e^{-S} \right)^2}{2\sigma^2} \right) \tag{2.1}$$

where S is the Huang-Rhys factor (which has been set to 1 for this study), m and n are vibrational states, W is the excitonic bandwidth, E_p is the energy of the C=C stretching mode, E_{0-0} is the energy of the 0-0 transition, and σ is the Gaussian line width. In particular, a comparison of the 0-0 transition energy provides a spectroscopic quantity to compare the “gas-to-crystal shifts” induced by differences in copolymer crystal structures (Figure 2.2b). Due to the complex origin of the excitonic bandwidth, *W*, a parameter which has been shown to be dependent on morphological features on multiple length scales, the value is only of interest in the context of this work as a validation of the weak excitionic coupling assumption underlying the model. The model was fit to the collected absorption data in the regime dominated by aggregate absorption (1.93 to 2.25 or 2.03 to 2.35 for P3HT- or P3EHT-like aggregates).

Fits of Equation 2.1 to experimental data can be found in Figure 2.8 and fitting parameters can be found in Table 2.3. Although values for the P3HT homopolymer agree well with literature values for thin films cast from chlorobenzene,[76-79] the P3EHT homopolymer exhibits an absorbance profile which is blue-shifted by over 60 meV from that of P3HT, as noted in the previous section (Figure 2.4). Application of the Spano model to the P3EHT homopolymer

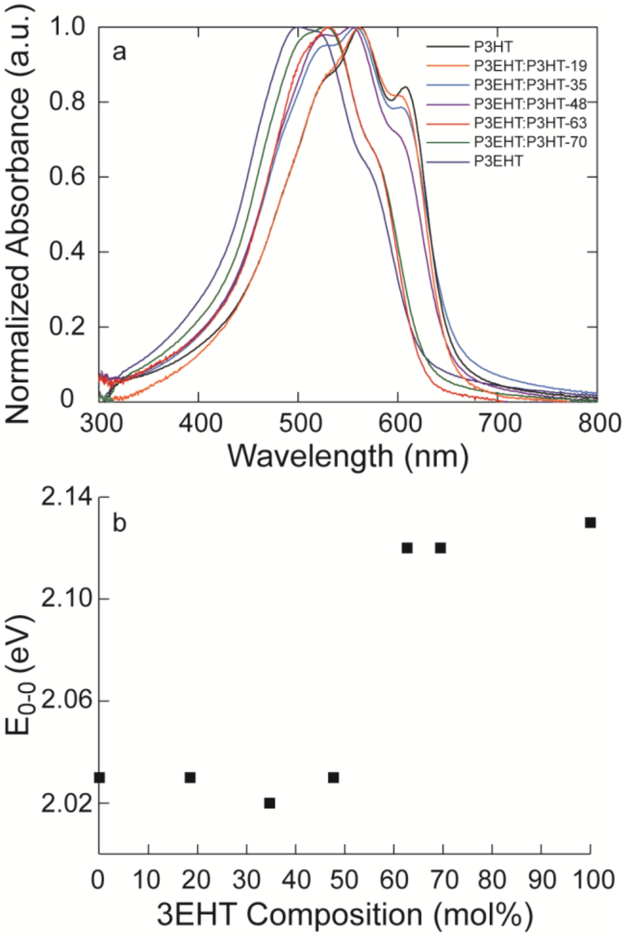

Figure 2.7: Optical characterization of P3EHT:P3HT copolymers

Optical properties for copolymers and homopolymers. (a) In the normalized UV-vis absorption profiles, the absorption edge for 3HT heavy copolymers align exactly, showing no difference in the band gap with increasing comonomer content. The band gap of the 3EHT heavy copolymers is blue shifted significantly from that of the other copolymers. (b) The energy of the 0-0 transition as a function of 3EHT composition. A large increase in the transition energy is observed as the 3EHT content increases beyond the symmetric composition.

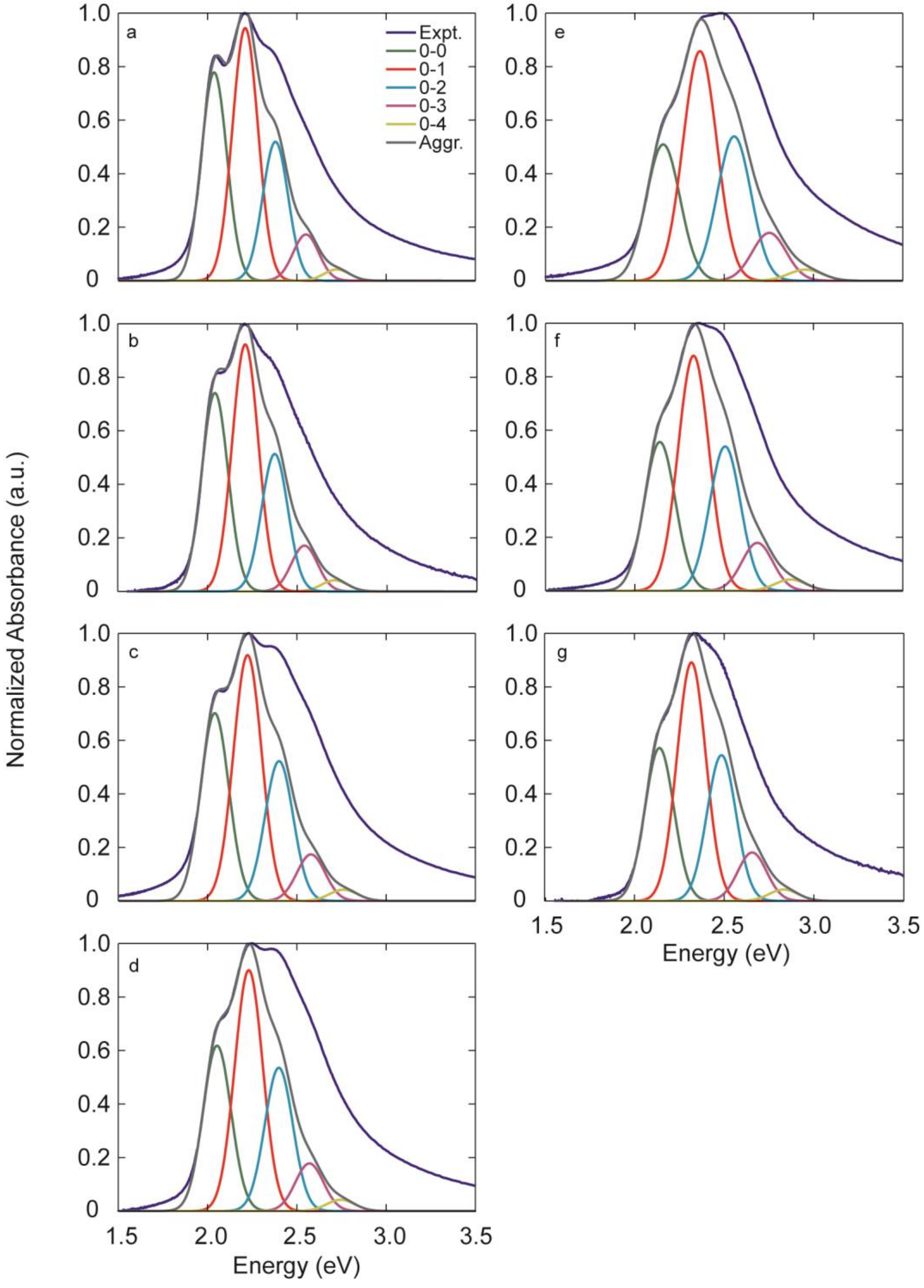

Figure 2.8: Fits to experimental optical absorption of P3EHT:P3HT copolymers

Representative UV-vis absorption profiles for (a) P3HT, (b) P3EHT:P3HT-19, (c) P3EHT:P3HT-35, (d) P3EHT:P3HT-48, I P3EHT, (f) P3EHT:P3HT-70, and (g) P3EHT:P3HT-63 with fits to Equation S1. Individual vibronic transitions are presented as green, red, teal, purple, and yellow curves the summation of which shown as a gray curve. Parameters for fits are collected in Table S1 as average and standard deviation of three thin films.

results in E_{0-0}, E_p, and W values slightly larger than that of P3HT, and though the energy of the vibrational transition and the excitonic bandwidth are larger than that presented for P3HT in this work, such values have been observed in thin films of P3HT in the past.[76] Importantly, the value of the excitonic bandwidth is still less than the energy of the vibrational transition, which indicates that the P3EHT homopolymer lies in the weak excitonic coupling regime and the Spano model is generally applicable.

Fits of Equation 2.1 to experimental data can be found in Figure 2.8 and fitting parameters can be found in Table 2.3. Although values for the P3HT homopolymer agree well with literature values for thin films cast from chlorobenzene,[76-79] the P3EHT homopolymer exhibits an absorbance profile which is blue-shifted by over 60 meV from that of P3HT, as noted in the previous section (Figure 2.4). Application of the Spano model to the P3EHT homopolymer results in E_{0-0}, E_p, and W values slightly larger than that of P3HT, and though the energy of the vibrational transition and the excitonic bandwidth are larger than that presented for P3HT in this work, such values have been observed in thin films of P3HT in the past.[76] Importantly, the value of the excitonic bandwidth is still less than the energy of the vibrational transition, which indicates that the P3EHT homopolymer lies in the weak excitonic coupling regime and the Spano model is generally applicable.

Unlike the continual decrease in melting transition temperature with increasing 3EHT content, parameters from the fit to the Spano model for the copolymers do not follow a simple monotonic trend. The copolymers can be divided into two groups: those with 0-0 transition energies similar to P3HT (P3EHT:P3HT-19, P3EHT:P3HT-35 and P3EHT:P3HT-48) and those nearer that of P3EHT (P3EHT:P3HT-63 and P3EHT:P3HT-70). We will first discuss the copolymers with high P3HT content that adopt the P3HT unit cell. P3EHT:P3HT-19, P3EHT:P3HT-35, and P3EHT:P3HT-48 have values of E_{0-0} and Gaussian linewidths that are almost identical to that of pure P3HT. That the energy of the 0-0 transition and disorder parameter are identical suggests that the 3EHT repeat units included within the copolymer aggregate region are electronically indistinguishable from that of 3HT. This is not surprising, as the only difference between monomers is in the optically-inactive alkyl component. Similar observations with copolymer composition can be made at for copolymers with majority 3EHT as well. P3EHT:P3HT-63, P3EHT:P3HT-70 and P3EHT have similar transitions which are nearly 100 meV removed from that of P3HT. Gaussian linewidths are also comparable amongst this group of random copolymers, though the P3EHT homopolymer is approximately 15 meV larger than those of the P3HT-rich copolymers.

The crystalline structural from the WAXS and the optical properties from the UV-vis absorbance are consistent and show the importance of the unit cell adopted on the optical properties. The first group (P3EHT:P3HT-19, P3EHT:P3HT-48, and P3EHT:P3HT-35) maintain the P3HT orthorhombic unit cell although the d-spacing of the (020) increases with increasing 3EHT content. This agrees with the observed trend that these polymers have the approximately the same E_{0-0} and line widths in UV-vis spectra. In the P3EHT-heavy compositions, the diffraction and UV-vis spectra are significantly different from that of the P3HT homopolymer. The energy of the 0-0 transition abruptly increases by nearly 100 meV once the unit cell transitions away from the P3HT unit cell. As the content is increased from 63 to 70 mol% 3EHT, slight changes in the unit cell result in a blue-shift in the absorption profile as well, further supporting that the absorption profile is intimately tied to the unit cell adopted by the P3AT. In contrast with the work of Jenekhe and coworkers in which only the (100) dimension was altered, the observed change in the unit cell results in increases to the π-π stacking dimension which affects the optical band gap of the material.

2.4 Conclusions

This chapter has illustrated the important role of alkyl side chains on the crystal structure and optoelectronic properties in P3ATs. Initially introduced to aid in the solubilization of the conjugated core, in the solid state these alkyl side chains present steric considerations which result in variations in the unit cell the subsequent macroscopic properties. In the case of homopolymers, straight and branched side chain P3ATs with narrow molecular weight distributions have been synthesized using the GRIM method. DSC, powder WAXS, and AFM confirm that P3EHT is a semicrystalline polymer, similar to P3HT and P3DDT; a fact which can be overlooked if relying solely on DSC data acquired at a fast heating rate. Powder XRD spectra showed lattice spacings which vary with the length and architecture of the alkyl side chain. Introducing a branch in the P3EHT case slightly increases the (010) spacing relative to the P3HT and P3DDT cases. UV-Vis absorbance spectroscopy and FET mobility measurements demonstrate that P3EHT has similar, though not identical, optoelectronic properties to P3HT and P3DDT.

The importance of the side chain architecture is underscored upon examination of copolymers of the 3HT and 3EHT unit cells. 3-Hexylthiophene and 3-(2-ethylhexyl)thiophene units cocrystallize when randomly copolymerized over all compositions and adopt a crystalline structure nearly identical to that of one of the homopolymers. In these cases, the optical band gap for the copolymers and the corresponding homopolymer indicate that both thiophene repeat units are conjugated along the backbone and electronically indistinguishable in the crystalline domains. Our observations of isodimorphism in P3AT copolymers plant these conjugated copolymers within the context of well-established literature while providing a platform for investigating fundamental structure-property relationships. From the data, it can be determined that the aliphatic side chain in P3ATs, though optoelectronically inactive, plays an important role in dictating the crystalline packing in the solid state. While changes in the alkyl chain dimension have been observed in the past and that this does not affect the optical absorbance in such systems, this work highlights that drastic changes to the crystalline structure can be effected which result in subsequent shifts in the absorbance spectra. Overall, the P3EHT-P3HT copolymer system rather elegantly illustrates the correlation between the optical properties and crystalline structure of P3ATs and provides a simple synthetic handle for modifying the melting transition temperature over a range of 96°C without affecting the absorbance edge.

Acknowledgements. We gratefully acknowledge support through an NSF CAREER award for the synthesis and characterization of structure of homopolymer P3ATs and support through the DOE-Office of Basic Energy Sciences Plastic Electronics Program at Lawrence Berkeley National Laboratories for device fabrication and characterization. The copolymer work was supported by the National Science Foundation under Grant No. 1206296. Victor Ho gratefully acknowledges the National Science Foundation for a graduate fellowship. Device fabrication and characterization was performed at the Molecular Foundry, a Lawrence Berkeley National Laboratory user facilities supported by the Office of Science, Office of Basic Energy Sciences, U.S. Department of Energy, under Contract No. DE-AC02-05CH11231.

2.5 Appendix

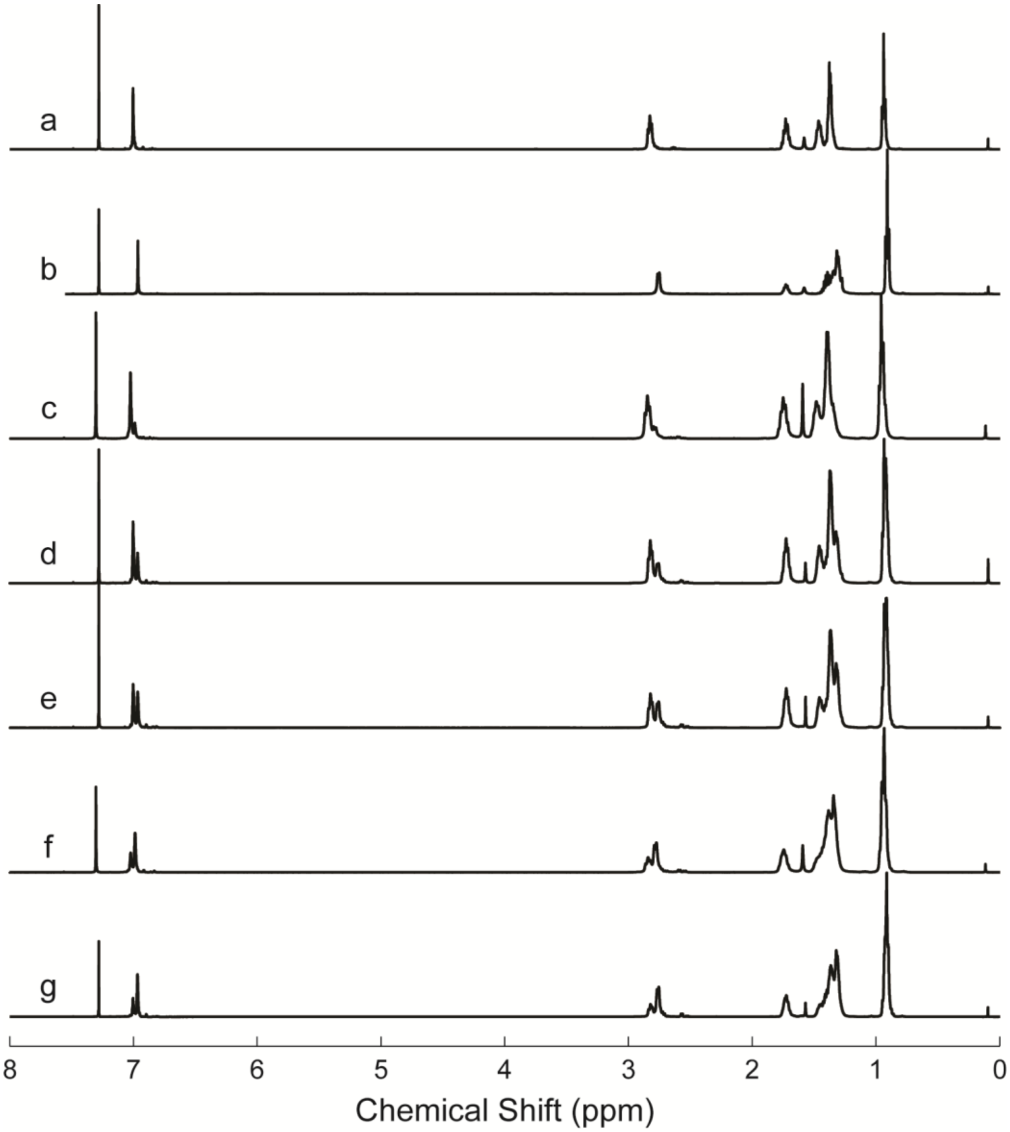

Figure 2.9: ^{1}H NMR spectra of P3EHT-P3HT copolymers

^{1}H NMR of spectra of (a) P3HT, (b) P3EHT, (c) P3EHT:P3HT-19, (d) P3EHT:P3HT-35, I P3EHT:P3HT-48, (f) P3EHT:P3HT-63, and (g) P3EHT:P3HT-70. Random copolymer composition was determined from the relative peak areas of resonances in the aromatic proton region.

Table 2.3: Fitting parameters to UV-vis spectra of thin films

Sample	W (meV)	$E_{0\text{-}0}$ (eV)	E_p (meV)	σ (meV)
P3HT	55	2.03	176	73
P3EHT:P3HT-19	57	2.03	169	73
P3EHT:P3HT-35	90	2.02	185	80
P3EHT:P3HT-48	102	2.03	179	79
P3EHT:P3HT-63	118	2.12	178	80
P3EHT:P3HT-70	129	2.12	190	87
P3EHT	157	2.13	205	94

Table 2.4: Crystalline reflections of homopolymers and copolymers

Sample	*100* (nm^{-1})	*010* (nm^{-1})[a]	*020* (nm^{-1})[a]	*200* (nm^{-1})
P3HT	3.6	-	15.9	7.2
P3DDT	2.5	-	15.5	4.9
P3EHT	4.1	6.3	-	8.3
P3EHT:P3HT-19	3.7	-	16.0	7.3
P3EHT:P3HT-35	3.5	-	15.5	7.1
P3EHT:P3HT-48	3.6	-	15.3	7.2
P3EHT:P3HT-63	4.0	5.5	-	8.0
P3EHT:P3HT-70	4.1	6.5	-	8.2

[a] Empty values are either disallowed by symmetry or difficult to assign due to large peak widths from disorder within polymer crystallites.

2.6 References

1. McCullough, R. D. The Chemistry of Conducting Polythiophenes. *Adv Mater* **1998,** *10* (2), 93.

2. Osaka, I.; McCullough, R. D. Advances in Molecular Design and Synthesis of Regioregular Polythiophenes. *Accounts Chem Res* **2008,** *41* (9), 1202.

3. Thompson, B. C.; Frechet, J. M. J. Organic photovoltaics - Polymer-fullerene composite solar cells. *Angew Chem Int Edit* **2008,** *47* (1), 58.

4. Peet, J.; Heeger, A. J.; Bazan, G. C. "Plastic" Solar Cells: Self-Assembly of Bulk Heterojunction Nanomaterials by Spontaneous Phase Separation. *Accounts Chem Res* **2009,** *42* (11), 1700.

5. Elsenbaumer, R. L.; Jen, K. Y.; Oboodi, R. Processible and Environmentally Stable Conducting Polymers. *Synthetic Met* **1986,** *15*, 169.

6. Jen, K. Y.; Miller, G. G.; Elsenbaumer, R. L. Highly Conducting, Soluble, and Environmentally-Stable Poly(3-Alkylthiophenes). *J Chem Soc Chem Comm* **1986,** (17), 1346.

7. Mccullough, R. D.; Williams, S. P. Toward Tuning Electrical and Optical-Properties in Conjugated Polymers Using Side-Chains - Highly Conductive Head-to-Tail Heteroatom-Functionalized Polythiophenes. *J Am Chem Soc* **1993,** *115* (24), 11608.

8. Ogawa, K.; Stafford, J. A.; Rothstein, S. D.; Tallman, D. E.; Rasmussen, S. C. Nitrogen-functionalized polythiophenes: Potential routes to new low band gap materials. *Synthetic Met* **2005,** *152* (1-3), 137.

9. Hou, J. H.; Chen, T. L.; Zhang, S. Q.; Huo, L. J.; Sista, S.; Yang, Y. An Easy and Effective Method To Modulate Molecular Energy Level of Poly(3-alkylthiophene) for High-Voc Polymer Solar Cells. *Macromolecules* **2009,** *42* (23), 9217.

10. McCullough, R. D.; Ewbank, P. C.; Loewe, R. S. Self-assembly and disassembly of regioregular, water soluble polythiophenes: Chemoselective ionchromatic sensing in water. *J Am Chem Soc* **1997,** *119* (3), 633.

11. Viinikanoja, A.; Areva, S.; Kocharova, N.; Aaritalo, T.; Vuorinen, M.; Savunen, A.; Kankare, J.; Lukkari, J. Structure of self-assembled multilayers prepared from water-soluble polythiophenes. *Langmuir* **2006,** *22* (14), 6078.

12. Liu, J. S.; Kadnikova, E. N.; Liu, Y. X.; McGehee, M. D.; Frechet, J. M. J. Polythiophene containing thermally removable solubilizing groups enhances the interface and the performance of polymer-titania hybrid solar cells. *J Am Chem Soc* **2004,** *126* (31), 9486.

13. Zhao, Y.; Keroack, D.; Yuan, G. X.; Massicotte, A.; Hanna, R.; Leclerc, M. Melting behavior of poly(3-alkylthiophene)s with long alkyl side-chains. *Macromol Chem Phys* **1997,** *198* (4), 1035.

14. Malik, S.; Nandi, A. K. Crystallization mechanism of regioregular poly(3-alkyl thiophene)s. *J Polym Sci, Part B: Polym Phys* **2002,** *40* (18), 2073.

15. Sirringhaus, H.; Brown, P. J.; Friend, R. H.; Nielsen, M. M.; Bechgaard, K.; Langeveld-Voss, B. M. W.; Spiering, A. J. H.; Janssen, R. A. J.; Meijer, E. W.; Herwig, P.; de Leeuw, D. M. Two-dimensional charge transport in self-organized, high-mobility conjugated polymers. *Nature* **1999,** *401* (6754), 685.

16. Wang, G. M.; Swensen, J.; Moses, D.; Heeger, A. J. Increased mobility from regioregular poly(3-hexylthiophene) field-effect transistors. *J Appl Phys* **2003,** *93* (10), 6137.

17. Padinger, F.; Rittberger, R. S.; Sariciftci, N. S. Effects of postproduction treatment on plastic solar cells. *Adv Funct Mater* **2003,** *13* (1), 85.

18. Li, G.; Shrotriya, V.; Huang, J. S.; Yao, Y.; Moriarty, T.; Emery, K.; Yang, Y. High-efficiency solution processable polymer photovoltaic cells by self-organization of polymer blends. *Nat Mater* **2005,** *4* (11), 864.

19. Ma, W. L.; Yang, C. Y.; Gong, X.; Lee, K.; Heeger, A. J. Thermally stable, efficient polymer solar cells with nanoscale control of the interpenetrating network morphology. *Adv Funct Mater* **2005,** *15* (10), 1617.

20. Kuila, B. K.; Nandi, A. K. Structural hierarchy in melt-processed poly(3-hexyl thiophene)-montmorillonite clay nanocomposites: Novel physical, mechanical, optical, and conductivity properties. *J Phys Chem B* **2006,** *110* (4), 1621.

21. Liu, J. S.; Sheina, E.; Kowalewski, T.; McCullough, R. D. Tuning the electrical conductivity and self-assembly of regioregular polythiophene by block copolymerization: Nanowire morphologies in new di- and triblock copolymers. *Angew Chem Int Edit* **2001,** *41* (2), 329.

22. Zhang, R.; Li, B.; Iovu, M. C.; Jeffries-EL, M.; Sauve, G.; Cooper, J.; Jia, S. J.; Tristram-Nagle, S.; Smilgies, D. M.; Lambeth, D. N.; McCullough, R. D.; Kowalewski, T. Nanostructure dependence of field-effect mobility in regioregular poly(3-hexylthiophene) thin film field effect transistors. *J Am Chem Soc* **2006,** *128* (11), 3480.

23. Wu, Z. Y.; Petzold, A.; Henze, T.; Thurn-Albrecht, T.; Lohwasser, R. H.; Sommer, M.; Thelakkat, M. Temperature and Molecular Weight Dependent Hierarchical Equilibrium Structures in Semiconducting Poly(3-hexylthiophene). *Macromolecules* **2010,** *43* (10), 4646.

24. Boudouris, B. W.; Molins, F.; Blank, D. A.; Frisbie, C. D.; Hillmyer, M. A. Synthesis, Optical Properties, and Microstructure of a Fullerene-Terminated Poly(3-hexylthiophene). *Macromolecules* **2009,** *42* (12), 4118.

25. Muller, C.; Ferenczi, T. A. M.; Campoy-Quiles, M.; Frost, J. M.; Bradley, D. D. C.; Smith, P.; Stingelin-Stutzmann, N.; Nelson, J. Binary organic photovoltaic blends: A simple rationale for optimum compositions. *Adv Mater* **2008,** *20* (18), 3510.

26. van Bavel, S.; Sourty, E.; de With, G.; Frolic, K.; Loos, J. Relation between Photoactive Layer Thickness, 3D Morphology, and Device Performance in P3HT/PCBM Bulk-Heterojunction Solar Cells. *Macromolecules* **2009,** *42* (19), 7396.

27. Chen, L. M.; Hong, Z. R.; Li, G.; Yang, Y. Recent Progress in Polymer Solar Cells: Manipulation of Polymer: Fullerene Morphology and the Formation of Efficient Inverted Polymer Solar Cells. *Adv Mater* **2009,** *21* (14-15), 1434.

28. Beal, R. M.; Stavrinadis, A.; Warner, J. H.; Smith, J. M.; Assender, H. E.; Watt, A. A. R. The Molecular Structure of Polymer-Fullerene Composite Solar Cells and Its Influence on Device Performance. *Macromolecules* **2010,** *43* (5), 2343.

29. Olsen, B. D.; Segalman, R. A. Self-assembly of rod-coil block copolymers. *Mat Sci Eng R* **2008,** *62* (2), 37.

30. Ho, C. C.; Lee, Y. H.; Dai, C. A.; Segalman, R. A.; Su, W. F. Synthesis and Self-assembly of Poly(diethylhexyloxy-p-phenylenevinylene)-b-poly(methyl methacrylate) Rod-Coil Block Copolymers. *Macromolecules* **2009,** *42* (12), 4208.

31. Wu, P. T.; Ren, G.; Jenekhe, S. A. Crystalline Random Conjugated Copolymers with Multiple Side Chains: Tunable Intermolecular Interactions and Enhanced Charge Transport and Photovoltaic Properties. *Macromolecules* **2010,** *43*, 3306.

32. Zhang, Y.; Tajima, K.; Hashimoto, K. Nanostructure Formation in Poly(3-hexylthiophene-block-3-(2-ethylhexyl)thiophene)s. *Macromolecules* **2009,** *42*, 7008.

33. Burkhart, B.; Khlyabich, P. P.; Thompson, B. C. Influence of the Ethylhexyl Side-Chain Content on the Open-Circuit Voltage in rr-Poly(3-hexylthiophene-co-3-(2-ethylhexyl)thiophene) Copolymers. *Macromolecules* **2012,** *45*, 3740.

34. Zhang, Y.; Tajima, K.; Hirota, K.; Hashimoto, K. Synthesis of all-conjugated diblock copolymers by quasi-living polymerization and observation of their microphase separation. *J Am Chem Soc* **2008,** *130* (25), 7812.

35. Loewe, R. S.; Ewbank, P. C.; Liu, J.; Zhai, L.; McCullough, R. D. Regioregular, Head-to-Tail Coupled Poly(3-alkylthiophenes) Made Easy by the GRIM Method: Investigation of the Reaction and the Origin of Regioselectivity. *Macromolecules* **2001,** *34* (13), 4324.

36. Loewe, R. S.; Khersonsky, S. M.; McCullough, R. D. A simple method to prepare head-to-tail coupled, regioregular poly(3-alkylthiophenes) using grignard metathesis. *Adv Mater* **1999,** *11* (3), 250.

37. Liu, S. L.; Chung, T. S. Crystallization and melting behavior of regioregular poly(3-dodecylthiophene). *Polymer* **2000,** *41* (8), 2781.

38. Lemstra, P. J.; Schouten, A. J.; Challa, G. Secondary Crystallization of Isotactic Polystyrene. *J Polym Sci, Part B: Polym Phys* **1974,** *12*, 1565.

39. Strobl, G. Crystallization and melting of bulk polymers: New observations, conclusions and a thermodynamic scheme. *Prog Polym Sci* **2006,** *31*, 398.

40. Heck, B.; Siegenfuhr, S.; Strobl, G.; Thomann, R. A law controlling polymer recrystallization showing up in experiments on s-polypropylene. *Polymer* **2007,** *48*, 1352.

41. Beckingham, B. S.; Ho, V.; Segalman, R. A. **2014,** in preparation.

42. Note that no dependence of molecular weight on lattice spacing was observed for any of the polymers investigated.

43. Prosa, T. J.; Moulton, J.; Heeger, A. J.; Winokur, M. J. Diffraction line-shape analysis of poly(3-dodecylthiophene): A study of layer disorder through the liquid crystalline polymer transition. *Macromolecules* **1999,** *32* (12), 4000.

44. Causin, V.; Marega, C.; Marigo, A.; Valentini, L.; Kenny, J. M. Crystallization and melting behavior of poly(3-butylthiophene), poly(3-octylthiophene), and poly(3-dodecylthiophene). *Macromolecules* **2005,** *38* (2), 409.

45. Boudouris, B. W.; Frisbie, C. D.; Hillmyer, M. A. Nanoporous Poly(3-alkylthiophene) Thin Films Generated from Block Copolymer Templates. *Macromolecules* **2008,** *41*, 67.

46. Prosa, T. J.; Winokur, M. J.; Moulton, J.; Smith, P.; Heeger, A. J. X-ray Structural Studies of Poly(3-alkylthiophenes): An Example of an Inverse Comb. *Macromolecules* **1992,** *25*, 4364.

47. Lee, C. S.; Dadmun, M. D. Important thermodynamic characteristics of poly(3-hexyl thiophene). *Polymer* **2014,** *55* (1), 4.

48. Boudouris, B. W.; Ho, V.; Jimison, L. H.; Toney, M. F.; Salleo, A.; Segalman, R. A. Real-Time Observation of Poly(3-alkylthiophene) Crystallization and Correlation with Transient Optoelectronic Properties. *Macromolecules* **2011,** *44* (17), 6653.

49. Baughman, R. H.; Chance, R. R. Point Defects in Fully Conjugated Polymers. *J Appl Phys* **1976,** *47* (10), 4295.

50. Tashiro, K.; Ono, K.; Minagawa, Y.; Kobayashi, M.; Kawai, T.; Yoshino, K. Structure and Thermochromic Solid-state Phase Transition of Poly (3-alkylthiophene). *J Polym Sci Pol Phys* **1991,** *29*, 1223.

51. Thompson, B. C.; Kim, B. J.; Kavulak, D. F.; Sivula, K.; Mauldin, C.; Frechet, J. M. J. Influence of alkyl substitution pattern in thiophene copolymers on composite fullerene solar cell performance. *Macromolecules* **2007,** *40* (21), 7425.

52. Kline, R. J.; McGehee, M. D.; Kadnikova, E. N.; Liu, J.; Frechet, J. M. J.; Toney, M. F. Dependence of Regioregular Poly(3-hexylthiophene) Film Morphology and Field-Effect Mobility on Molecular Weight. *Macromolecules* **2005,** *38*, 3312.

53. Babel, A.; Jenekhe, S. A. Alkyl chain length dependence of the field-effect carrier mobility in regioregular poly(3-alkylthiophene)s. *Synthetic Met* **2005,** *148* (2), 169.

54. Wong, M.; Hollinger, J.; Kozycs, L. M.; McCormick, T. M.; Lu, Y.; Burns, D. C.; Seferos, D. S. An Apparent Size-Exclusion Quantification Limit Reveals a Molecular Weight Limit in the Synthesis of Externally Initiated Polythiophenes. *Acs Macro Letters* **2012,** *1*, 1266.

55. Mandelkern, L., *Crystallization of Polymers*, 2nd ed.; McGraw-Hill: New York, 2002; Vol. 1.

56. Flory, P. J. Thermodynamics of Crystallization in High Polymers. IV. A Theory of Crystalline States and Fusion in Polymers, Copolymers, and Their Mixtures with Diluents. *J Chem Phys* **1949,** *17* (3), 223.

57. Izard, E. F. The effect of chemical composition on selected physical properties of linear polymers. *J Polym Sci* **1952,** *8* (5), 503.

58. Sanchez, I. C.; Eby, R. K. Crystallization of Random Copolymers. *J Res Nat Stand Sec A* **1973,** *77A* (3), 353.

59. Edgar, O. B.; Ellery, E. 498. Structure-property relationships in polyethlene terephthalate co-polyesters. Part I. Melting points. *J Chem Soc* **1952,** (0), 2633.

60. Kline, R. J.; DeLongchamp, D. M.; Fischer, D. A.; Lin, E. K.; Richter, L. J.; Chabinyc, M. L.; Toney, M. F.; Heeney, M.; McCulloch, I. Critical Role of Side-Chain Attachment Density on the Order and Device Performance of Polythiophenes. *Macromolecules* **2007,** *40*, 7960.

61. Rivnay, J.; Noriega, R.; Kline, R. J.; Salleo, A.; Toney, M. F. Quantitative analysis of lattice disorder and crystallite size in organic semiconductor thin films. *Phys Rev B* **2011,** *84*, 045203.

62. Noriega, R.; Rivnay, J.; Vandewal, K.; Koch, F. P. V.; Stingelin, N.; Smith, P.; Toney, M. F.; Salleo, A. A general relationship between disorder, aggregation and charge transport in conjugated polymers. *Nat. Mat.* **2013,** *12*, 1038.

63. Allegra, G.; Bassi, I. W. Isomorphism in Synthetic Macromolecular Systems. *Adv Polym Sci* **1969,** *6*, 549.

64. Kamiya, N.; Sakurai, M.; Inoue, Y.; Chujo, R. Isomorphic Behavior of Random Copolymers: Thermodynamic Analysis of Cocrystallization of Poly(3-hydroxybutyrate-co-3-h ydroxyvalerate). *Macromolecules* **1991,** *24*, 3888.

65. Matsumoto, T.; Nakamae, K.; Ogoshi, N.; Kawasoe, M.; Oka, H. The Crystallinity of Ethylene-Vinyl Alcohol Copolymers. *Kobunshi Kagaku* **1971,** *28*, 610.

66. Nakamae, K.; Kameyama, M.; Matsumoto, T. Elastic Moduli of the Crystalline Regions in the Direction Perpendicular to the Chain Axis of Ethylene-Vinyl Alcohol Copolymers. *Polym Eng Sci* **1979,** *19* (8), 572.

67. Voigt-Martin, I. G.; Mandelkern, L., *Handbook of Polymer Science and Technology*, 1 ed.; Marcel Dekker Publishers: New York, 1989; Vol. 4.

68. Natta, G. Progress in the Stereospecific Polymerization. *Makromolekul Chem* **1960,** *35* (1), 94.

69. Kreuz, J. A.; Hsiao, B. S.; Renner, C. A.; Goff, D. L. Crystalline Homopolyimides and Copolyimides Derived from 3,3',4,4'-Biphenyltetracarboxylic Dianhydride/ 1,3-Bis(4-aminophenoxy)benzene/l,12-Dodecanediamine. 1. Materials, Preparation, and Characterization. *Macromolecules* **1995,** *28*, 6926.

70. Edgar, O. B.; Hill, R. The p-phenylene linkage in linear high polymers: Some structure–property relationships. *J Polym Sci* **1952,** *8* (1), 1.

71. Fox, M., *Optical Properties of Solids*, 2 ed.; Oxford University Press: 2010.

72. Kittel, C., *Introduction to Solid State Physics*, 8 ed.; John Wiley & Sons, Inc.: New York, 2004.

73. Turner, S. T.; Pingel, P.; Steyrleuthner, R.; Crossland, E. J. W.; Ludwigs, S.; Neher, D. Quantitative Analysis of Bulk Heterojunction Films Using Linear Absorption Spectroscopy and Solar Cell Performance. *Adv Funct Mater* **2011,** *21*, 4640.

74. Spano, F. C. Modeling disorder in polymer aggregates: The optical spectroscopy of regioregular poly„3-hexylthiophene thin films. *J Chem Phys* **2005,** *122,* 234701.

75. Spano, F. C. Absorption in regio-regular poly(3-hexyl)thiophene thin films: Fermi resonances, interband coupling and disorder. *Chem Phys* **2006,** *325*, 22.

76. Duong, D. T.; Toney, M. F.; Salleo, A. Role of confinement and aggregation in charge transport in semicrystalline polythiophene thin films. *Phys Rev B* **2012,** *86*, 205205.

77. Clark, J.; Silva, C.; Friend, R. H.; Spano, F. C. Role of Intermolecular Coupling in the Photophysics of Disordered Organic Semiconductors: Aggregate Emission in Regioregular Polythiophene. *Phys Rev Lett* **2007,** *98*, 206406.

78. Barnes, M. D.; Baghar, M. Optical Probes of Chain Packing Structure and Exciton Dynamics in Polythiophene Films, Composites, and Nanostructures. *J Polym Sci, Part B: Polym Phys* **2012,** *50*, 1121.

79. Niles, E. T.; Roehling, J. D.; Yamagata, H.; Wise, A. J.; Spano, F. C.; Moule, A. J.; Grey, J. K. J-Aggregate Behavior in Poly-3-hexylthiophene Nanofibers. *J. Phys. Chem. Lett.* **2012,** *3*, 259.

Chapter 3: Real-Time Observation of Poly(3-alkylthiophene) Crystallization and Correlation with Transient Optoelectronic Properties

Adapted from "Real-Time Observation of Poly(3-alkylthiophene) Crystallization and Correlation with Transient Optoelectronic Properties," B.W. Boudouris, V. Ho, L.H. Jimison, M.F. Toney, A. Salleo, R.A. Segalman, Macromolecules, 2011, 44(17), 6653-6658. (DOI: 10.1021/ma201316a) with permission from the authors. *Reproduced by permission of The American Chemical Society*

As discussed in Chapter 2, poly(3-(2-ethylhexyl)thiophene) (P3EHT) crystallizes at room temperature over the course of an hour. Such kinetics in thin film allow for *in situ* measurements during crystallization and the establishment of a direct relationship between charge mobility and optoelectronic properties as a function of thin film crystallinity in an important class of semiconducting polymers. Significantly, the correlation of thin film microstructure, as monitored with grazing-incidence X-ray diffraction (GI-XRD) is correlated with optical and charge transport measurements all in real time. We demonstrate that while the degree of crystallinity and optical properties of the material exhibit a continuous increase over time, there is a critical point at which a significant increase polymer field-effect hole mobility is observed. This model polythiophene derivative, P3EHT, with an accessible melting temperature and crystallization kinetics, provides new insight into the relationship between crystallinity and properties in semiconducting polymers and suggests new considerations important to the design of polymeric devices. In particular, this indicates that while the total fraction of polymer crystallinity is critical in controlling optical properties, a threshold effect is in place for charge mobility properties. Furthermore, it can be seen that the hole mobility in P3EHT thin films are dependent on the morphology at the crystalline length scale and those on the order of device dimensions.

3.1 Introduction

Conjugated polymers, with inherently rigid molecular backbones, have attracted much attention due to their relatively favorable charge transport properties, high optical absorption coefficients, and ease of processing from common organic solvents.[1-3] However, these materials form a semicrystalline film upon solution-casting that is far removed from the equilibrium microstructure; therefore, the processing history of the active layer in an electronic device greatly influences the morphology, which in turn affects performance.[4-8] The degree of crystallinity is a particularly crucial factor in obtaining high performance organic thin film devices.[9-11] Usually in thin film polymeric semiconductors, the charge mobility in the amorphous regions is significantly lower than that in the crystalline domains.[12-15] As such, studying the degree of crystallinity in semiconducting polymer thin films and developing polymers and processing conditions that control the fraction of amorphous polymer is of great interest. In general, previous experimental studies have varied the degree of crystallinity in semiconducting polymer thin films by varying deposition conditions, solvent vapor pressures, solid-state processing, and post-processing conditions (*e.g.*, annealing treatments) to kinetically trap films at various points during crystallization.[12,16-19] However, these methods allow only limited control, making it difficult to form completely amorphous films or to dictate crystalline fraction in order to generate a series of specimens with a *continuum* in the polymer percent crystallinity. Furthermore, non-ideal film-to-film reproducibility hinders an easy interpretation of these experiments. As a result, determining how semicrystalline polymer films crystallize and the effect of this sequence on observable optoelectronic properties has proven extremely difficult. Because this fundamental understanding is lacking, the synthesis of each new polymer requires the reformulation of a new set of processing conditions in order to maximize device performance.[20] Therefore, the practical limits of these materials are unknown, and optimization of polymer-based electronics is largely Edisonian and significantly time intensive.

Poly(3-alkylthiophenes) (P3ATs), in particular, have risen to the fore of the organic electronics community over the past 15 years due to their useful optical and electronic properties.[21-24] In fact, poly(3-hexylthiophene) (P3HT) has become the standard p-type material in polymer-based organic field-effect transistors (OFETs)[25-26] and the standard electron-donating material in bulk heterojunction organic photovoltaic (OPV) devices.[18,27-28] Usually these active layers are deposited from solution at room temperature, which is significantly removed from the crystallization temperature of P3HT (T_c ~180 °C).[29-30] This large degree of undercooling leads to kinetically-trapped microstructures and the morphology is difficult to control.[31-33] On the other hand, we have shown recently that poly(3-(2-ethylhexyl)thiophene) (P3EHT) has comparable optoelectronic properties to that of P3HT and poly(3-dodecylthiophene) (P3DDT), and that its melting and liquid crystal transition temperatures are much lower ($T < 120$ °C).[34] This makes P3EHT an ideal candidate for understanding the impact of crystallization on optoelectronic properties for a technologically important class of semiconductors polymers, poly(3-alkylthiophenes), especially as solid-state processing of organic electronic materials is rising to the fore.[35-36]

Here, we correlate the physics of semicrystalline ordering of a P3EHT (M_n ~10.8 kg/mol, PDI ~1.2) thin film to the polymer's optoelectronic properties utilizing *in situ* measurements on an experimentally convenient time scale when quenching from the melt to room temperature. Specifically, we demonstrate that while the polymer crystallinity continually increases over time, the field-effect transistor (FET) hole mobilities abruptly increase 60-fold at a threshold time. We attribute this mobility onset to the formation of a thin film crystalline network in an amorphous matrix. In addition, we show that the evolution of ultraviolet-visible (UV-Vis) absorption and photoluminescence (PL) profiles in the thin film correlate well with the polymer crystallization. The polymer solidification process is readily observed as the crystal structure of the P3EHT thin film is monitored as a function of time after quenching to room temperature (from the melted ($T_m \approx 80$ °C) state) with grazing-incidence X-ray diffraction (GI-XRD). The appearance of higher order reflections in the GI-XRD spectra with time after quenching indicates three-dimensional crystallization occurring over the course of ~1 h. These real-time observations of crucial structure-transport relationships of this model macromolecular semiconductor provide insight into how polythiophene ordering influences hole transport and optical absorption, which in turn, should lead to: design rules for semiconducting polymer architectures, the opportunity for solid-state processing of semiconducting polymer thin films, and better control of the final active layer microstructures in polymer-based organic electronics.

3.2 Experimental

3.2.1 General Methods

Poly(3-hexylthiophene) (P3HT) and poly(3-(2-ethylhexyl)thiophene) (P3EHT) were synthesized using the Grignard Metathesis (GRIM) polymerization scheme.[37-38] The ^{1}H NMR spectra were measured on a Bruker AVQ-400 spectrometer using deuterated chloroform (Cambridge) solutions containing ~1 wt% polymer. The molecular weights of the polymers were calculated using end group analysis of the ^{1}H NMR spectrum. Size exclusion chromatography (SEC) data were collected on either a Viscotek TDA 302 SEC with a set of four Viscotek T-columns (one of each of T6000, T5000, T4000, and T3000 columns) and a refractive index detector. THF at 35 °C was used as the mobile phase at a flow rate of 1 mL min^{-1}. The instrument was calibrated with polystyrene (PS) standards (Polymer Laboratories). The polydispersity index (PDI) of the polythiophenes was calculated using SEC against polystyrene standards. Film thicknesses were estimated by scratching the polymer film and measuring the step change with a Veeco Dektak 150 profilometer.

3.2.2 Structural and Optoeletronic Characterization

Thin Film Grazing Incidence X-Ray Diffraction (GI-XRD) Structural Characterization. Grazing incidence X-ray diffraction data were collected with a two-dimensional MAR345 image plate detector at SSRL beam line 11-3. The incidence angle was optimized to increase scattering from the film and minimize substrate scattering. Beam line 11-3 operates at an energy of 12.7 keV and a sample to detector distance of approximately 400 nm (calibrated with a LaB_6 standard) was used. Data were corrected for the nonlinear mapping between pixel position and q before analysis. The pole figures were formed by computing cake integrations along an arc of constant q corresponding to the position of the (100) peak (~4.5 nm^{-1}) from β of –90° to +90° (with β defined such that 0° corresponds to the area detector meridian (vertical), and 90° corresponds to in-plane), using a Δq wide enough to encompass the entire peak. Appropriate background subtractions were made to remove the parasitic and other background scattering. We note that there exists a distortion from the true specular condition with increasing q_z for a flat image plate detector in the grazing incidence geometry.[39] However, in this case (*e.g.*, the (100) reflection), the q position is low enough that the distortion is small. This was confirmed by the identical shape of local specular curves of the (100) peak, taken with the two-dimensional detector and the incident angle at the scattering angle for the (100) Bragg reflection.[39] Furthermore, high resolution rocking curve data collected for polar angles within a few degrees of zero[40] overlapped with the 2D-GIXS intensity. This shows that the approximate pole figures from the GIXD geometry are sufficiently accurate for our purposes. Therefore, partial pole figures, consisting of data extracted from only the two-dimensional grazing incidence diffraction patterns were used for texture and relative degree of crystallinity calculations, easing data collection. The small distortion associated with partial pole figures, compared to complete pole figures, which combine both grazing incidence data and specular data, may result in a small error in relative degree of crystallinity calculation. For P3HT films of similar thickness, with a population of crystallites perfectly aligned with the substrate, the error can be quite large (up to 20%). However, for the case of the P3EHT films in this study, the overlapping specular data, and lack of perfectly oriented crystallites, confirms the low error associated with partial pole figures, and the validity of the presented data. Because the films are isotropic in the plane of the substrate, the (100) pole figures are completely captured in the intensity vs. β plots rather than two-dimensional stereograms. However, we do take into account the integration across spherical coordinates when calculating the relative degree of crystallinity.

Ultraviolet-Visible (UV-Vis) Absorbance and Photoluminescence (PL) Measurements. UV-Vis measurements were made with Varian Cary 50 instrument between 350 and 900 nm. Photoluminescence measurements were made with Varian Cary Eclipse Fluorescence Spectrophotometer between 500 and 900 nm with excitation at 452 nm. Thin films were fabricated by spinning solution of 10 mg polymer per 1 mL chloroform at 2000 rpm for 60 sec on glass substrates. Final film thicknesses were measured to be ~60 nm. Films were heated to 120 °C under vacuum for 30 min, quenched to room temperature (t = 0 min) and transferred to the instrument within 30 sec. UV-Vis and PL measurements were performed every ten minutes at room temperature.

Field-Effect Transistor (FET) Fabrication and Measurements. Heavily doped silicon with a 200 nm thermally grown dielectric SiO_2 layer (C_i = 17.3 nF cm^{-2}) was used as the substrate and gate electrode for the fabrication of bottom-gate, bottom-contact field-effect transistors (FETs). The substrates were cleaned by sonication for 10 min in acetone, hexanes, and isopropanol sequentially. The substrates were then blown dry with compressed nitrogen. The gold-patterned substrates then were transferred into an inert atmosphere glove box. The gold bottom contacts were patterned with photolithography to yield a channel with dimensions of L = 5 μm and W = 2000 μm. To generate the active layer, a 10 mg P3EHT per 1 mL anhydrous chloroform solution was deposited onto the silicon substrate and spun-coat at a rate of 2000 rpm for 1 min. The film was then allowed to dry for 1h at room temperature in the glove box. The film was then heated to 120 °C for 30 min and quenched to room temperature (t = 0 min). After transferring the devices to a Desert Cryogenics vacuum probe station, the chamber was evacuated using a turbomolecular pump (P ~10^{-6} Torr). Current-voltage characteristics were measured using an Agilent HP 4156C Precision semiconductor parameter analyzer connected to Model 72A-24/10 probe tips (American Probe and Technologies). Data were collected and stored using LabView source code. All measurements were acquired in the dark. Mobility values were determined in the saturation regime (V_D = –60 V) and calculated using the following equation.[41]

$$\frac{\partial[(I_{D,sat})^{1/2}]}{\partial V_G} = \sqrt{\frac{W}{2L}\mu C_i} \qquad (3.1)$$

3.3 Results and Discussion

3.3.1 Structural Characterization of Thin Films

Thin films of P3EHT are crystallographically highly oriented (strong crystalline texture) relative to other P3ATs, as evidenced by greater resolution of reflections in grazing-incidence X-ray diffraction (GI-XRD) patterns (Figure 3.1) and pole figures (Figure 3.2). This allows for determination of a potential unit cell for P3EHT which is qualitatively different from that of the orthorhombic cell proposed for other P3ATs.[42-43] From the GI-XRD pattern of P3EHT (Figure 3.1i), the (100), (200), and (300) reflections are observed along the vertical axis at q = 4.38, 8.62,

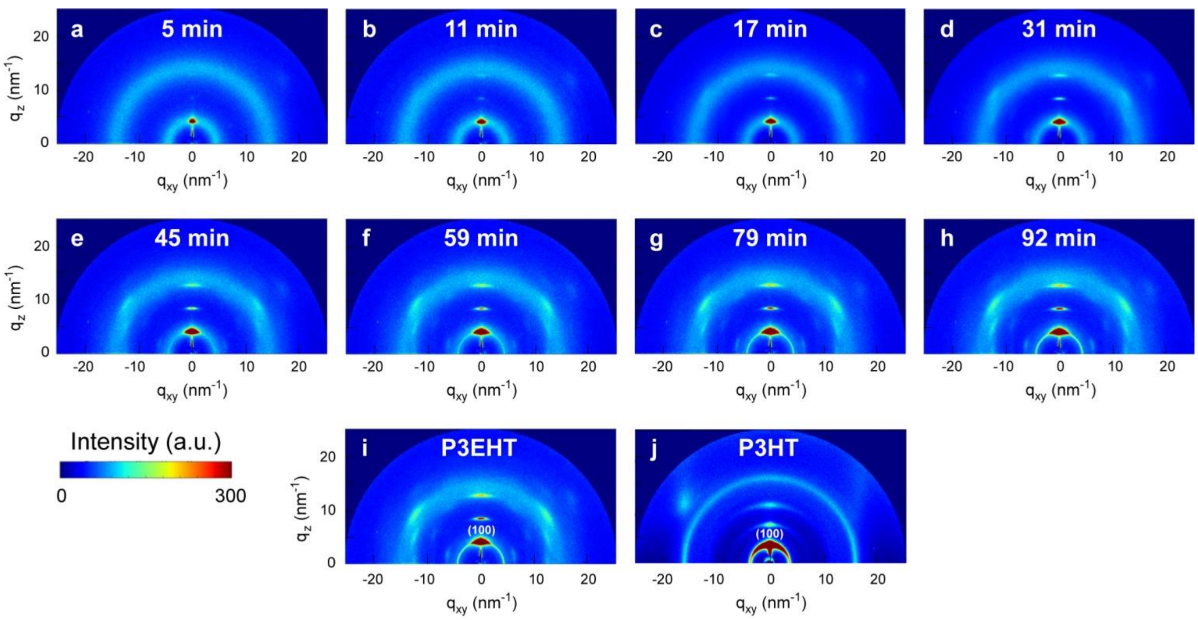

Figure 3.1: Grazing incidence x-ray diffraction patterns of P3EHT thin films

Grazing-incidence X-ray diffraction (GI-XRD) patterns of a P3EHT thin film at (a) 5, (b) 11, (c) 17, (d) 31, I 45, (f) 59, (g) 79, and (h) 92 minutes after quenching to room temperature from the isotropic melt. Comparison of patterns for (i) P3EHT 92 minutes after quenching to room temperature and (j) P3HT with the (100) reflection labeled. The color scale for Figure 3.1j is 0 to 600 a.u. due to a longer exposure time for the P3HT thin film.

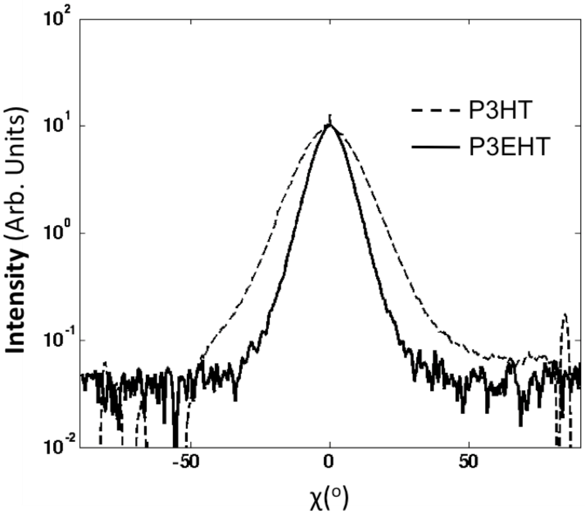

Figure 3.2: Approximate (100) pole figure of P3EHT and complete (100) pole figure of P3HT

Comparison of the approximate (100) pole figure of P3EHT and the complete (100) pole figure of P3HT thin films of similar thicknesses. The narrower pole figure width for the P3EHT pole figure suggests a more oriented crystalline texture in the P3EHT thin film.

and 12.9 nm^{-1}, respectively; this preferential alignment relative to the substrate is seen in the P3HT film as well (Figure 3.1j). However, unlike other P3ATs, the (01*l*) line of reflections is located at q_{xy} = 6.15 nm^{-1} (*e.g.*, the (010) can be seen at q_{xy} = 6.15 nm^{-1} and q_z = 2.0 nm^{-1}). This indicates that P3EHT does not occupy the same orthorhombic unit cell as P3HT. While the complete indexing and molecular packing determination are beyond the scope of this chapter, the position of the (010) reflection leads to lattice parameter of b = 1.03 nm. This is over twice as large as that observed in other P3ATs (*e.g.*, d = 0.39 nm for P3HT[34]), which indicates that there is a second thiophene chain in the unit cell located halfway between along the b-direction and staggered along the chain axis, resulting in a molecule-molecule spacing in this direction of 0.52 nm.

In addition to the improved crystalline texture, the lower thermal transitions of P3EHT relative to other P3ATs allows crystallization to be monitored *in-situ* and correlated to changes in optoelectronic properties, which are also measured as a function of crystallization time. GI-XRD patterns of the P3EHT thin films collected after quenching from the isotropic melt to room temperature reveal the progression of crystallization as a function of time. Shortly after quenching (Figure 3.1a), the diffraction pattern is similar to that of the polymer film in the melt (Figure 3.3) with an amorphous halo the dominating feature. A weak peak exists along the vertical near 4.50 nm^{-1}, corresponding to the expected repeat distance of approximately 1.4 nm along the sample normal (nominally the alkyl stacking direction) according to powder diffraction of bulk P3HT and P3EHT, and is indexed as the (100) Bragg reflection.[34] After ten minutes, two additional orders of (h00) peaks are visible, and the intensity of the (h00) peaks continues to increase with time (labeled in Figure 3.1i). Approximately 31 min after quenching, a number of off-axis peaks appear, including the (010), corresponding to the π-π stacking repeat. With further increasing time, the amorphous halo decreases in intensity, and the (h00), (010), and off-axis peaks become more defined, but without significant increases in intensity.

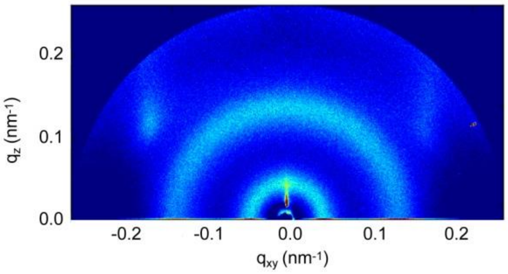

Figure 3.3: Grazing-incidence x-ray diffraction patterns of P3EHT in the melt

GI-XRD spectra of P3EHT in the melt at 120 °C showing no reflections and a wide amorphous halo due to the lack of crystallinity when heated above the melting point.

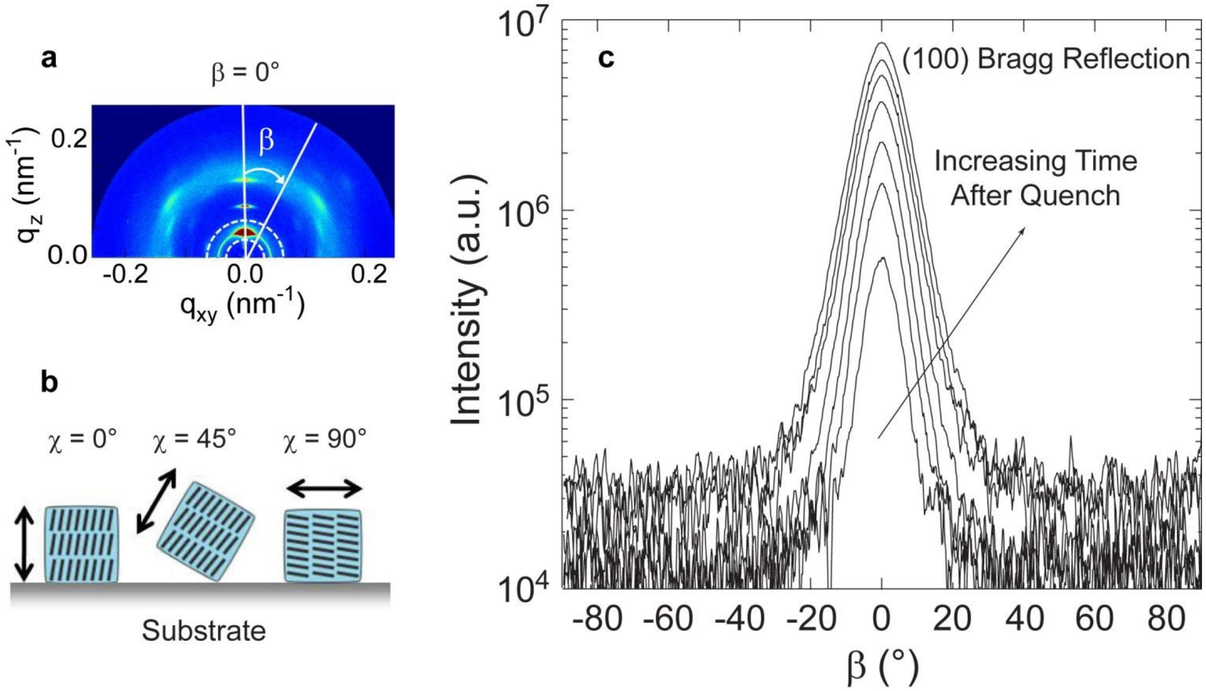

Figure 3.4: Orientation of Crystallites in P3EHT thin films

(a) The two-dimensional GI-XRD pattern demonstrates the definition of the β angle, which ranges from 0° on the vertical to 90 ° on the horizontal. The (100) Bragg reflection (encompassed by the dashed lines) was used to calculate the relative degree of crystallinity (*rDoC*) data shown in Figure 3.5. (b) The cartoon shows the orientation of P3EHT chains relative to the silicon dioxide substrate for various values of the β angle. The arrows of the illustration indicate the orientation of the (h00) vector. (c) Approximate pole figures of the (100) Bragg reflection as a function of time.

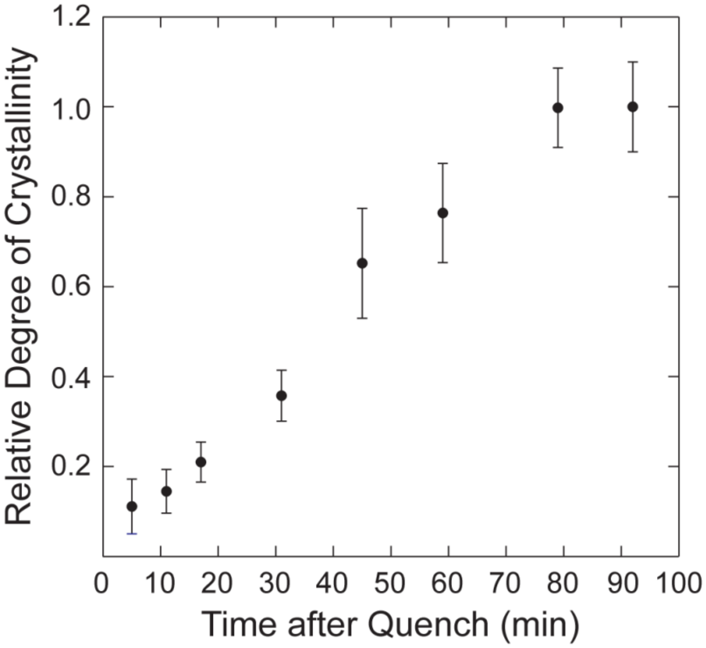

Figure 3.5: Relative degree of crystallinity as a function of time

The relative degree of crystallinity (*rDoC*) as a function of time for the P3EHT thin film, based on intensity of the (100) Bragg reflection. Here, all *rDoC* values are normalized such that the final time (t = 93 min) has a value of 1.0.

3.3.2 Optoelectronic Characterization During Crystallization

A 60-fold increase in the field-effect hole mobility occurred over the course of polymer crystallization after quenching from the melt (vide infra) and can be explained by the crystallization of the P3EHT film. The relative degree of P3EHT crystallinity is determined quantitatively as a function of time by measuring approximate pole figures of the (100) reflection (Figure 3.4).[39] The measured crystallinity steadily increases over ~75 minutes after quenching before reaching a constant value (Figure 3.5). Due to geometry of grazing incidence diffraction, these approximate pole figures (Figure 3.4b) do not probe crystallites with their (100) direction oriented within a few degrees of the substrate normal; this requires local specular scans. However, in our case, the approximate pole figures are quite accurate (see Figure 3.2). The relative degree of crystallinity (*rDoC*) was calculated from the approximate pole figures according to Equation 3.2.

$$DoC \propto \int_{\chi_{\min}}^{\frac{\pi}{2}} \sin(\chi) I(\chi) d\chi \tag{3.2}$$

where χ_{min} is the minimum χ allowed by the GI-XRD geometry. The film with the highest degree of crystallinity in this dataset, corresponding to the longest time after quench, was assigned a value of 1.0, against which other thin films were compared.

In addition to increased intensity of peaks in GI-XRD, thin film UV-Vis absorption and photoluminescence (PL) profiles show a clear red-shift, a signature of increased conjugation length in organic semiconductors, with time after quenching from the melt. When the isotropic melt is quenched directly to room temperature, the absorption profile is initially broad and features only one maximum at λ = 463 nm (Figure 3.6a).[44] This absorbance profile is akin to a dilute solution of a regioregular P3AT in a good solvent[45] and the absorbance profile of a regiorandom P3AT thin film.[46-47] In both of these, the P3AT lacks semicrystalline order and no interchain optoelectronic coupling exists. This comparison shows that the P3EHT film is noncrystalline immediately after quenching to room temperature, consistent with the GI-XRD profile. However, at a *rDoC* value as low as 0.15 (10 minutes after quenching), the profile begins to red-shift and a vibronic shoulder appears at a higher wavelength ($\lambda \approx 573$) indicating the formation of small crystalline regions. As the time after quench approaches 1 h, the P3EHT absorption coefficient increases and reaches a relatively high value in agreement with previous reports.[45,48] This thin film absorption behavior of P3EHT is in stark contrast to that of a P3HT thin film quenched to room temperature from the melt.[49] In the P3HT case, the absorption profile remains constant over the course of one hour (Figure 3.7); this is consistent with rapid crystallization of the straight chain alkyl substituted P3AT at room temperature due to significant undercooling.

Furthermore, the absorption profiles show an isosbestic point is present at λ = 452 nm during the course of crystallization. This indicates that only two species contribute to the overall absorption profile, and that the total absorption profile is a linear combination of each component's absorption spectrum.[50-51] These two absorbing species are taken to be the amorphous domains, where the absorption occurs without interchain coupling, and crystalline domains, in which correlations between neighboring chains increase the P3EHT conjugation length. This increase in conjugation length decreases the band gap and shifts the absorption

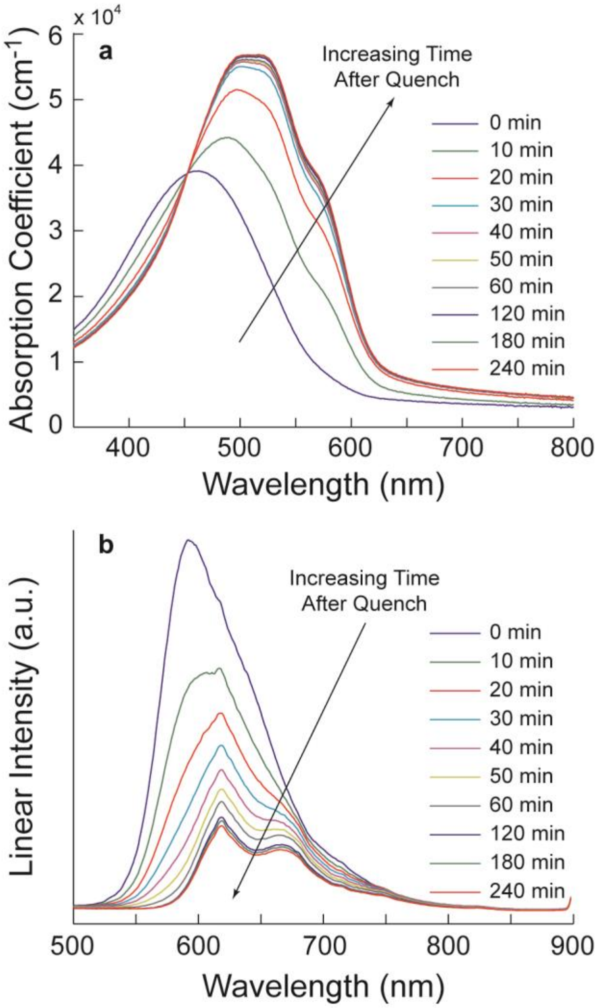

Figure 3.6: Time-resolved optical characterization of P3EHT thin films

(a) Time-resolved thin film UV-Vis light absorption spectra of P3EHT during crystallization. Thin films were heated to the isotropic melt (T = 120 °C) under vacuum and then quenched to room temperature to obtain an amorphous morphology which exhibits an absorption profile similar to that of a dilute P3EHT solution. A red-shift in the absorption profile is observed over the course of crystallization and the presence of a low energy vibronic shoulder is observed also. The isosbestic point at λ = 452 nm is consistent with a non-degradation event that shows the transition from one absorbing species to another. (b) Real-time, steady-state photoluminescence (PL) emission spectra of a P3EHT thin film during crystallization. Thin films were heated to the isotropic melt (T = 120 °C) under vacuum and then quenched to room temperature. A red-shift in the emission profile is observed over the course of crystallization and a secondary, lower energy emission peak emerges. The excitation wavelength was chosen as the isosbestic point to ensure a constant absorption value. Final film thicknesses were ~60 nm as estimated by profilometry.

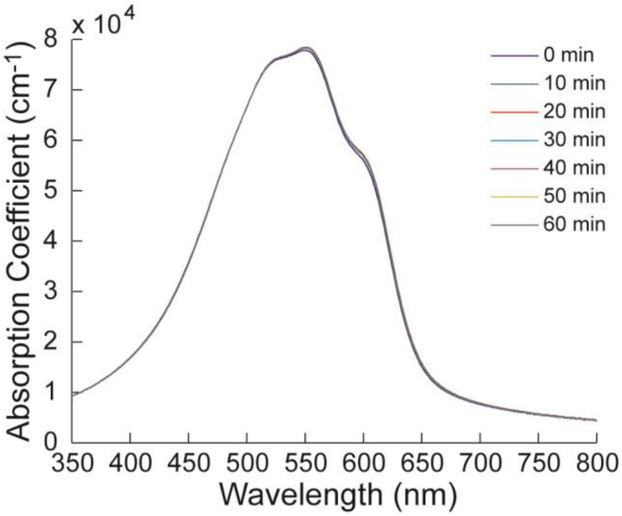

Figure 3.7: Time-resolved UV-vis spectra of P3HT thin films

UV-Vis spectra of poly(3-hexylthiophene) (P3HT) as a function of time after quench from the melt (T = 230 °C) to room temperature. Unlike P3EHT there is little change in the optical properties of this polymer with time, in stark contrast to that of P3EHT shown in Figure 3.6a.

profile of the crystalline domains to longer wavelengths.[25] Thus, the decrease in absorption intensity at shorter wavelengths (λ < 452 nm) and the increase in absorption intensity at longer wavelengths (λ > 452 nm) can be recognized as a signature of the conversion of amorphous to semicrystalline polymer domains with time.

Thin film photoluminescence (PL) data collected in real-time (Figure 3.6b) further demonstrate the formation of interchain P3EHT aggregates over ~1 h after quenching from the isotropic melt. Immediately after quenching, the PL data resemble that of an amorphous P3AT thin film[52] or a dilute P3AT solution with a broad peak at λ < 600 nm.[53-54] As early as 10 min a clear red-shift in the maximum of the emission profile to λ = 617 nm is observed and a small shoulder at lower energy (λ = 665 nm) emerges. This difference of ~0.18 eV commonly is interpreted as the energetic difference associated with the phonon energy of the C=C symmetric stretch of the conjugated backbone.[53] With time, there is an increase in the emission at λ = 665 nm and a decrease in emission at λ = 617 nm. Previous efforts have shown that the lower wavelength peak is associated with amorphous regions of a P3AT film while the higher wavelength peak is representative of emission from a crystalline region of the film.[33] Furthermore, it has been demonstrated that the increase of the lower energy emission peak relative to the higher energy emission is consistent with an increase in polythiophene conjugation length.[47,53] In fact, the decrease in emission at λ = 617 nm has been seen for P3AT thin films with increasing regioregularity.[55] Therefore, we conclude that the semicrystalline order in our films leads to decreased PL emission at λ = 617 nm. Additionally, these PL data and the P3EHT thin film absorption data confirm that the optical properties are intrinsically coupled with the microstructure of the P3AT and that we can observe these structure-property evolutions in real-time.

In contrast to the relatively uniform increase in the *rDoC* and absorption coefficient as a function of time, there is a much sharper increase in the mobility (Figure 3.8). The first measurement made after quenching (t = 12 min) shows a P3EHT hole mobility (μ_h) of μ_h ~6 x 10^{-7} cm^2 V^{-1} s^{-1}, which is low and consistent with an amorphous material with many charge trap sites. This low mobility persists up to *rDoC* ≈ 0.30 (t ≈ 28 min) at which time a dramatic increase (Figure 3.8, shaded region) in hole mobility of ~60 fold, which suggests the formation of a semicrystalline network that is better suited for carrying charge. Note that this is also the point where the π –π stacking reflections and other off axis peaks appear in the GI-XRD spectrum. Finally, the hole mobility saturates at μ_h ~4 x 10^{-5} cm^2 V^{-1} s^{-1} for *rDoC* ≈ 0.5, remains relatively constant over the remainder of the experiment and is of the same order as for low molecular weight P3DDT and P3EHT polymers.[34,56]

Importantly, these data allow for the better understanding of how crystallinity affects charge transport due to the ease of processing associated with P3EHT. For instance, at higher *rDoC* (>0.5) the hole mobility saturates despite a two-fold increase in the relative *rDoC*. Once a series of semicrystalline domains that can be crossed easily are available for charge transport, holes readily move along these high mobility pathways.

In addition to having a much longer crystallization time than straight-chain poly(3-alkythiophenes) at room temperature, the final P3EHT diffraction pattern (achieved after ~90 min, Figure 3.1f) displays more off-axis peaks than a P3HT film (Figure 3.1g) and has more highly oriented crystalline texture. The presence of significant off-axis peaks implies coherent three-dimensional molecular packing, which is the case for well-ordered films of other liquid crystalline polymers such as poly(5,5-*bis*(3-doedecyl-2-thienyl)-2,2-bithiophene) (PQT)[57] or

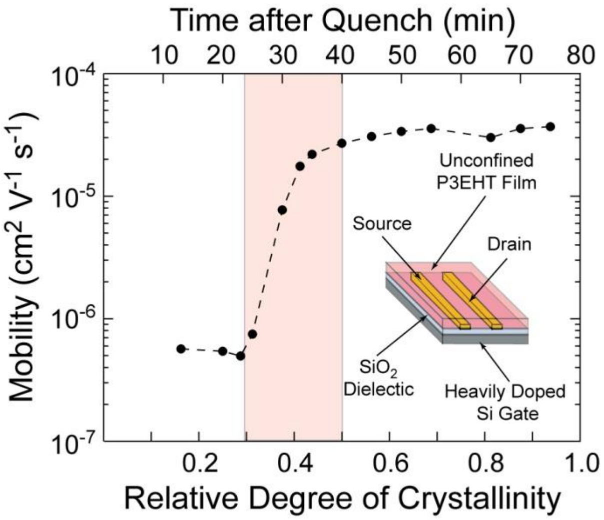

Figure 3.8: Field-effect hole mobility during crystallization

Field-effect hole mobility (μ_h) as a function of the relative degree of crystallinity as determined from the data in Figure 3.5 (the upper axis shows the time after quenching from the melt). The inset schematically depicts the silicon oxide-gated bottom gate, bottom contact field-effect transistor (FET) device geometry. A bottom contact geometry ensures that the polymer is not confined by an electrode interface during microstructural organization. Mobility values were calculated in the saturation regime (V_D = –60 V).

poly(2,5-*bis*(3-alkylthiophen-2-yl)thieno[3,2-*b*]thiophene) (pBTTT).[58] Both of these materials possess a lower density of side chains compared to P3HT, allowing for molecular interdigitation.[59] The side chain complexity in the P3EHT structure may result in a similar interdigitation effect. Furthermore, the broader peak in the pole figure (Figure 3.2) for a P3HT film of comparable thickness indicates significantly more oriented crystalline texture in the P3EHT film. This texture is independent of quenching time, as shown by the similar shapes of the approximate pole figures (Figure 3.4c). The crystallites are well-oriented with the (h00) vector normal to the substrate (Figure 3.4b), which suggests that on average there is smaller spread in out-of-plane orientations between neighboring crystallites. In other systems, polymer films with long-range crystallographic alignment have been used to make high performance field-effect transistors.[9,60] Therefore, P3EHT may prove to be a material whose microstructure can be manipulated easily for the fabrication of high performance organic electronic devices, as well as a useful material for the real-time study of P3AT crystallization and optoelectronic studies.

3.4 Conclusions

Because it has readily accessible melting and liquid crystalline transitions, poly(3-(2-ethylhexyl)thiophene) was used as a model polymer to study the time-resolved crystallization of poly(3-alkylthiophenes), an important class of semiconducting polymers. Due to the slow crystallization of P3EHT when quenched from the melt to room temperature, we observe the formation of a semicrystalline thin film with a strongly preferred crystallographic orientation over the course of ~1 h and we are able to correlate this microstructural ordering in the film directly with changes in the optoelectronic properties of the polymer. Specifically, a P3EHT thin film shows a clear transition in hole mobility that we interpret as due to the formation of a percolating crystalline network; at this point (*rDoC* increasing from 0.3 to 0.5), the hole mobility increases 60 times relative to the amorphous film. Furthermore, the optical properties of the polymers shift from a regime of amorphous-like behavior where there are only intramolecular correlations to that of a crystalline P3AT where intermolecular interactions play crucial roles at the same point that FET hole mobility sharply increases. By utilizing a P3AT that crystallizes on an experimental convenient time scale at room temperature, we can correlate how the degree of crystallinity in P3AT thin films affect the material's optical and electronic properties in real-time. The better understanding of these crucial relationships, in turn, can help guide the design of new semiconducting polymers and the new active layer processing conditions in organic electronic devices.

Acknowledgements. Support provided through the DOE-Office of Science Plastic Electronics Program at Lawrence Berkeley National Laboratories, supported via the Director, Office of Science, Office of Basic Energy Sciences (BES), Division of Materials Sciences and Engineering, of the US Department of Energy (DOE) under contract No. DE-AC02-05CH11231 and the National Science foundation for a graduate fellowship. Device fabrication and characterization was performed at the Molecular Foundry, a Lawrence Berkeley National Laboratory user facility supported by the Office of Science, BES, DOE. Portions of this research were carried out at the Stanford Synchrotron Radiation Lightsource, a Directorate of SLAC National Accelerator Laboratory and an Office of Science User Facility operated for the U.S. Department of Energy Office of Science by Stanford University. Field-effect transistor measurements were performed by Bryan W. Boudouris. GI-XD analysis was performed in collaboration with Leslie H. Jimison, Michael F. Toney, and Alberto Salleo at Stanford University and the Stanford Synchrotron Radiation Laboratory (SSRL). LHJ acknowledges support from Toshiba Corporation through the Center for Integrated Systems at Stanford. AS gratefully acknowledges support from the National Science Foundation in the form of a Career Award. RAS acknowledges support from the Alfred P. Sloan Foundation.

3.5 References and Notes

1. *Handbook of Conducting Polymers*. Skotheim, T. A.; Elsenbaumer, R. L.; Reynolds, J. R., Eds.; Marcel Dekker: New York, 1998; Vol. 2.

2. Loo, Y. L.; McCulloch, I. Progress and challenges in commercialization of organic electronics. *MRS Bull* **2008,** *33* (7), 653.

3. Shaheen, S. E.; Ginley, D. S.; Jabbour, G. E. Organic-based photovoltaics. toward low-cost power generation. *MRS Bull* **2005,** *30* (1), 10.

4. Tsao, H. N.; Mullen, K. Improving polymer transistor performance via morphology control. *Chem Soc Reviews* **2010,** *39* (7), 2372.

5. Inigo, A. R.; Tan, C. H.; Fann, W.; Huang, Y. S.; Perng, G. Y.; Chen, S. A. Non-dispersive Hole Transport in a Soluble Poly(p-phenylene vinylene). *Adv Mater* **2001,** *13* (7), 504.

6. Huang, Y. F.; Inigo, A.; Chang, C. C.; Li, K. C.; Liang, C. F.; Chang, C. W.; Lim, T. S.; Chen, S. H.; White, J.; Jeng, U. S.; Su, A. C.; Huang, Y. S.; Peng, K. Y.; Chen, S. A.; Pai, W. W.; Lin, C. H.; Tameev, A.; Novikov, S.; Vannikov, A.; Fann, W. S. Nanostructure-Dependent Vertical Charge Transport in MEH-PPV Films. *Adv Funct Mater* **2007,** *17* (15), 2902.

7. Salleo, A.; Kline, R. J.; DeLongchamp, D. M.; Chabinyc, M. L. Microstructural Characterization and Charge Transport in Thin Films of Conjugated Polymers. *Adv Mater* **2010,** *22* (34), 3812.

8. Jimison, L. H.; Salleo, A.; Chabinyc, M. L.; Bernstein, D. P.; Toney, M. F. Correlating the microstructure of thin films of poly[5,5-bis(3-dodecyl-2-thienyl)-2,2-bithiophene] with charge transport: Effect of dielectric surface energy and thermal annealing. *Phys Rev B* **2008,** *78* (12), 125319.

9. Mcculloch, I.; Heeney, M.; Bailey, C.; Genevicius, K.; Macdonald, I.; Shkunov, M.; Sparrowe, D.; Tierney, S.; Wagner, R.; Zhang, W. M.; Chabinyc, M. L.; Kline, R. J.; Mcgehee, M. D.; Toney, M. F. Liquid-crystalline semiconducting polymers with high charge-carrier mobility. *Nat Mater* **2006,** *5* (4), 328.

10. Zhang, R.; Li, B.; Iovu, M. C.; Jeffries-EL, M.; Sauve, G.; Cooper, J.; Jia, S. J.; Tristram-Nagle, S.; Smilgies, D. M.; Lambeth, D. N.; McCullough, R. D.; Kowalewski, T. Nanostructure

dependence of field-effect mobility in regioregular poly(3-hexylthiophene) thin film field effect transistors. *J Am Chem Soc* **2006,** *128* (11), 3480.

11. Lunt, R. R.; Benziger, J. B.; Forrest, S. R. Relationship between Crystalline Order and Exciton Diffusion Length in Molecular Organic Semiconductors. *Adv Mater* **2010,** *22* (11), 1233.

12. Yang, H.; Shin, T. J.; Yang, L.; Cho, K.; Ryu, C. Y.; Bao, Z. Effect of Mesoscale Crystalline Structure on the Field-Effect Mobility of Regioregular Poly(3-hexylthiophene) in Thin-Film Transistors. *Adv Funct Mater* **2005,** *15* (4), 671.

13. Masubuchi, S.; Kazama, S. Intrinsic Transport Properties in Electrochemically Prepared Polythiophene Doped with PF6-. *Synthetic Met* **1995,** *74*, 151.

14. Sirringhaus, H.; Brown, P. J.; Friend, R. H.; Nielsen, M. M.; Bechgaard, K.; Langeveld-Voss, B. M. W.; Spiering, A. J. H.; Janssen, R. A. J.; Meijer, E. W.; Herwig, P.; de Leeuw, D. M. Two-dimensional charge transport in self-organized, high-mobility conjugated polymers. *Nature* **1999,** *401*, 685.

15. Sirringhaus, H.; Brown, P. J.; Friend, R. H.; Nielsen, M. M.; Bechgaard, K.; Langeveld-Voss, B. M. W.; Spiering, A. J. H.; Janssen, R. A. J.; Meijer, E. W. Microstructure-Mobility Correlation in Self-Organised, Conjugated Polymer Field-Effect Transistors. *Synthetic Met* **2000,** *111*, 129.

16. Erb, T.; Zhokhavets, U.; Gobsch, G.; Raleva, S.; Stuhn, B.; Schilinsky, P.; Waldauf, C.; Brabec, C. J. Correlation between structural and optical properties of composite polymer/fullerene films for organic solar cells. *Adv Funct Mater* **2005,** *15* (7), 1193.

17. Clarke, T. M.; Ballantyne, A. M.; Nelson, J.; Bradley, D. D. C.; Durrant, J. R. Free Energy Control of Charge Photogeneration in Polythiophene/Fullerene Solar Cells: The Influence of Thermal Annealing on P3HT/PCBM Blends. *Adv Funct Mater* **2008,** *18* (24), 4029.

18. Li, G.; Shrotriya, V.; Huang, J. S.; Yao, Y.; Moriarty, T.; Emery, K.; Yang, Y. High-efficiency solution processable polymer photovoltaic cells by self-organization of polymer blends. *Nat Mater* **2005,** *4* (11), 864.

19. Chang, J.-F.; Sun, B.; Breiby, D. W.; Nielsen, M. M.; SÃ¶lling, T. I.; Giles, M.; McCulloch, I.; Sirringhaus, H. Enhanced Mobility of Poly(3-hexylthiophene) Transistors by Spin-Coating from High-Boiling-Point Solvents. *Chem Mater* **2004,** *16* (23), 4772.

20. Chabinyc, M. L.; Jimison, L. H.; Rivnay, J.; Salleo, A. Connecting electrical and molecular properties of semiconducting polymers for thin-film transistors. *MRS Bull* **2008,** *33* (7), 683.

21. McCullough, R. D. The Chemistry of Conducting Polythiophenes. *Adv Mater* **1998,** *10* (2), 93.

22. Osaka, I.; McCullough, R. D. Advances in Molecular Design and Synthesis of Regioregular Polythiophenes. *Accounts Chem Res* **2008,** *41* (9), 1202.

23. Thompson, B. C.; Frechet, J. M. J. Organic photovoltaics - Polymer-fullerene composite solar cells. *Angew Chem Int Edit* **2008,** *47* (1), 58.

24. Peet, J.; Heeger, A. J.; Bazan, G. C. "Plastic" Solar Cells: Self-Assembly of Bulk Heterojunction Nanomaterials by Spontaneous Phase Separation. *Accounts Chem Res* **2009,** *42* (11), 1700.

25. Sirringhaus, H.; Brown, P. J.; Friend, R. H.; Nielsen, M. M.; Bechgaard, K.; Langeveld-Voss, B. M. W.; Spiering, A. J. H.; Janssen, R. A. J.; Meijer, E. W.; Herwig, P.; de Leeuw, D. M. Two-dimensional charge transport in self-organized, high-mobility conjugated polymers. *Nature* **1999,** *401* (6754), 685.

26. Wang, G. M.; Swensen, J.; Moses, D.; Heeger, A. J. Increased mobility from regioregular poly(3-hexylthiophene) field-effect transistors. *J Appl Phys* **2003,** *93* (10), 6137.

27. Padinger, F.; Rittberger, R. S.; Sariciftci, N. S. Effects of postproduction treatment on plastic solar cells. *Adv Funct Mater* **2003,** *13* (1), 85.

28. Ma, W. L.; Yang, C. Y.; Gong, X.; Lee, K.; Heeger, A. J. Thermally stable, efficient polymer solar cells with nanoscale control of the interpenetrating network morphology. *Adv Funct Mater* **2005,** *15* (10), 1617.

29. Kuila, B. K.; Nandi, A. K. Structural hierarchy in melt-processed poly(3-hexyl thiophene)-montmorillonite clay nanocomposites: Novel physical, mechanical, optical, and conductivity properties. *J Phys Chem B* **2006,** *110* (4), 1621.

30. Verploegen, E.; Mondal, R.; Bettinger, C. J.; Sok, S.; Toney, M. F.; Bao, Z. A. Effects of Thermal Annealing Upon the Morphology of Polymer-Fullerene Blends. *Adv Funct Mater* **2010,** *20* (20), 3519.

31. Jimison, L. H.; Toney, M. F.; McCulloch, I.; Heeney, M.; Salleo, A. Charge-Transport Anisotropy Due to Grain Boundaries in Directionally Crystallized Thin Films of Regioregular Poly(3-hexylthiophene). *Adv Mater* **2009,** *21* (16), 1568.

32. Kayunkid, N.; Uttiya, S.; Brinkmann, M. Structural Model of Regioregular Poly(3-hexylthiophene) Obtained by Electron Diffraction Analysis. *Macromolecules* **2010,** *43* (11), 4961.

33. Brinkmann, M.; Chandezon, F.; Pansu, R. B.; Julien-Rabant, C. Epitaxial Growth of Highly Oriented Fibers of Semiconducting Polymers with a Shish-Kebab-Like Superstructure. *Adv Funct Mater* **2009,** *19* (17), 2759.

34. Ho, V.; Boudouris, B. W.; Segalman, R. A. Tuning Polythiophene Crystallization through Systematic Side Chain Functionalization. *Macromolecules* **2010,** *43* (19), 7895.

35. Baklar, M. A.; Koch, F.; Kumar, A.; Domingo, E. B.; Campoy-Quiles, M.; Feldman, K.; Yu, L. Y.; Wobkenberg, P.; Ball, J.; Wilson, R. M.; McCulloch, I.; Kreouzis, T.; Heeney, M.; Anthopoulos, T.; Smith, P.; Stingelin, N. Solid-State Processing of Organic Semiconductors. *Adv Mater* **2010,** *22* (35), 3942.

36. Muller, C.; Zhigadlo, N. D.; Kumar, A.; Baklar, M. A.; Karpinski, J.; Smith, P.; Kreouzis, T.; Stingelin, N. Enhanced Charge-Carrier Mobility in High-Pressure-Crystallized Poly(3-hexylthiophene). *Macromolecules* **2011,** *44* (6), 1221.

37. Loewe, R. S.; Khersonsky, S. M.; McCullough, R. D. A simple method to prepare head-to-tail coupled, regioregular poly(3-alkylthiophenes) using grignard metathesis. *Adv Mater* **1999,** *11* (3), 250.

38. Loewe, R. S.; Ewbank, P. C.; Liu, J.; Zhai, L.; McCullough, R. D. Regioregular, Head-to-Tail Coupled Poly(3-alkylthiophenes) Made Easy by the GRIM Method: Investigation of the Reaction and the Origin of Regioselectivity. *Macromolecules* **2001,** *34* (13), 4324.

39. Baker, J. L.; Jimison, L. H.; Mannsfeld, S.; Volkman, S.; Yin, S.; Subramanian, V.; Salleo, A.; Alivisatos, A. P.; Toney, M. F. Quantification of Thin Film Crystallographic Orientation Using X-ray Diffraction with an Area Detector. *Langmuir* **2010,** *26* (11), 9146.

40. Jimison, L. H.; Stanford University: Doctoral Thesis, 2010.

41. Sze, S. M.; Ng, K. K., *Physics of semiconductor devices*, 3rd ed.; Wiley-Interscience: Hoboken, N.J., 2007; p x.

42. Prosa, T. J.; Winokur, M. J.; Moulton, J.; Smith, P.; Heeger, A. J. X-ray Structural Studies of Poly(3-alkylthiophenes): An Example of an Inverse Comb. *Macromolecules* **1992,** *25*, 4364.

43. Brinkmann, M.; Wittmann, J.-C. Orientation of Regioregular Poly(3-hexylthiophene) by Directional Solidification: A Simple Method to Reveal the Semicrystalline Structure of a Conjugated Polymer. *Adv Mater* **2006,** *18* (7), 860.

44. Note that the sample is annealed in a vacuum oven at T = 120 C for at least 30 min, which ensures the removal of any residual solvent from the spin-coating procedure used to generate the thin film.

45. Boudouris, B. W.; Molins, F.; Blank, D. A.; Frisbie, C. D.; Hillmyer, M. A. Synthesis, Optical Properties, and Microstructure of a Fullerene-Terminated Poly(3-hexylthiophene). *Macromolecules* **2009,** *42* (12), 4118.

46. Chen, T. A.; Wu, X. M.; Rieke, R. D. Regiocontrolled Synthesis of Poly(3-Alkylthiophenes) Mediated by Rieke Zinc - Their Characterization and Solid-State Properties. *J Am Chem Soc* **1995,** *117* (1), 233.

47. Brown, P. J.; Thomas, D. S.; Kohler, A.; Wilson, J. S.; Kim, J. S.; Ramsdale, C. M.; Sirringhaus, H.; Friend, R. H. Effect of interchain interactions on the absorption and emission of poly(3-hexylthiophene). *Phys Rev B* **2003,** *67* (6).

48. Thompson, B. C.; Kim, B. J.; Kavulak, D. F.; Sivula, K.; Mauldin, C.; Frechet, J. M. J. Influence of alkyl substitution pattern in thiophene copolymers on composite fullerene solar cell performance. *Macromolecules* **2007,** *40* (21), 7425.

49. P3HT films were quenched from 230 C to room temperature. Because of P3HT's high melting transition, the isotropic phase could not be accessed prior to degradation.

50. Kankare, J.; Lukkari, J.; Pajunen, T.; Ahonen, J.; Visy, C. Evolutionary Spectral Factor-Analysis of Doping Undoping Processes of Thin Conductive Polymer-Films. *Journal of Electroanalytical Chemistry* **1990,** *294* (1-2), 59.

51. Vinokurov, I. A.; Kankare, J. Beer's law and the isosbestic points in the absorption spectra of conductive polymers. *J Phys Chem B* **1998,** *102* (7), 1136.

52. Ruseckas, A.; Namdas, E. B.; Ganguly, T.; Theander, M.; Svensson, M.; Andersson, M. R.; Inganas, O.; Sundstrom, V. Intra- and interchain luminescence in amorphous and semicrystalline films of phenyl-substituted polythiophene. *J Phys Chem B* **2001,** *105* (32), 7624.

53. Clark, J.; Silva, C.; Friend, R. H.; Spano, F. C. Role of intermolecular coupling in the photophysics of disordered organic semiconductors: Aggregate emission in regioregular polythiophene. *Physical Review Letters* **2007,** *98* (20).

54. Cook, S.; Furube, A.; Katoh, R. Analysis of the excited states of regioregular polythiophene P3HT. *Energy & Environmental Science* **2008,** *1* (2), 294.

55. Bai, X.; Holdcroft, S. Molecular Control of Luminescence from Poly(3-Hexylthiophenes). *Macromolecules* **1993,** *26* (17), 4457.

56. Kline, R. J.; McGehee, M. D.; Kadnikova, E. N.; Liu, J.; Frechet, J. M. J.; Toney, M. F. Dependence of Regioregular Poly(3-hexylthiophene) Film Morphology and Field-Effect Mobility on Molecular Weight. *Macromolecules* **2005,** *38,* 3312.

57. Jimison, L. H.; Salleo, A.; Chabinyc, M. L.; Bernstein, D. P.; Toney, M. F. Correlating the microstructure of thin films of poly[5,5-bis(3-dodecyl-2-thienyl)-2,2-bithiophene] with charge transport: Effect of dielectric surface energy and thermal annealing. *Physical Review B* **2008,** *78* (12).

58. Chabinyc, M. L.; Toney, M. F.; Kline, R. J.; McCulloch, I.; Heeney, M. X-ray scattering study of thin films of poly(2,5-bis(3-alkylthiophen-2-yl)thieno[3,2-b]thiophene). *Journal of the American Chemical Society* **2007,** *129* (11), 3226.

59. Kline, R. J.; DeLongchamp, D. M.; Fischer, D. A.; Lin, E. K.; Richter, L. J.; Chabinyc, M. L.; Toney, M. F.; Heeney, M.; McCulloch, I. Critical role of side-chain attachment density on the order and device performance of polythiophenes. *Macromolecules* **2007,** *40* (22), 7960.

60. Hamadani, B. H.; Gundlach, D. J.; McCulloch, I.; Heeney, M. Undoped polythiophene field-effect transistors with mobility of 1 cm(2) V-1 s(-1). *Appl Phys Lett* **2007,** *91* (24).

Chapter 4: Poly(3-alkylthiophene) Diblock Copolymers with Ordered Microstructures and Continuous Semiconducting Pathways

Adapted from "Poly(3-alkylthiophene) Diblock Copolymers with Ordered Microstructures and Continuous Semiconducting Pathways," V. Ho, B.W. Boudouris, B.L. McCulloch, C.G. Shuttle, M. Burkhardt, M.L. Chabinyc, R.A. Segalman, *J. Am. Chem. Soc.*, 2011, 133 (24), 9270-9273. (DOI: 10.1021/ja2035317) *Reproduced by permission of The American Chemical Society*

Conjugated rod-coil and semiflexible-flexible coil diblock copolymers self-assemble due to a balance of liquid crystalline (rod-rod) and monomeric enthalpic (rod-coil) interactions. Previous work has shown that while classical block copolymers self-assemble into a wide variety of nanostructures, when liquid crystalline interactions dominate self-assembly in rod-coil block copolymers lamellar structures are preferred. In this chapter, it is demonstrated that other, potentially more useful, nanostructures can be formed when these two interactions are more closely balanced. In particular, hexagonally-packed polylactide (PLA) cylinders embedded in a semiconducting poly(3-alkylthiophene) (P3AT) matrix can be formed. This microstructure is particularly attractive as it provides the opportunity to incorporate additional functionalities into a majority phase nanostructured conjugated polymer, for example in organic photovoltaic (OPV) applications.

Furthermore, crystallization of the thiophene component can proceed from the inhomogeneous melt and be confined by the glassy nature of the PLA matrix. Many previous efforts to generate such phases in polythiophene-based block copolymers have failed due to the rubbery nature and low strength of segregation at the crystallization temperature of P3ATs. Here, we demonstrate that careful design of the P3AT moiety allows for a balance between crystallization and microphase separation arising from control over the location of the crystallization temperature. In addition to hexagonally-packed cylinders, P3AT-PLA block copolymers form nanostructures with long-range order at all block copolymer compositions. Importantly, the conjugated moiety of the P3AT-PLA block copolymers retains the crystalline packing structure and characteristic high time-of-flight (TOF) charge transport of the homopolymer polythiophene (μ_h ~10^{-4} cm^2 V^{-1} s^{-1}) in the confined geometry of the block copolymer domains.

4.1 Introduction

While there is significant interest in using block copolymer self-assembly strategies to achieve nanoscale patterning in conjugated polymers for optoelectronics, and organic photovoltaics[1-4] in particular, the thermodynamics of self-assembly of these materials is more complicated than classical block copolymers due to the rigidity of the conjugated constituent moiety and the necessity of crystallinity to attain high charge mobility. The phase space of model conjugated block copolymers based on poly(phenylene vinylene) derivatives is at least four dimensional relying on the Flory-Huggins interaction parameter (χN), the volume fraction of each rod-like block (φ_{rod}), the Maier-Saupé parameter (μN), and the block length ratio ($\nu = R_{g,coil}/L_{rod}$).[1,5] In addition to these complexities in the melt, while poly(3-hexylthiophene) (P3HT) is widely studied and of specific utility in photovoltaic applications, due its high hole mobility (μ_h ~10^{-2} cm^2 V^{-1} s^{-1} in thin film transistors),[6-8] thermal self-assembly is generally precluded by crystallization of P3HT ($T_m \approx 220$ °C).[9-11] The P3HT moiety crystallizes as long, semiconducting wire-like domains and the coil block is forced into the amorphous domains between the P3HT fibers. The inability to control the orientation and geometry of the semiconducting wires beyond that of the parent P3HT homopolymer has led to limited utility for optoelectronic applications. When specific solvent annealing conditions are used, lamellar and hexagonally-packed microstructures have been observed in P3HT-based block copolymers, but only when the majority component was the insulating moiety and only under specific solvent annealing conditions.[12]

Modifications to the P3HT chemical structure result in the ability to control rod-rod interactions and may be used to control the driving forces in self-assembly of subsequent block copolymers. For example, poly(3-(2-ethylhexyl)thiophene) (P3EHT), has a relatively low melting temperature ($T_m \approx 80$ °C) and rod-rod interactions that are significantly depressed relative to P3HT while retaining optoelectronic properties that are qualitatively similar to P3HT.[13] In this work we demonstrate that poly(3-(2-ethylhexyl)thiophene)-*b*-polylactide (P3EHT-PLA) block copolymers self-assemble in the semicrystalline state into a number of well-ordered microstructures over the entire block copolymer composition window. Importantly, microstructures of hexagonally-packed polylactide cylinders embedded in a continuous semiconducting P3EHT matrix are observed. Furthermore, the melting transition of P3EHT is sufficiently low that self-assembly can be realized with multiple amorphous blocks as well, indicating the utility of the approach which is not limited to chemistries with high strengths of segregation.

4.2 Experimental

4.2.1 General Methods

^{1}H NMR spectra were measured on a Bruker AVQ-400 or AVB-400 spectrometer using deuterated chloroform (Cambridge) solutions containing ~1 wt% polymer. Molecular weights were determined by end group analysis from the ^{1}H NMR spectra. Size exclusion chromatography (SEC) data were collected on a Viscotek TDA 302 SEC with four Viscotek T-columns (one T-6000, T-5000, T-4000, and T-3000 column). The response was measured using a refractive index (RI) detector. Tetrahydrofuran (THF) at 35 °C was used as the mobile phase at a flow rate of 1 mL min^{-1}. The instrument was calibrated with polystyrene (PS) standards (Polymer Laboratories).

4.2.2 Detailed Synthetic Procedure

Materials. All reagents and solvents were used as received from Sigma-Aldrich unless otherwise noted. Degassed tetrahydrofuran (THF) was purified by passage through an activated alumina column (UOP A2 Alumina, 12-32 mesh) and was collected in flame-dried, air-free flask. Toluene was purified by stirring over calcium hydride and then distilling the material under inert atmosphere. D,L-lactide was purified by recrystallization from ethyl acetate followed by drying under reduced pressure and was stored in an inert atmosphere glove box. Bromine-terminated poly(3-(2-ethylhexyl)thiophene) (P3EHT) was synthesized according to the GRIM procedure which is well-established in the literature and was subsequently subjected to end group modification to generate the diblock copolymer macroinitiator.[13-15]

Representative Synthesis of Hydroxyl-terminated Poly(3-(2-ethylhexyl)thiophene) (P3EHT-OH). Bromine-terminated poly(3-(2-ethylhexyl)thiophene) (3.5 g, 0.5 mmol) was added to a 1 L 3-neck flask. The polymer was dissolved in 500 mL of toluene, 50 mL of ethanol, and 50 mL of 2M aqueous Na2CO3. After purging with nitrogen, the solution was heated to 90 °C. To the reaction, 4-hydroxymethylphenylboronic acid (3.75 g, 25 mmol) was added slowly. Then tetrakis(triphenylphosphine) palladium(0) (300 mg, 0.25 mmol) was added to the reaction mixture. The reaction was allowed to proceed overnight at 90°C. The reaction solution was poured into methanol and the product was purified by Soxhlet extraction with methanol, acetone, and chloroform. The chloroform fraction was saved and used as the macroinitiator (P3EHT-OH) for the ring-opening polymerization of D,L-lactide.

Representative Synthesis of Poly(3-(2-ethylhexyl)thiophene)-*b*-Polylactide (P3EHT-PLA) Block Copolymers. Ring-opening polymerizations of lactide from P3AT macroinitiators are known, and a method similar to previous reports was used here for the polymerization of D,L-lactide.[16-17] The details for the example synthesis of P3EHT(0.36)-PLA(13) are as follows. P3EHT-OH (0.30 g, 0.041 mmol) was dissolved in anhydrous toluene (6.4 mL) in an inert atmosphere glovebox. A solution of 1 M triethyl aluminum (AlEt3) in hexanes (41 μL, 0.041 mmol) was also added in order to have equal molar amounts of AlEt3 and P3EHT-OH present. This solution was stirred overnight at room temperature in the glovebox to allow for the macroinitiator formation. The next morning, D,L-lactide (0.92 g, 6.4 mmol) was added. The reaction was sealed, removed from the glovebox, and placed in an oil bath where it was heated at 90°C for 9 h (~41% conversion of D,L-lactide monomer). The reaction was cooled to room temperature, quenched with ~2 M HCl (1 mL, 2 mmol), and precipitated in methanol. After filtering and washing with methanol, the polymer was dissolved in THF and precipitated in petroleum ether to remove any residual P3EHT homopolymer. The solid product was then filtered, collected, and dried under vacuum overnight.

Representative Synthesis of Bromine-terminated Poly(3-(2-ethylhexyl)thiophene) ATRP macroinitiator (P3EHT-ATRP). Atom transfer radical polymerizations (ATRP) of methyl methacrylate and methyl acrylate from P3HT macroinitiators have been presented in the past.[18] ATRP macroinitiators of P3EHT were synthesized from reaction of P3EHT-OH with the 2-bromoisobutyryl bromide. A solution of P3EHT-OH (1.5g, 0.2 mmol) and triethylamine (3.48 mL, 25 mmol) in THF was stirred at 40 °C for 15 minutes. To this solution, 2-bromoisobutyryl bromide (2.8 mL, 23 mmol) was added dropwise and allowed to stir overnight. The reaction was quenched by addition to methanol and the product was collected by vacuum filtration.

Representative Synthesis of Bromine-terminated Poly(3-(2-ethylhexyl)thiophene)-*b*-Poly(methyl methacrylate) (P3EHT-PMMA). P3EHT-ATRP (0.59 g, 0.08 mmol) polymer was dissolved in 3.5 mL toluene and 1.6 mL methyl methacrylate. To this solution, CuBr (3 mg, 0.02 mmol) and N,N,N′,N′,N″-pentamethyldiethylenetriamine (PMDETA, 4.4 μL, 0.02 mmol) were added and the reaction solution was degassed with three freeze-pump-thaw cycles. The reaction was allowed to proceed for 80 minutes at 75 °C. Reaction was cooled to room temperature, quenched by exposure to air, and precipitated in methanol. After filtering and washing with methanol, the polymer was dissolved in THF and precipitated in petroleum ether to remove any residual P3EHT homopolymer. The solid product was then collected by centrifugation and dried under vacuum overnight.

4.2.3 Thermal and Structural Characterization

Differential scanning calorimetry (DSC) measurements were acquired using a Thermal Advantage Q20 calorimeter at a scan rate of 10 °C min^{-1}. An indium standard was used to calibrate the instrument and nitrogen was used as the purge gas. DSC heating traces presented in the Appendix (Figure 4.5). Small and wide angle X-ray scattering (SAXS and WAXS) samples were prepared by pressing a 2 mm thick polymer disc. The samples were then annealed at 150 °C for 48 h under high vacuum and then cooled slowly to room temperature. SAXS and WAXS experiments were conducted at beamline 1-4 of the Stanford Synchrotron Radiation Laboratory (SSRL). Additional SAXS experiments were carried out at the Advanced Light Source (ALS) on Beamline 7.3.3. Bulk transmission electron microscopy (TEM) samples were prepared by solution casting thick (~1 mm) samples onto epoxy resins from toluene solutions. The samples were then annealed at 150°C for 48 h under high vacuum and then cooled slowly to room temperature. The polymer samples were then thinly sliced using a microtome (thickness ~70 nm) and collected on copper TEM grids. The P3EHT moiety of the P3EHT-PLA block copolymer samples was selectively stained by exposing the thinly-sliced samples to RuO4 vapor for ~40 minutes. TEM imaging was performed on a JEOL JEM-2100 microscope at an operating voltage of 200 kV in bright field mode.

4.2.4 Time-of-flight (TOF) Device Measurements

Sandwich-structure, TOF devices were prepared in the following manner. Glass substrates that were coated with indium-doped tin oxide (ITO) were cleaned by sonication in acetone, soap in water, deionized water, and isopropanol for 20 minutes in each solvent. Then, the poly(3-alkylthiophene) homopolymers and block copolymers were dissolved in *ortho*-dichlorobenzene (125 mg ml^{-1}) and stirred overnight at 80 °C. The polymer was deposited onto the ITO substrates by drop casting from solution over the course of ~3 h. The polymer active layers were subsequently thermally annealed overnight at T = 150 °C and then slowly cooled to room temperature prior to top contact deposition. The layer thicknesses were determined to be 4µm using profilometry. A 90 nm thick gold electrode was evaporated under high vacuum (~10^{-7} mbar) to complete the devices.

In this time-of-flight method, a pulse of laser light (λ = 532 nm) is used to generate a thin sheet of charge pairs at the ITO electrode. An applied voltage is applied to the device to transport holes to the Au electrode. Note that care was taken to ensure that, when tested, the devices were far removed from the capacitive charge limit. The charge transit time (t_{tr}) is then easily determined from the resultant photocurrent transient and the mobility (μ_{TOF}) is calculated using Equation 1.

$$\mu_{TOF} = \frac{d^2}{v_{t_{tr}}} \tag{4.1}$$

Here, d is the thickness of film (4 µm) and V is the applied voltage. Due to the dispersive nature of the TOF transients, the transit time is estimated from the intercept of the asymptotes on a double logarithmic plot of current versus time. The hole carrier mobility was determined at the electric field $E = 1.5 \times 10^5$ V m^{-1}.

4.3 Results and Discussion

4.3.1 Synthesis of Poly(3-(2-ethylhexyl)thiophene)-*b*-Polylactide

P3EHT-PLA block copolymers are readily generated using a change-of-mechanism polymerization (CHOMP) scheme that utilizes two controlled polymerization techniques (Figure 4.1a).[19-20] These block copolymers have tunable molecular weights, narrow molecular weight distributions ($M_w/M_n \leq 1.21$), and contain no residual P3EHT homopolymer (Figure 4.1b), which allows for self-assembly into a number of well-ordered microstructures. The Grignard Metathesis (GRIM) route[14-15] is used to polymerize bromine-terminated P3EHT, which is then end-functionalized with a hydroxyl group through a Suzuki coupling reaction to form the P3EHT-OH macroinitiator. Subsequent controlled ring-opening polymerization (ROP) of D,L-lactide using triethylaluminium ($AlEt_3$) completes the synthesis of the P3EHT-PLA block copolymers. PLA is a desirable coil block as it not only is an amorphous material with an easily-accessible glass transition temperature, but also has been shown to be selectively etchable from a P3AT matrix[16-17] suggesting opportunities to backfill the ordered, porous nanostructures with a material of complementary functionality.[21]

Table 4.1: Summary of P3EHT-PLA polymer sample characteristics

Sample[a]	M_n[b] (kg/mol) P3EHT	M_w/M_n[c]	w_{P3EHT}[d]	T_g(°C)[e] PLA	T_m(°C)[e] P3EHT	Structure[g]	d (nm)[h]
P3EHT-OH	7.4	1.06	1.00	--	79	--	--
P3EHT(0.75)-PLA(2)	7.0	1.07	0.75	34	94	HEX	19.0
P3EHT(0.70)-PLA(3)	7.4	1.06	0.70	33	90	HEX	21.1
P3EHT(0.67)-PLA(4)	7.0	1.08	0.67	36	90	HEX	21.4
P3EHT(0.63)-PLA(4)	7.0	1.05	0.63	36	90	HEX	24.9
P3EHT(0.50)-PLA(7)	7.0	1.09	0.50	39	89	LAM	29.0
P3EHT(0.47)-PLA(8)	7.0	1.12	0.47	41	90	LAM	31.3
P3EHT(0.36)-PLA(13)	7.4	1.09	0.36	46	95	LAM	36.1
P3EHT(0.31)-PLA(16)	7.4	1.11	0.31	49	96	LAM	36.8
P3EHT(0.29)-PLA(17)	7.0	1.12	0.29	47	90	LAM	37.1
P3EHT(0.25)-PLA(21)	7.0	1.13	0.25	46	90	LAM	40.2
P3EHT(0.12)-PLA(56)	7.4	1.21	0.12	51	[f]	M	52.1

[a] P3EHT-OH is a homopolymer of the poly(3-(2-ethylhexyl)thiophene)-*b*-polylactide series symbolized by P3EHT(X)-PLA(Y) where the block copolymer is composed of X weight fraction P3EHT and has a PLA block with a number-average molecular weight of Y kg/mol. [b] As determined by ^{1}H NMR spectroscopy. [c] As determined by SEC versus polystyrene standards. [d] $w_{P3EHT} = M_n(\text{P3EHT}) / [M_n(\text{PLA}) + M_n(\text{P3EHT})]$ [e] As determined by DSC at a heating rate of 10 °C min^{-1} under a nitrogen purge. [f] The P3EHT melting temperature for this sample was not prominent enough to be observed in DSC. [g] The morphology (HEX = hexagonally-packed cylinders of PLA in a P3EHT matrix, LAM = lamellae, and M = P3EHT micelles in a PLA matrix) was determined by SAXS experiments at T = 50 °C. [h] The domain spacing (*d*) was determined from the principle reflection (q^*) acquired in SAXS experiments at T = 50 °C.

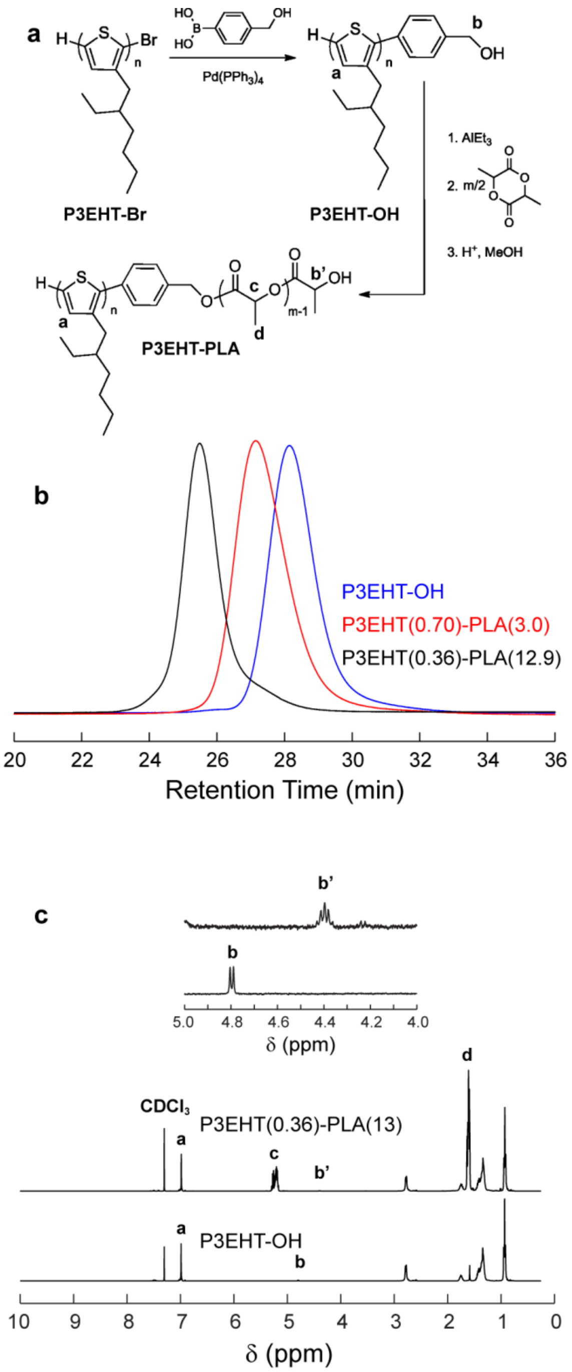

Figure 4.1: Synthetic scheme and characterization of P3EHT-PLA Block Copolymers

(a) Synthetic scheme for P3EHT-PLA using two controlled polymerization techniques. (b) SEC traces of a P3EHT-OH homopolymer and representative block copolymers. The SEC traces were taken with THF at 35 °C as the eluent at a flow rate of 1 mL min^{-1}. (c) Representative ^{1}H NMR for P3EHT-OH and P3EHT-PLA block copolymer. Labeled resonances correspond to protons in (a). Expanded 5.0 to 4.0 ppm regions are provided as insets for comparison.

4.3.2 Self-Assembly of P3EHT-PLA Block Copolymers

At room temperature, block copolymers at all compositions form periodic morphologies commonly observed conventional block copolymer self-assembly (Table 4.1). As with rod-coil block copolymer and semiflexible systems,[1] there exists a large region of compositions ($0.25 \leq w_{P3EHT} \leq 0.50$) for the P3EHT-PLA system where lamellar structures (LAM) are present (Table 4.1) because the lamellar interfaces are generally stabilized by rod-rod interactions.[22-23] The rigidity of the conjugated P3EHT moiety does not allow for the facile generation of microstructures with curved interfaces. Therefore, disordered micelles with spherical shapes (Figure 4.2d) are only observed at extremely high PLA content ($w_{P3EHT} = 0.12$). The long-range order of the lamellae phases is confirmed both through microscopy (Figure 4.2c) and by the integer reflections present in the SAXS spectra (Figure 4.3a).

At high P3EHT content ($0.63 \leq w_{P3EHT} \leq 0.75$), hexagonally-packed cylinders of PLA embedded in a P3EHT matrix (HEX) are observed both in transmission electron microscopy (TEM) images (Figure 4.2b) and small-angle X-ray scattering (SAXS) spectra (Figure 4.3a). The TEM image of the P3EHT(0.70)-PLA(3) block copolymer shows that hexagonally-packed domains form large areas (~1 μm) of mono-orientation with large grains of PLA cylinders (P3EHT is stained dark selectively with RuO_4) running with their long axes parallel and perpendicular to the plane of the TEM image. In fact, a grain boundary is evident in Figure 2b and marked by a white line. This morphology is highly unexpected for systems with conformational asymmetry. In the context of rod-coil block copolymer self-assembly curved interfaces are disfavored and cylindrical domains are not typically observed, even for systems with high coil fractions that adopt hexagonal symmetries.[1,24-25] Furthermore in systems with less conformational asymmetry (*i.e.* semiflexible-flexible), hexagonally packed symmetries are not observed at high volume fractions of the rigid component although spherical and cylindrical morphologies can be observed with large coil compositions.[26] We do not propose an explanation for the observed behavior; however, note that this and the other regularly ordered morphologies (Figure 4.2c) can be observed both at elevated temperatures (above the melting temperature of P3EHT, Figure 4.6) and upon quenching to room temperature where P3EHT is crystalline and PLA is glassy (Table 4.1). As such, these hexagonal morphologies are not the result of crystallization and, due to the lack of order-order transitions upon heating, are somewhat stable thermodynamically. This is in stark contrast to the nanofibril microstructure observed for the P3EHT-OH homopolymer (Figure 4.2a), which has a characteristic fiber width of ~16 nm (measured from SAXS data) and are not observed above the melting temperature of P3EHT.

In addition to forming ordered microstructures at almost all P3EHT weight fractions studied ($0.25 \leq w_{P3EHT} \leq 0.70$), also note that the P3EHT domains remain semicrystalline as evidenced by differential scanning calorimetry (DSC) scans (Figure 4.5) and the powder wide-angle X-ray scattering (WAXS) spectra (Figure 4.3b). Such crystallization of the P3EHT moiety occurs in the nanostructured block copolymer domains and is important for the optoelectronic properties of P3AT moiety. Importantly, representative calorimetry data (Figure 4.5) for block copolymers which self-assemble into all morphologies [P3EHT(0.25)-PLA(21), P3EHT(0.36)-PLA(13), and P3EHT(0.70)-PLA(3) self-assemble into spherical micelles, hexagonally-packed cylinders, and alternating lamellae, respectively] show features indicative of both the glass transition of the PLA and the melting of P3EHT. Glass transition and melting temperatures for all polymer are collected in Table 4.1.

This is of crucial importance when these molecules are used in organic electronic devices as crystallinity is inherently tied to the optoelectronic properties of polymer semiconductors.[27-30]

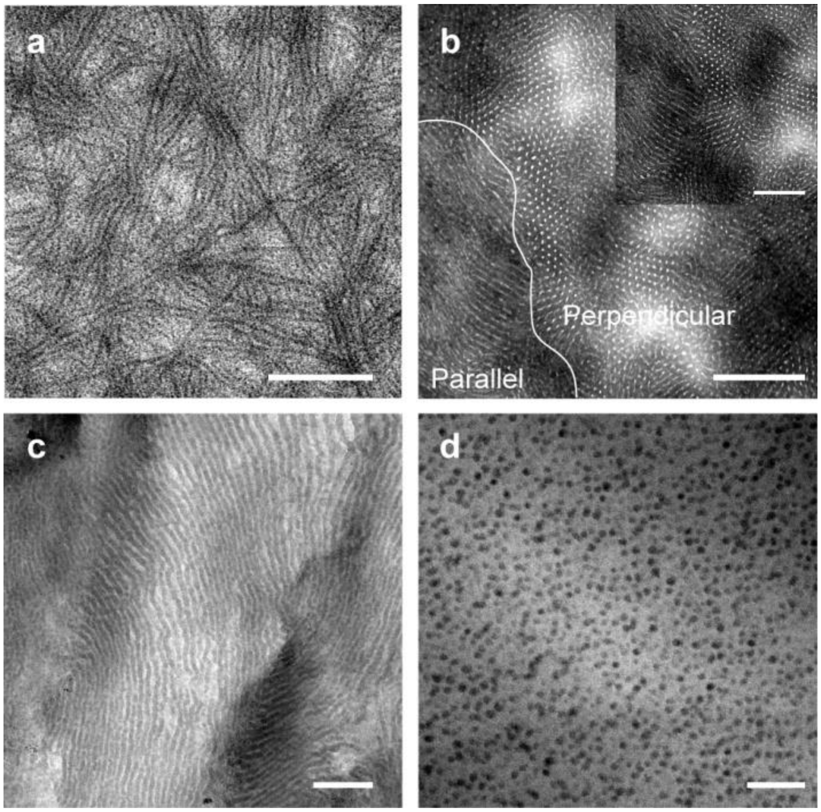

Figure 4.2: Transmission electron micrographs of self-assembled P3EHT-PLA

TEM images of (a) unstained P3EHT-OH nanofibrils (natural contrast occurs due to higher electron density in the crystalline regions) and the stained microstructures of the (b) hexagonally-packed P3EHT(0.70)-PLA(3), (c) lamellar P3EHT(0.50)-PLA(7), and (d) disordered micelles of P3EHT(0.12)-PLA(56). The bulk TEM samples were annealed at 150 °C for 48 h under high vacuum and thinly sliced (~70 nm) using a microtome. Figure 2b highlights two distinct grains. In one, the long axes of the PLA cylinders are parallel to the plane of the image and in the other the long axes of the cylinders are perpendicular to the plane of the image. The inset of Figure 2b is a magnification showing this parallel-to-perpendicular grain boundary. The P3EHT moiety was stained dark in the block copolymer samples by exposing the samples to RuO_4 vapors for 30-50 min. All scale bars represent 200 nm. Further TEM images can be found in the Appendix.

Furthermore, the intensity and breadth of the diffraction peaks changes in the block copolymer. The increased intensity of the (010) reflection is of significance as it suggests an increase in the correlation of π-π interactions, which is directly related to the optical and charge transport properties in organic electronic devices. Finally, we note that for the disordered micelles microstructure, a large amorphous halo associated with the PLA block appears for larger q values ($8 \leq q \leq 18$ nm^{-1}), and the peak width for all reflections is larger than other morphologies and the homopolymer. This is expected as crystallite size is necessarily confined in all dimensions in contrast to a system confined to only one- or two-dimensions (lamellar or cylindrical morphologies, respectively) for which the fast growth crystallite axis can propagate along at least one direction. The ordered HEX and LAM microstructures are present both in the solid state and when heated into the melt, and heating scans show clear endotherms which are significantly increased in block copolymer samples relative to the parent P3EHT homopolymer (Table 4.1). This increased thermal stability of crystalline domains has been observed previously in rod-coil block copolymers and can been attributed to pinning the rod block at the block copolymer interface, which decreases the conformational entropy gained during melting.[31] This confinement also facilitates crystallization of the P3EHT block by providing a common nucleation point for lattice growth, as has been previously observed in PPV-based block copolymers.[32]

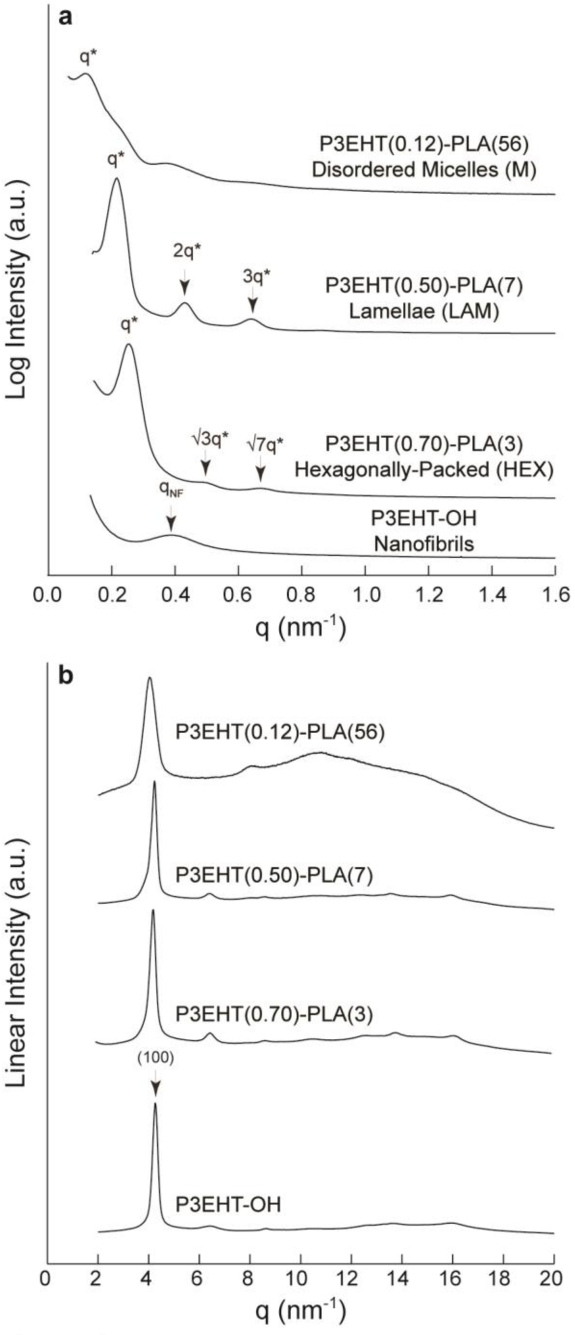

Figure 4.3: Small- and wide-angle x-ray scattering 1-D patterns

(a) Small-angle X-ray scattering (SAXS) and (b) Wide-angle X-ray scattering (WAXS) 1D azimuthally integrated spectra for the P3EHT-OH homopolymer and representative P3EHT-PLA block copolymers for each of the three observed microstructures, hexagonally-packed cylinders (HEX), lamellae (LAM), and micelles (M). The samples were annealed at 150 °C for 48 h under high vacuum prior to data acquisitions. The P3EHT moiety of the block copolymers remains semicrystalline at all block copolymer compositions as evidenced by the alkyl-chain stacking (100) reflections in the WAXS spectra. All spectra shown were acquired at T = 50 °C.

4.3.3 Mobility in Self-Assembled Morphologies

The hole mobility in the P3EHT-PLA block copolymers was measured by time-of-flight (TOF) (Figure 4.4) and values are collected in Table 4.2. Values for block copolymers that self-assemble into percolated morphologies (*i.e.* lamellar and hexagonally-packed cylinders) are comparable to the P3EHT and P3HT homopolymers (M_n(P3HT) ~7 kg/mol) of similar molecular weights (μ_h ~10^{-4} cm^2 V^{-1} s^{-1}), consistent with previous results both in pristine P3AT films and in polymer-fullerene and polymer-polymer blends.[33-35] This is a direct result of the preservation of the P3AT crystal structure within the bock copolymer domains and, importantly, demonstrates the availability of a continuous transport pathway through the co-polymer film. Because of these factors, the mobility for representative hexagonally-packed [P3EHT(0.75)-PLA(2), P3EHT(0.67)-PLA(4)] and lamellar [P3EHT(0.47)-PLA(8)] P3EHT-PLA block copolymers show the same charge transport values with hole mobilities of μ_h ~10^{-4} cm^2 V^{-1} s^{-1}. These data demonstrate that by controlling the rod-rod interactions and crystallization behavior in poly(3-alkythiophene) derivatives well-ordered block copolymer microstructures were generated. Additionally, we are able to control the nanoscale phase separation of the P3EHT domains while retaining the charge transport properties of the most oft-used semiconducting polymer.

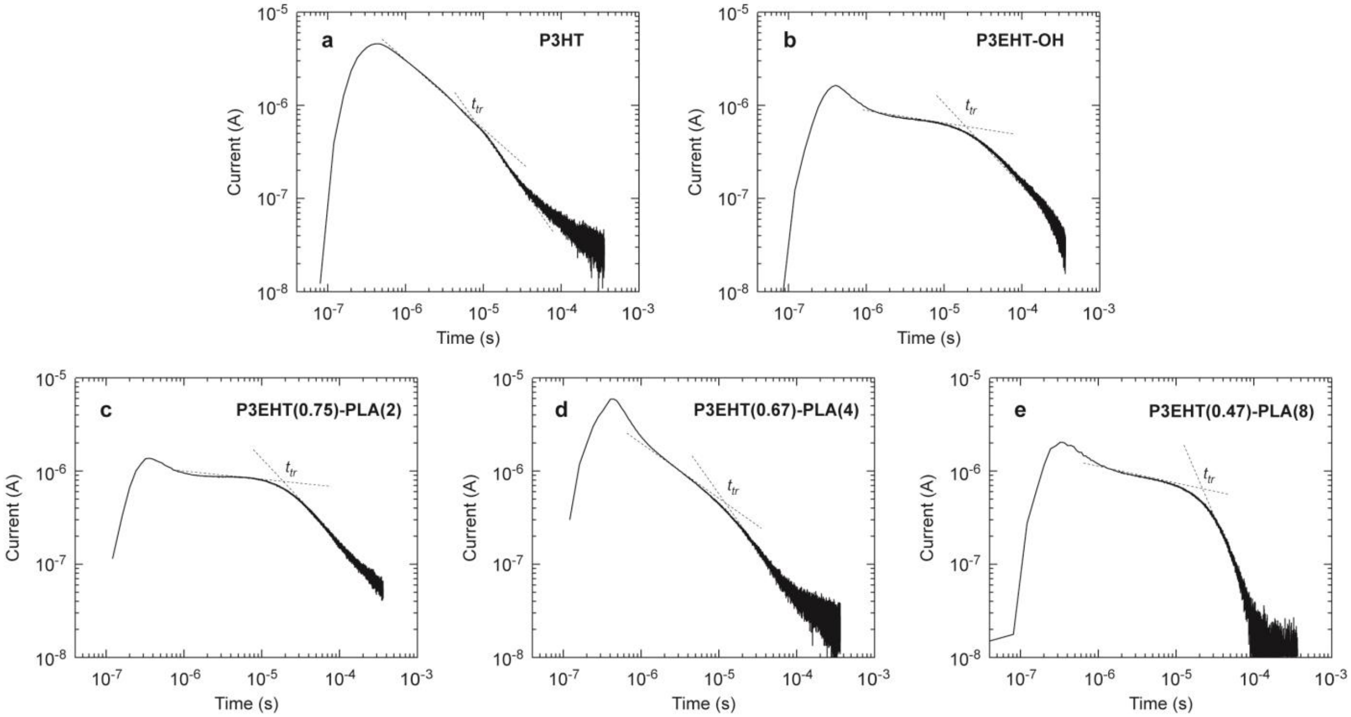

Figure 4.4: Time of flight transients for mobility determination

Raw time-of-flight (TOF) mobility data for the (a) P3HT homopolymer and (b) P3EHT-OH homopolymer samples. Additionally, raw TOF data is shown for representative block copolymers (c) P3EHT(0.75)-PLA(2), (d) P3EHT(0.67)-PLA(4), and I P3EHT(0.47)-PLA(8). The transit time (t_{tr}) used to calculate the TOF mobility values is marked as the intersection of the two dashed lines.

Table 4.2: Summary of time of flight mobility measurements

Sample	Structure	μ_h $(cm^2\ V^{-1}\ s^{-1})^a$
P3HT	--	$3.07\text{x}10^{-4}$
P3EHT-OH	--	$1.23\text{x}10^{-4}$
P3EHT(0.75)-PLA(2)	HEX	$1.83\text{x}10^{-4}$
P3EHT(0.67)-PLA(4)	HEX	$2.21\text{x}10^{-4}$
P3EHT(0.47)-PLA(8)	LAM	$1.47\text{x}10^{-4}$

[a] Mobility measurements extracted from transit times and calculated according to Equation 1.

4.3.4 Self-Assembly in Other P3EHT-containing Block Copolymers

Block copolymers of P3EHT-PLA self-assemble into morphologies conventionally observed in coil-coil block copolymers though large regions of phase space are occupied by lamellar morphologies. Importantly, the ability to confine crystallization relies on the depressed melting transition of P3EHT relative to P3HT, thus opening a larger temperature processing window for obtaining non-crystalline morphologies. This flexibility provides the opportunity to self-assemble a wide range of chemistries as observed in Figure 4.5. Block copolymers with poly(methyl methacrylate) (P3EHT-PMMA) and poly(methyl acrylate) (P3EHT-PMA) self-assemble into lamellar morphologies as evidenced by integer multiples of SAXS peaks. Interestingly, this series of block copolymer indicates that self-assembled morphologies can be obtained in the semicrystalline state for block copolymers that are glassy (PLA and PMMA) or rubbery (PMA, $T_g \sim 10$ °C) at the crystallization temperature of the polythiophene. This is a clear indication that the crystallization can proceed either under hard or soft confinement. Though the comparison in this section is kept qualitative, it indicates that the self-assembly of P3AT-containing block copolymers into periodic nanoscale morphologies can be controlled simply by simple substitution of the alkyl chain on the thiophene component. Self-assembly of P3DDT-PMMA has also been presented based on this premise.[36]

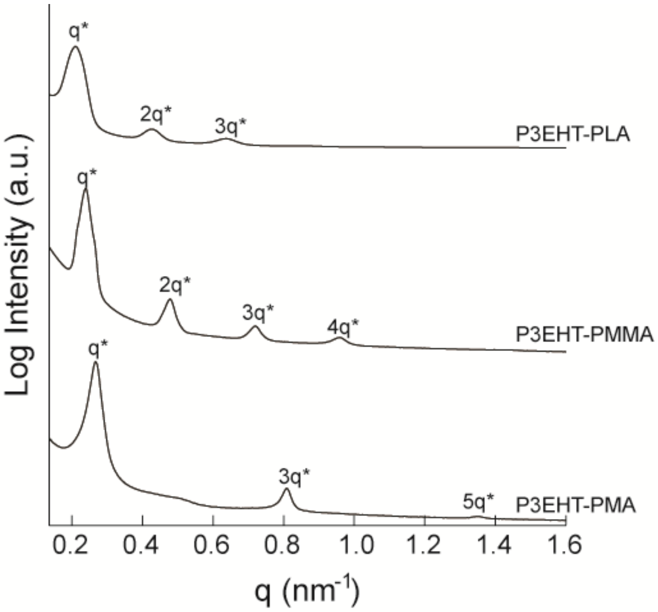

Figure 4.5: Small-angle x-ray scattering profiles of P3EHT-containing block copolymers

Small-angle x-ray scattering (SAXS) profiles of P3EHT-containing block copolymers of various chemistries [poly(3-(2-ethylhexyl)thiophene-*b*-poly(methyl methacrylate) (P3EHT-PMMA) and poly(3-(2-ethylhexyl)thiophene-*b*-poly(methyl acrylate) (P3EHT-PMA)] in the solid state. All samples self-assemble into lamellar morphologies evidenced by integer multiples of q^*. The depressed melting transition of P3EHT relative to P3HT allows for the observation of self-assembled periodic nanostructures due to crystallization within structures formed from the inhomogeneous melt.

4.4 Conclusions

We have synthesized a series of P3EHT-PLA block copolymers, using controlled polymerization techniques such that the polymers have controllable molecular weights and compositions with narrow molecular weight distributions. The use of a poly(3-alkylthiophene) derivative with a lowered crystallization temperature lead to the facile self-assembly of the P3EHT-PLA block copolymers as well as P3EHT-PMMA and P3EHT-PMA. Importantly, P3EHT-PLA block copolymers form microstructures where the P3EHT block serves as the majority phase. Furthermore, we observe an increase in melting temperature and diffraction peak intensity in P3EHT-PLA block copolymers where the conjugated polymer is the majority phase. These data are consistent with confinement of the crystalline P3EHT domains to the nanoscopic length scale which decreases the conformational entropy gained by melting. Because the P3EHT domains remain semicrystalline, the block copolymers can self-assemble on the 10 nm length scale while retaining the high charge transport properties commonly associated with poly(3-alkythiophenes).

Acknowledgements. Support provided through an NSF CAREER award and the National Science Foundation for a graduate. Work on materials characterization was supported by the U.S. Department of Energy, Office of Basic Energy Sciences, Division of Materials Sciences and Engineering under Contract No. DE-AC02-05CH11231. Parts of the X-ray scattering studies were carried out at the Advanced Light Source (ALS) on Beamline 7.3.3. The Advanced Light Source is supported by the Director, Office of Science, Office of Basic Energy Sciences, of the U.S. Department of Energy under Contract No. DE-AC02-05CH11231. Additional X-ray scattering studies were carried out at the Stanford Synchrotron Radiation Laboratory (SSRL), a national user facility operated by Stanford University on behalf of the U.S. Department of Energy, Office of Basic Energy Sciences on Beamline 1-4. Transmission electron microscopy performed by Bryan L. McCulloch. BLM gratefully acknowledges partial support from the Dow Advanced Materials graduate fellowship. Time of flight (ToF) mobility measurements conducted by Chris Shuttle, Martin Burkhardt, and Michael Chabinyc. CS, MGB, and MLC are supported as part of the Center for Energy Efficient Materials, an Energy Frontier Research Center funded by the U.S. Department of Energy, Office of Science, Office of Basic Energy Sciences under Award Number DE-SC0001009

4.5 Appendix

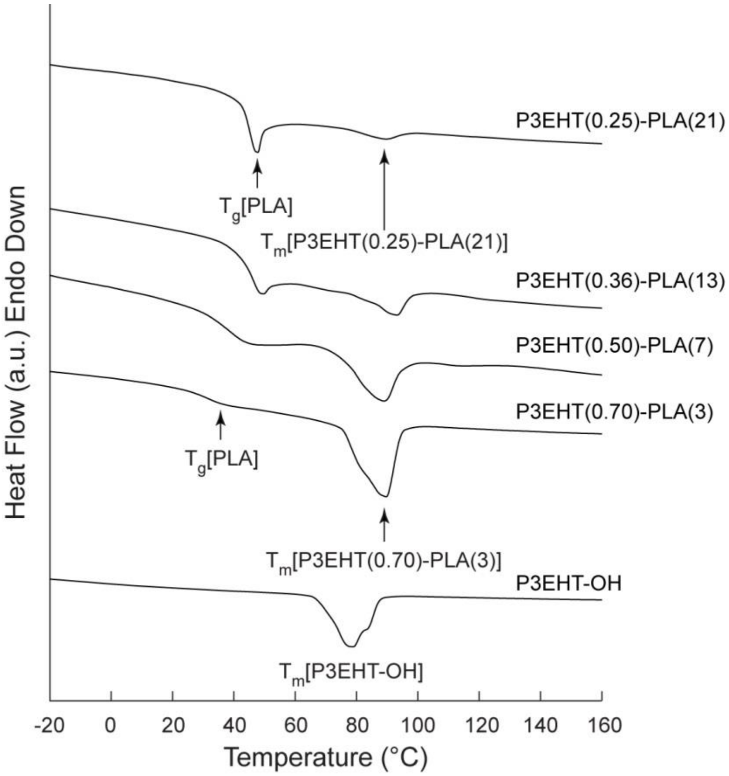

Figure 4.6: Representative DSC thermograms for P3EHT-PLA block copolymers

Representative DSC thermograms for the P3EHT-OH homopolymer and P3EHT-PLA block copolymers. Note that the peak for the melting transition temperature I of the P3EHT increases by ~10 °C when the moiety is confined in the ordered block copolymers. The melting transition temperature remains approximately constant for all P3EHT-PLA samples. As the molecular weight of the PLA blocks are increased, the glass transition temperature (T_g) of the PLA moiety increases before reaching a plateau, as expected.

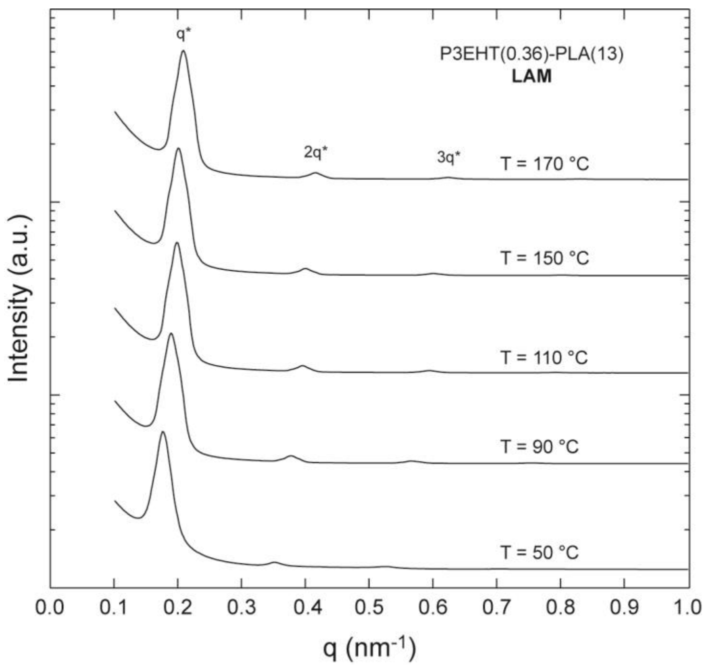

Figure 4.7: Representative temperature dependent SAXS of P3EHT-PLA

Representative P3EHT-PLA SAXS data as a function of temperature. The polymer sample was allowed to equilibrate for 20 min at each temperature prior to beam exposure. For this lamellar sample [P3EHT(0.36)-PLA(13)] the *q**, 2*q**, and 3*q** reflections are clearly visible at elevated temperatures. These data demonstrate the stability of the P3EHT-PLA block copolymer morphologies in the solid state (T = 50 °C) and in the melt (T > 80 °C) until temperatures near the thermal degradation temperature of the PLA block (T ~180 °C). Note that these microstructures are present both upon heating (90 °C and 150 °C) and cooling (170 °C, 110 °C, and 50 °C) the samples.

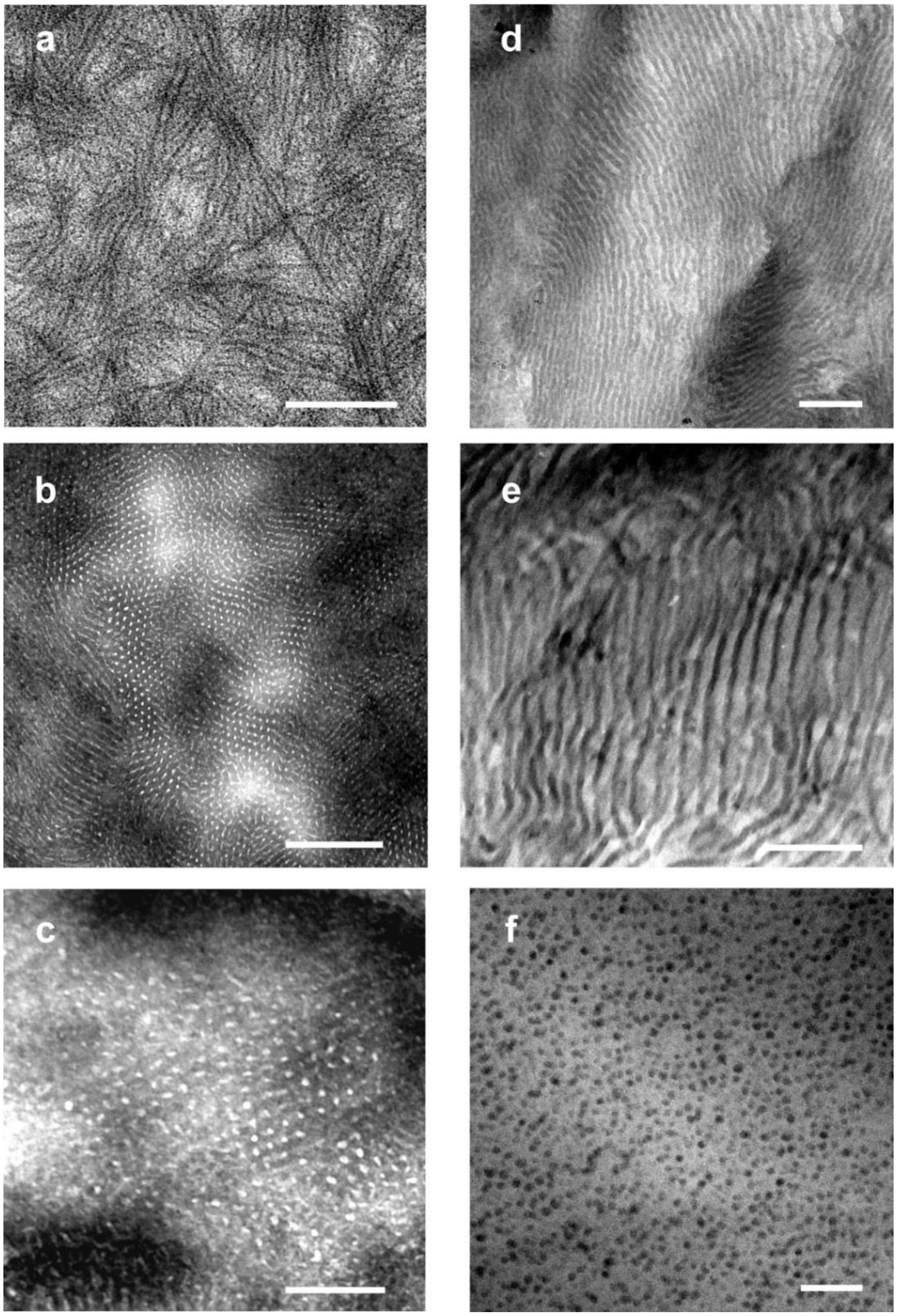

Figure 4. 8: Transmisssion electron micrographs of P3EHT-PLA samples

Enlarged and additional TEM images of (a) unstained P3EHT-OH nanofibrils and the stained microstructures of the hexagonally-packed (b) P3EHT(0.70)-PLA(3) and (c)P3EHT(0.63)-PLA(4). Also, the lamellar (d) P3EHT(0.50)-PLA(7) and I P3EHT(0.36)-PLA(13) are shown. Finally, (f) shows the disordered micelles of P3EHT(0.12)-PLA(56). The bulk TEM samples were annealed at 150 °C for 48 h under high vacuum and thinly sliced (~70 nm) using a microtome. The P3EHT moiety was stained dark in the block copolymer samples by exposing the samples to RuO_4 vapors for 30-50 min. All scale bars represent 200 nm.

4.6 References

1. Olsen, B. D.; Segalman, R. A. Self-assembly of rod-coil block copolymers. *Mat Sci Eng R* **2008,** *62*, 37.

2. Ho, C. C.; Lee, Y. H.; Dai, C. A.; Segalman, R. A.; Su, W. F. Synthesis and Self-assembly of Poly(diethylhexyloxy-p-phenylenevinylene)-b-poly(methyl methacrylate) Rod-Coil Block Copolymers. *Macromolecules* **2009,** *42* (12), 4208.

3. Botiz, I.; Darling, S. B. Optoelectronics using block copolymers. *Materials Today* **2010,** *13* (5), 42.

4. Darling, S. B. Block copolymers for photovoltaics. *Energy & Environmental Science* **2009,** *2* (12), 1266.

5. Olsen, B. D.; Shah, M.; Ganesan, V.; Segalman, R. A. Universalization of the phase diagram for a model rod-coil diblock copolymer. *Macromolecules* **2008,** *41* (18), 6809.

6. McCullough, R. D. The Chemistry of Conducting Polythiophenes. *Adv Mater* **1998,** *10* (2), 93.

7. Osaka, I.; McCullough, R. D. Advances in Molecular Design and Synthesis of Regioregular Polythiophenes. *Accounts Chem Res* **2008,** *41* (9), 1202.

8. Peet, J.; Heeger, A. J.; Bazan, G. C. "Plastic" Solar Cells: Self-Assembly of Bulk Heterojunction Nanomaterials by Spontaneous Phase Separation. *Accounts Chem Res* **2009,** *42* (11), 1700.

9. Iovu, M. C.; Craley, C. R.; Jeffries-EL, M.; Krankowski, A. B.; Zhang, R.; Kowalewski, T.; McCullough, R. D. Conducting regioregular polythiophene block copolymer nanofibrils synthesized by reversible addition fragmentation chain transfer polymerization (RAFT) and nitroxide mediated polymerization (NMP). *Macromolecules* **2007,** *40* (14), 4733.

10. Iovu, M. C.; Jeffries-El, M.; Zhang, R.; Kowalewski, T.; Mccullough, R. D. Conducting block copolymer nanowires containing regioregular poly(3-hexylthiophene) and polystyrene. *J Macromol Sci Par A Pure Appl Chem* **2006,** *43* (12), 1991.

11. Higashihara, T.; Ohshimizu, K.; Hirao, A.; Ueday, M. Facile Synthesis of ABA Triblock Copolymer Containing Regioregular Poly(3-hexylthiophene) and Polystyrene Segments via Linking Reaction of Poly(styryl)lithium. *Macromolecules* **2008,** *41* (24), 9505.

12. Dai, C. A.; Yen, W. C.; Lee, Y. H.; Ho, C. C.; Su, W. F. Facile synthesis of well-defined block copolymers containing regioregular poly(3-hexyl thiophene) via anionic macroinitiation method and their self-assembly behavior. *J Am Chem Soc* **2007,** *129* (36), 11036.

13. Ho, V.; Boudouris, B. W.; Segalman, R. A. Tuning Polythiophene Crystallization through Systematic Side Chain Functionalization. *Macromolecules* **2010,** *43* (19), 7895.

14. Loewe, R. S.; Khersonsky, S. M.; McCullough, R. D. A simple method to prepare head-to-tail coupled, regioregular poly(3-alkylthiophenes) using grignard metathesis. *Adv Mater* **1999,** *11* (3), 250.

15. Loewe, R. S.; Ewbank, P. C.; Liu, J.; Zhai, L.; McCullough, R. D. Regioregular, Head-to-Tail Coupled Poly(3-alkylthiophenes) Made Easy by the GRIM Method: Investigation of the Reaction and the Origin of Regioselectivity. *Macromolecules* **2001,** *34* (13), 4324.

16. Boudouris, B. W.; Frisbie, C. D.; Hillmyer, M. A. Nanoporous Poly(3-alkylthiophene) Thin Films Generated from Block Copolymer Templates. *Macromolecules* **2008,** *41* (1), 67.

17. Boudouris, B. W.; Frisbie, C. D.; Hillmyer, M. A. Polylactide−Polythiophene−Polylactide Triblock Copolymers. *Macromolecules* **2010,** *43* (7), 3566.

18. Liu, J. S.; Sheina, E.; Kowalewski, T.; McCullough, R. D. Tuning the electrical conductivity and self-assembly of regioregular polythiophene by block copolymerization: Nanowire morphologies in new di- and triblock copolymers. *Angew Chem Int Edit* **2001,** *41* (2), 329.

19. Schmidt, S. C.; Hillmyer, M. A. Synthesis and characterization of model polyisoprene-polylactide diblock copolymers. *Macromolecules* **1999,** *32* (15), 4794.

20. Hillmyer, M. Block copolymer synthesis. *Current Opinion in Solid State & Materials Science* **1999,** *4* (6), 559.

21. Botiz, I.; Darling, S. B. Self-Assembly of Poly(3-hexylthiophene)-block-polylactide Block Copolymer and Subsequent Incorporation of Electron Acceptor Material. *Macromolecules* **2009,** *42* (21), 8211.

22. Olsen, B. D.; Segalman, R. A. Structure and thermodynamics of weakly segregated rod-coil block copolymers. *Macromolecules* **2005,** *38* (24), 10127.

23. Segalman, R. A.; Olsen, B. D.; Shah, M.; Ganesan, V. Universalization of the phase diagram for a model rod-coil diblock copolymer. *Macromolecules* **2008,** *41* (18), 6809.

24. Semenov, A. N.; Vasilenko, S. V. Theory of the nematic-semectic-A transition in a melt of macromolecules consisting of a rigid and a flexible block. *J Exp Theor Phys* **1986,** *63* (1), 70.

25. Olsen, B. D.; Segalman, R. A. Nonlamellar phases in asymmetric rod-coil block copolymers at increased segregation strengths. *Macromolecules* **2007,** *40* (19), 6922.

26. Kumar, N. A.; Ganesan, V. Communication: Self-assembly of semiflexible-flexible block copolymers. *J Chem Phys* **2012,** *136* (10).

27. Mcculloch, I.; Heeney, M.; Bailey, C.; Genevicius, K.; Macdonald, I.; Shkunov, M.; Sparrowe, D.; Tierney, S.; Wagner, R.; Zhang, W. M.; Chabinyc, M. L.; Kline, R. J.; Mcgehee, M. D.; Toney, M. F. Liquid-crystalline semiconducting polymers with high charge-carrier mobility. *Nat Mater* **2006,** *5* (4), 328.

28. Zhang, R.; Li, B.; Iovu, M. C.; Jeffries-EL, M.; Sauve, G.; Cooper, J.; Jia, S. J.; Tristram-Nagle, S.; Smilgies, D. M.; Lambeth, D. N.; McCullough, R. D.; Kowalewski, T. Nanostructure dependence of field-effect mobility in regioregular poly(3-hexylthiophene) thin film field effect transistors. *J Am Chem Soc* **2006,** *128* (11), 3480.

29. Lunt, R. R.; Benziger, J. B.; Forrest, S. R. Relationship between Crystalline Order and Exciton Diffusion Length in Molecular Organic Semiconductors. *Adv Mater* **2010,** *22* (11), 1233.

30. Street, R. A.; Northrup, J. E.; Salleo, A. Transport in polycrystalline polymer thin-film transistors. *Physical Review B* **2005,** *71*.

31. Olsen, B. D.; Alcazar, D.; Krikorian, V.; Toney, M. F.; Thomas, E. L.; Segalman, R. A. Crystalline structure in thin films of DEH-PPV homopolymer and PPV-b-PI rod-coil block copolymers. *Macromolecules* **2008,** *41* (1), 58.

32. Segalman, R. A.; Olsen, B. D.; Alcazar, D.; Krikorian, V.; Toney, M. F.; Thomas, E. L. Crystalline structure in thin films of DEH-PPV homopolymer and PPV-b-PI rod-coil block copolymers. *Macromolecules* **2008,** *41* (1), 58.

33. Mauer, R.; Kastler, M.; Laquai, F. The Impact of Polymer Regioregularity on Charge Transport and Efficiency of P3HT:PCBM Photovoltaic Devices. *Adv Funct Mater* **2010,** *20* (13), 2085.

34. Kreouzis, T.; Kumar, A.; Baklar, M. A.; Scott, K.; Stingelin-Stutzmann, N. Efficient, Stable Bulk Charge Transport in Crystalline/Crystalline Semiconductor-Insulator Blends. *Adv Mater* **2009,** *21* (44), 4447.

35. Ballantyne, A. M.; Chen, L.; Dane, J.; Hammant, T.; Braun, F. M.; Heeney, M.; Duffy, W.; McCulloch, I.; Bradley, D. D. C.; Nelson, J. The effect of poly(3-hexylthiophene) molecular weight on charge transport and the performance of polymer : fullerene solar cells. *Adv Funct Mater* **2008,** *18* (16), 2373.

36. Moon, H. C.; Bae, D.; Kim, J. K. Self-assembly of Poly(3-dodecylthiophene)-block-poly(methyl methacrylate) Copolymers Driven by Competition between Microphase Separation and Crystallization. *Macromolecules* **2012,** *45* (12), 5201.

Chapter 5: Crystalline Structure in Lamellar Poly(3-alkylthiophene)-containing Block Copolymers

As discussed in Section 1.2.3, upon cooling from the melt the adopted solid-state morphology of semicrystalline block copolymers is dictated by the competition between the crystallization of the crystallizable block and the preexisting microphase separated melt. At the crystallization temperature of the semicrystalline component, if the amorphous component is glassy or the strength of segregation is sufficiently high, crystallization can proceed within confined block copolymer domains without significantly affecting the periodic structure. In Chapter 4, it was shown that self-assembled morphologies can be observed in the melt and semicrystalline state of block copolymers that contain a low melting point poly(3-alkylthiophene) (P3AT) as the semiconducting component. Importantly, microphase separation was observed to occur in various different chemistries. However, it was not presented how the melt phase structure from which crystallization proceeds affects the observed thermal properties and crystallite structure.

In this chapter, we present the crystallization and structure of the semiflexible-flexible system, poly(3-(2-ethylhexyl)thiophene)-*b*-poly(methyl acrylate) (P3EHT-PMA). The well-established body of literature on flexible-flexible semicrystalline block copolymers provides a convenient starting point for understanding conjugated block copolymers, but as discussed in Sections 1.2.1-1.2.2, increasing the rigidity of the conjugated moiety can result in anisotropic molecular ordering in addition to conventional spatial periodicity observed at longer (10-100 nm) length scales. The complexity in the self-assembly of semiflexible block copolymers is amplified by the potential coupling between the Flory-Huggins and Maier-Saupe interaction parameter, which can induce orientational ordering in regions of phase space not expected in the homopolymer. In this particular system, crystallization proceeds from the inhomogeneous melt in which chains are highly stretched relative to their unperturbed state. As a result, the crystallites are shown to adopt a preferential orientation relative to the block copolymer interfaces with the chain axis parallel to the lamellar normal.

5.1 Introduction

Periodic features on sub-100 nm length scales have been proposed as a potential method to improve the efficiency of organic electronic devices. Specifically, the optimization of exciton harvesting and charge collection in organic photovoltaics[1-2] may be possible with reliable control over nanostructures possessing feature sizes commensurate with the exciton diffusion length. Block copolymers present the unique advantage of self-assembly at the sub-100 nm length scale[3-5] which is difficult to otherwise achieve in a scalable fashion. However, it is well-known that the self-assembly of block copolymers in which one component is semicrystalline and the other is amorphous requires balancing the driving forces for crystallization and microphase segregation.[6-7] From such an understanding, the structure of numerous different semicrystalline block copolymer chemistries have been predictively controlled.[8-9] Importantly, included in this body of literature is the self-assembly of poly(3-alkylthiophene) (P3AT) containing block copolymers,[10-13] a class of molecules which have been extensively studied in organic optoelectronics.[14-15]

Although the self-assembly of P3AT-containing block copolymers has been shown to control the structure at the 10-100 nm length scale, it is well-known that the optoelectronic properties of organic semiconductors are highly dependent on the crystalline structure at multiple length scales. At small length scales, the rate of electron transport has been described by Marcus theory, in which the efficiency of the electron transfer process is dependent on the transfer integral and the renormalization energy.[16] Generally, the transfer integral describes the orbital overlap between adjacent molecules in the crystalline state, and therefore can be dependent highly on the shape of conjugated molecules.[17-19] From this, charge transport mobility has been observed to be anisotropic when measurements are conducted along particular unit cell axes in single crystals of polymers[20-21] and small molecules.[22-25] In addition to single crystal devices, the hole mobility in semicrystalline polymer thin films is observed to be dependent on the probed direction relative to crystalline axes as well but is proposed to be highly affected by the presence and nature of grain boundaries in addition to intracrystallite considerations.[26-28]

As such, potential crystallite orientation within block copolymer domains arising from confinement of the semicrystalline domain presents an interesting opportunity to control the optoelectronic properties. Orientational templating of crystallites within block copolymers has been studied for semicrystalline systems in the past including polyethylene, poly(ethylene oxide), and poly(ε-caprolactone).[6,29-33] Building on these works, the orientation of crystallites has been shown to depend heavily on the structure of the melt or solution phase structure from which crystallization proceeds. Work on polyethylene-containing block copolymers showed through pole figure analysis of aligned samples that the orientation of crystallite stems in lamellar samples confined to microphase separated domains in the melt were found to orient perpendicular to the lamellar normal.[30,34-35] Though this orientation appears counterintuitive from the standpoint of classical homopolymer crystallite growth processes, this orientation is preferable when the crystalline long period is incommensurate with the block copolymer domain size. However, the orientation was proposed to adopt crystallite stems parallel to the lamellar normal if a polyethylene block copolymer was crystallized from the homogeneous (or weakly segregated) melt.[36-37] In addition to differences in the crystallite orientation when crystallizing from either the strongly-segregated as opposed to the disordered melt, the temperature dependence of the orientation in poly(ethylene oxide)-*b*-polystyrene was shown to be correlated with the degree of chain crowding at the interface.[38-40] From these works, it can be seen that crystallite orientation within the semicrystalline domain is highly dependent on the melt phase structure.

However, in spite of this large body of literature on semicrystalline block copolymers, the studied semicrystalline component had a flexible chain shape. While the persistence length of polyethylene and poly(ethylene oxide) are 0.57 nm and 0.41 nm,[41] respectively, the value for conjugated polymers are typically at least an order of magnitude larger, with P3ATs in particular having a persistence length of ~3 nm.[42-45] Work on rod-coil block copolymers, theoretically and experimentally has shown that orientational ordering in the melt due to packing constraints arising from the molecular shape can force the backbone of the rod-like moiety to lie perpendicular (or at a slight tilt) to the interface even at low strengths of segregation, χN.[46-50] Importantly with sufficiently high rod-rod interactions upon cooling from the isotropic phase, a transition to the nematic phase (in which the polymer backbones are aligned) will necessarily precede microphase separation.[47] As the contour length of the polymer is increased to be on the order of the persistence length, a transition from the rigid rod-like to the semiflexible regime is approached. Importantly, many conjugated polymers used in organic electronic devices lie in this semiflexible regime. Although the structure and phase behavior of conjugated-flexible block copolymers have not been deeply explored experimentally, theoretical work on the phase behavior as a function of the persistence length has been presented.[51-52] From these works, rod-coil block copolymer behavior in which large regions of phase space are dictated by orientationally ordered (liquid crystalline) phases can be recovered even in the case of polymers with less rigid backbones at sufficiently high rod-rod interaction or high volume fraction of the semiflexible components.

Interestingly, though the structural characterization of crystallization within block copolymer domains has been extensively examined in non-conjugated polymers, functional block copolymers in which one of the components is optoelectronically-active have not been studied. In these systems, conjugation along the backbone and sterics of large solubilizing groups leads to high bending energies for polymer chains and relatively long persistence lengths relative to that of more conventionally-studied semicrystalline polymers.[42-43,45] In this chapter, we present the thermal and structural characterization of optoelectronically-active crystallites within self-assembled lamellar domains. Crystallization is observed to proceed from the inhomogenous melt and scaling of the domain suggests that chains are highly stretched. Furthermore, the orientation of these crystallites within self-assembled domains is examined, and it is proposed to be highly dependent on the elongated chain shape in the melt. Understanding the orientation of crystallites in this system provides an outlook for predictive control over crystalline orientation in the future.

5.2 Experimental

5.2.1 General Methods

^{1}H NMR spectra were acquired on a Bruker AV-500 spectrometer using deuterated chloroform (Cambridge) as the solvent. Molecular weights were determined by end group analysis of the ^{1}H NMR spectra and confirmed, when possible, with matrix assisted laser desorption/ionization (MALDI) performed on a Voyager DE MALDI-TOF with terthiophene as the matrix. Gel permeation chromatography (GPC) data were collected on a Viscotek TDA 302 with four Viscotek T-columns (one T-6000, T-5000, T-4000, and T-3000 column). The response was measured using a refractive index (RI) detector. Tetrahydrofuran (THF) at 35 °C was used as the mobile phase at a flow rate of 1 mL min^{-1}. The instrument was calibrated with polystyrene (PS) standards (Polymer Source). Differential scanning calorimetry (DSC) was performed on a Thermal Advantage Q20 calorimeter at a scan rate of 10 °C min^{-1} unless otherwise noted. An indium standard was used to calibrate the instrument and nitrogen was used as the purge gas. Picnometry was performed at room temperature with water as the fluid.

Sample preparation. Samples for powder patterns of small- and wide-angle x-ray scattering were pressed in aluminum washers at 120°C. Block copolymer samples were annealed 150°C overnight under vacuum. Aligned samples were obtained by hot pressing between Kapton™ sheets with aluminum spacers to maintain constant thickness. Samples were allowed to cool to room temperature slowly under vacuum overnight. Semicrystalline aligned samples were obtained after melting crystallites at 120°C and held at various crystallization temperatures for upwards of two weeks to allow for complete crystallization. Aligned samples were placed in Tzero hermetically-sealed aluminum pans for DSC measurements.

5.2.2 Detailed Synthetic Procedure

Materials. All reagents and solvents were used as received from Sigma-Aldrich unless otherwise noted. Tetrahydrofuran (THF) was degassed, dried overnight on CaH_2, and distilled into air-free flasks. N,N,N',N',N"-pentamethyldiethylenetriamine (PMDETA) and methyl acrylate were passed through basic alumina columns prior to use.

Representative Synthesis of Ethynyl-terminated Poly(3-(2-ethylhexyl)thiophene) (P3EHT-ethynyl). General procedure for synthesis of ethynyl-terminated P3AT follows GRIM method presented by McCullough and coworkers. A 250 mL three neck flask was flame-dried and back-filled with nitrogen. 2,5-dibromo-3-(2-ethylhexyl)thinophene (14.6 g, 41.2 mmol) was added by syringe followed by addition of THF dried over CaH_2. A solution of 2.0 M *tert*-butylmangesium chloride (20.6 mL, 41.2 mmol) in diethyl ether was added by syringe and the reaction solution was refluxed for 90 minutes. After cooling to room temperature, dry $Ni(dppp)Cl_2$ (492 mg, 0.91 mmol) was added and the solution was allowed to react for 45 minutes. The reaction was terminated with addition of 0.5M ethynylmagnesium chloride (20.6 mL, 10.3 mmol) in THF. Termination was allowed to proceed for 2 min, and the polymer was then precipitated in methanol and collected by centrifugation. The powder was then extracted with acetone and hexanes. Note that a Soxhlet extraction was not performed, as it has been shown that heat results in coupling of the ethynyl product. The product was collected by precipitation from the hexanes phase in methanol, dried overnight under vacuum, and stored in the freezer.

Representative Synthesis of Bromine-terminated Poly(methyl acrylate) (PMA-Br). General procedure for synthesis of bromine-terminated poly(methyl acrylate) follows atom transfer radical polymerization (ATRP) method popularized by Matyjaszewski and coworkers. Methyl acrylate (10 mL, 110 mmol), ethyl α-bromoisobutyrate (73.6 μL, 0.5 mmol), cuprous bromide (41.7 mg, 0.29 mmol), and PMDETA (60.7 μL, 0.29 mmol) were combined in a 20 mL Schlenk flask. The reaction solution was degassed with three freeze-pump-thaw cycles and the reaction was allowed to proceed at 75 °C. The reaction time was varied to control the molecular weight of the polymer. Reaction was quenched to room temperature, dissolved in chloroform, and passed through a basic alumina column to remove residual copper. Solvent and unreacted monomer were removed with vacuum and PMA was collected. Polymer was dried overnight under vacuum.

Representative Synthesis of Azide-terminated Poly(methyl acrylate) (PMA-N_3). PMA-Br (1 g, 0.12 mmol) and sodium azide (0.118 g, 1.8 mmol) were combined in 5 mL of N,N-dimethylformamide. The reaction was allowed to proceed for 24 hours at room temperature. The reaction was diluted with chloroform and passed through a silica gel column. Solvent was removed under vacuum and the polymer was dried overnight.

Representative Synthesis of Poly(3-(2-ethylhexyl)thiophene)-*b*-poly(methyl acrylate) (P3EHT-PMA). General procedure for synthesis of bromine-terminated poly(methyl acrylate) follows Azide-alkyne Huisgen cycloaddition of P3EHT-ethynyl and PMA-N_3. PMA-N_3 (0.5 g, 60 μmol), P3EHT-ethynyl (0.46 g, 90 μmol), cuprous bromide (6.5 mg, 45 μmol), and PMDETA (9.4 μL, 45 μmol) were combined in 4 mL of THF in a 10 mL Schlenk flask. The reaction solution was degassed with three freeze-pump-thaw cycles and the reaction was allowed to proceed for 20 hours at room temperature. The solution reaction was diluted with chloroform and passed through a basic alumina column to remove residual copper and precipitated in cold petroleum ether. The excess P3EHT (1.5 molar) was soluble in petroleum ether and did not precipitate out. The purified block copolymer was collected via centrifugation and dried overnight under vacuum.

5.2.3 Structural Characterization

All x-ray scattering experiments were conducted in transmission mode. WAXS experiments were carried out at beam line 1-4 of the Stanford Synchrotron Radiation Lightsource (SSRL) with an incident energy of 8.3 keV and a sample-detector distance of ~200 mm. SAXS measurements were performed in part at beam line 1-4 of SSRL with a sample-detector distance of ~1000 mm and at the Advanced Light Source (ALS) with an incident energy of 10 keV and a sample-detector distance ~3000 mm. The longer sample-detector distance was necessary for characterization of P3EHT-PMA (37.8). Configurations were calibrated with a silver behenate (AgBe) standard. Domain sizes were determined by fit of the primary peak location to Bragg's law $d=2\pi/q$. Analysis was performed with the Nika package to Igor.[53]

5.3 Results and Discussion

5.3.1 Synthesis of Poly(3-(2-ethylhexyl)thiophene)-*b*-Poly(methyl acrylate)

Poly(3-(2-ethylhexyl)thiophene)-*b*-poly(methyl acrylate) (P3EHT-PMA) was synthesized from azide-alkyne Huisgen cycloaddition of ethynyl-functional P3EHT and azide-terminated PMA (Figure 5.1). Such a reaction scheme has been reported in the past for the synthesis of block copolymers containing a conjugated polymer such as poly(3-hexylthiophene).[11-12,54-56] Ethynyl-functional P3EHT was synthesized following the GRIM polymerization scheme developed by McCullough and coworkers.[57-58] The molecular weight was controlled by varying the catalyst to monomer ratio, and the reaction was terminated with ethynylmagnesium chloride to form telechelic polymers. Though it has been reported that difunctional polymer can be formed under these reaction conditions,[58] significant populations of ABA-type triblock were not observed after coupling reactions. It should also be noted that the ethynyl-terminated P3EHT was kept in the freezer to prevent the thermally-activated coupling observed in ethynyl-terminated P3HT.[55-56] Azide-functionalized poly(methyl acrylate) (PMA-N_3) was synthesized by reaction of PMA-Br [obtained via atom transfer radical polymerization (ATRP)] with excess sodium azide. After the coupling reaction, excess unreacted P3EHT was removed by precipitation in cold petroleum ether, and purified product was collected by centrifugation. Molecular characteristics of the polymers are provided in Table 1. The molecular weight of the thiophene component varies over the range of 5 to 15.5 kg/mol and the block copolymer volume fractions varied between 0.42 and 0.49.

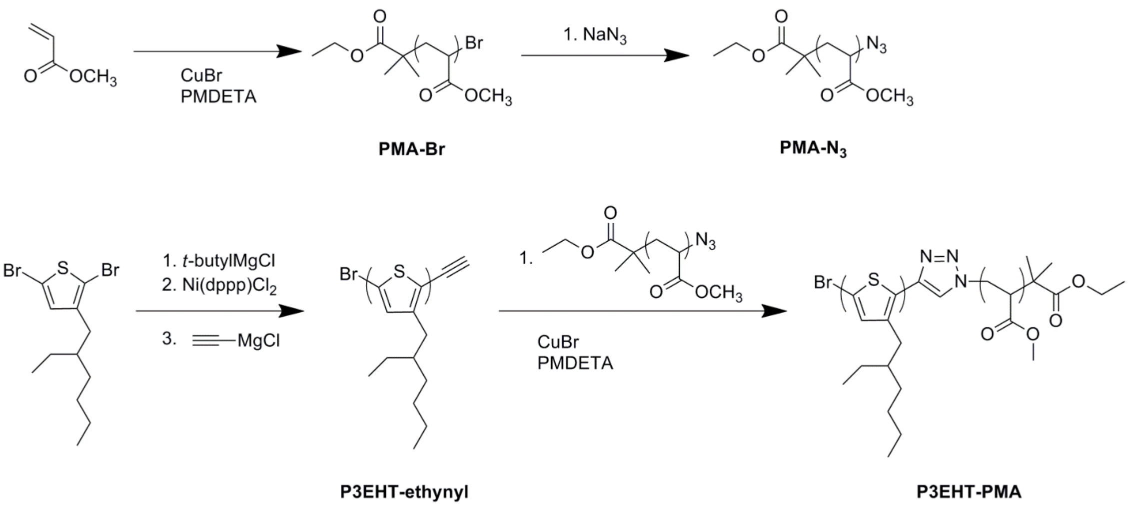

Figure 5.1: Synthetic scheme of P3EHT-PMA block copolymers

Synthesis of P3EHT-PMA block copolymers via an azide-alkyne Huisgen cycloaddition of ethynyl-terminated P3EHT and azide-terminated PMA. Bromine-terminated PMA, synthesized via ATRP, was reacted with sodium azide to obtain PMA-N_3. Ethynyl-terminated P3EHT was obtained following the Grignard metathesis polymerization scheme developed by McCullough and coworkers.

Table 5.1: Summary of P3EHT-PMA polymer sample characteristics

Sample[a]	M_n[b] (kg/mol) *P3EHT*	L/l_p[c]	M_n (kg/mol) *P3EHT-PMA*	f_{P3EHT}[d]	M_w/M_n[b]	d (nm)[e]	d_{3EHT} (nm)	T_m (°C)[f]
P3EHT-PMA (12.3)	5	3.2	12.3	0.42	1.11	20	8.2	83
P3EHT-PMA (17.0)	8	5.2	17.0	0.49	1.17	28	13.9	87
P3EHT-PMA (37.8)	15.5	10.1	37.8	0.43	1.20	57	24.7	80

[a] P3EHT-PMA block copolymers represented by molecular weight of total. [b] As determined by gel permeation chromatography against polystyrene standards. [c] The ratio of the contour length (using a monomer length of 0.38 nm) and the persistence length measured with SANS.[45] From these values the polymer should behave as a semiflexible chain in contrast with a rigid rod or a Gaussian coil. [d] As determined by ^1H NMR spectroscopy of the purified block copolymer. Volume fractions presented for melt phase. [e] Domain size determined from the primary scattering peak ($2\pi/q^*$) in the melt (120°C). [f] The final melting peak as observed in differential scanning calorimetry (DSC) for samples crystallized at 25°C.

5.3.2 Thermal Characterization

At room temperature P3EHT has been shown to crystallize into a semicrystalline state from differential scanning calorimetry (DSC) heating traces.[59-60] P3EHT homopolymers crystallized at 25°C exhibit melting transition temperatures that increase from 74°C to 80°C and 88°C with increasing molecular weight (Figure 5.2). The presence of multiple endotherms on heating is a commonly observed phenomenon in semicrystalline polymers and has been ascribed to melt-recrystallization processes which has been discussed in more detail in Chapter 2.[61-64] At lower temperatures, smaller or less perfect crystallites melt and recrystallize into more thermodynamically stable structures, which then melt at elevated temperatures. Evidence of the presence of melt-recrystallization in these systems can be observed by increasing the crystallization temperature to 55°C resulting in a single melting endotherm as less-perfect crystallites are no longer stable during crystallization (Figure 5.3a).[64]

Crystallinity in the P3EHT-PMA block copolymers can similarly be confirmed with DSC. Upon heating from room temperature block copolymers exhibit a glass transition of the PMA domains and melting endotherms at higher temperatures from the P3EHT domains. However, while in many other semicrystalline block copolymers systems the melting temperature of the crystallizable component is nearly identical to or slightly depressed from that of the parent homopolymer, the melting temperature of the thiophene component in the block copolymer relative to the parent homopolymer varies depending on the molecular weight. The peak of the endotherm of P3EHT-PMA (37.8) is observed to be 8°C lower than that of the parent homopolymer (Figure 5.2c), but due to the breadth of the endotherm of P3EHT-PMA (37.8), the temperatures at which melting is complete (inferred from the intersection of tangent lines) are nearly identical. The breadth of this peak may be evidence of kinetic restrictions on melt-recrystallization or a broader distribution of crystallites rather than any thermodynamic effect of confinement though this hypothesis remains to be tested. In contrast, the melting transition temperatures of P3EHT-PMA (12.3) and P3EHT-PMA (17.0) are 9°C and 7°C higher than that of parent homopolymers, respectively (Figure 5.2b-c). This positive deviation from the parent homopolymer remains at elevated crystallization temperatures as both homopolymer and block copolymer melting endotherms shift to higher temperatures (Figure 5.3a). Additionally, decreasing the heating rate to 2.5 °C/min results in increases to the relative magnitude of the highest temperature endotherms, though qualitatively the trend in melting points are not affected (Figure 5.3b). Such a result is expected for melt-recrystallization.

While similar or slightly depressed melting points in block copolymers have been observed in the past, a higher melting temperature in confined lamellae is less commonly observed in the literature. An increased melting temperature has been observed in the crystalline-crystalline diblock copolymer, poly(ε-caprolactone)-*b*-poly(ethylene) (PCL-PE).[65] The authors attribute the increased transition temperature to the crystallinity of the polyethylene block at the melting transition of the PCL block. The crystalline PE domain necessarily constrains the interfacial area to the cross-sectional area of the PE unit cell which forces PCL chains to adopt a stretched state upon melting. Such stretching reduces the conformational entropy of the PCL chains in the ordered melt relative to chains at the unperturbed state as would be observed upon melting the PCL homopolymer. Though this hypothesis may be valid in a crystalline-crystalline polymer, drawing analogies to our observations of increased melting transition temperature in the P3EHT-PMA system is complicated by the fact that the rubbery PMA block may not in itself restrict the conformation of the P3EHT chain in the melt as a crystalline or glassy interface

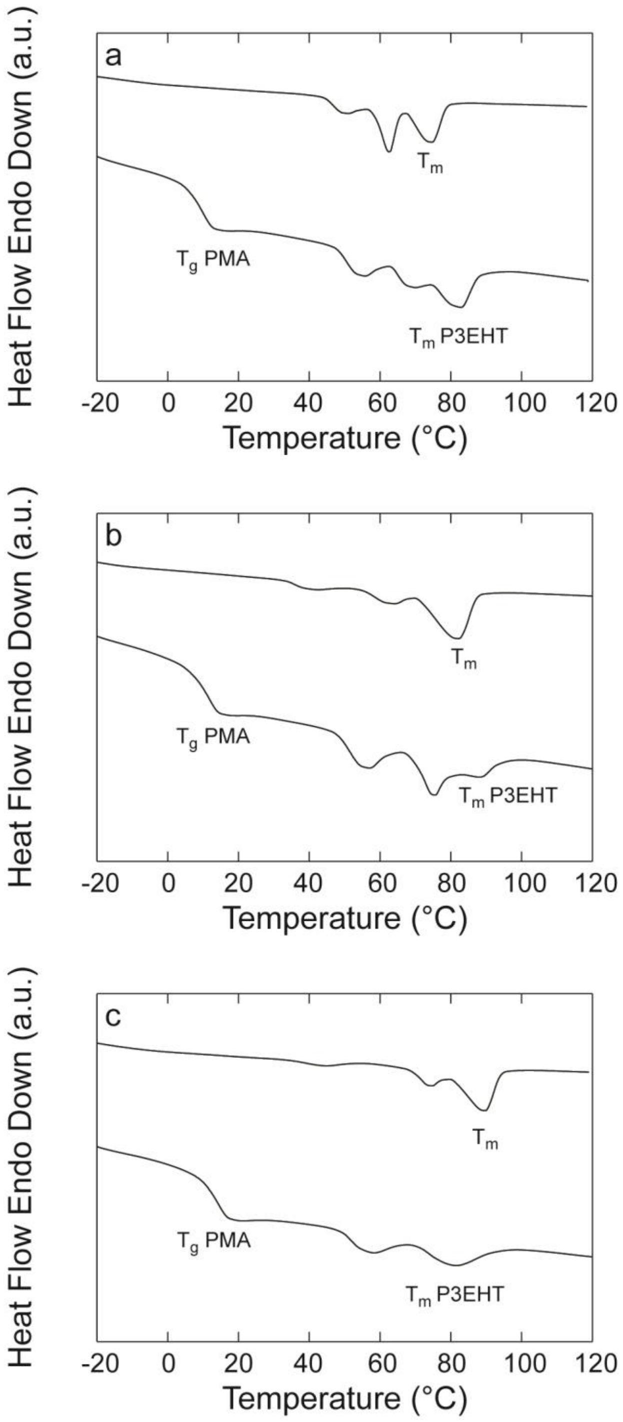

Figure 5.2: Differential scanning calorimetry of P3EHT-PMA block copolymers

Differential scanning calorimetry (DSC) heating traces of block copolymers and parent homopolymers for (a) P3EHT-PMA (12.3), (b) P3EHT-PMA (17.0), and (c) P3EHT-PMA (37.8). Traces are offset for clarity. The final melting point for P3EHT-PMA (12.3) and P3EHT-PMA (17.0) are higher than their corresponding homopolymers whereas the melting point of P3EHT-PMA (37.8) is lower.

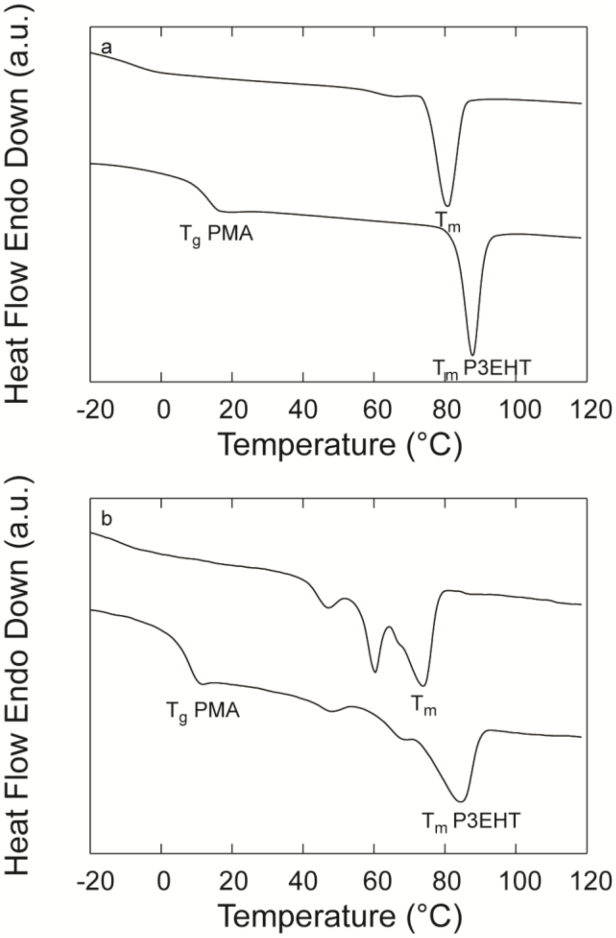

Figure 5.3: DSC traces of P3EHT-PMA (12.3) at varying heating rates

DSC heating traces of P3EHT-PMA (12.3) and the parent P3EHT homopolymer (a) crystallized at 55°C and (b) crystallized at 25°C with a heating rate of 2.5°C/min. Though the features vary between the slow heating and the higher annealing temperature, the final melting point is unaffected. The block copolymer melting transitions are higher than that of the homopolymer under all conditions.

would. Further understanding of the chain shape in the phase separated melt may shed light on the validity of such an argument.

5.3.2 Microphase Separation in the Melt and Solid State

All block copolymers in this study self-assemble into lamellar morphologies in the melt, as indicated by integer multiples of q^* in small-angle x-ray scattering (SAXS) (Figure 5.4a). As expected, increasing the overall molecular weight results in systematic shift in the primary scattering peak to lower q and therefore larger domain spacings. Though it is difficult to determine the exact value of the exponential scaling in these systems from so few samples, a plot of the domain size as a function of overall degree of polymerization results in a best fit exponent of 0.94 (Figure 5.4b). It should be noted that a linear scaling has been observed in rod-coil systems in the past,[49-50] though in these molecular weight regimes the polymer should behave as a semiflexible polymer and not a fully rigid rod. Furthermore, rod-rod interactions, which may transition the polymer to rigid rod-like behavior, has been measured for the homopolymer[59] and was determined to be weak compared to other systems such as poly(phenylene vinylene)[66] and polyfluorene[67]. However, it is possible that a large Flory-Huggins interaction parameter concentrates the stiffer component which results in an enhanced nematic potential.[51] Regardless of the validity of such a hypothesis, a high exponent suggests that the polymer chains are highly stretched in the melt. Importantly, the primary peak for all samples persist upon heating to 160°C and do not decrease in intensity indicating that self-assembled morphologies exist even at elevated temperatures. As such, crystallization of the P3AT moiety of these systems proceeds directly from the inhomogenous melt in all cases.

The highly stretched P3EHT chain conformation is further supported by the ratio of the contour length of the polythiophene moiety to the block copolymer domain size. The width of each domain in the melt can be estimated from the volume fraction of the block copolymer determined from the density of amorphous P3EHT[68] (1.01 g/cm^3) and PMA[69] (1.11 g/cm^3). From these values, the domain sizes of the 3EHT domains are calculated and tabulated in Table 1. For comparison, the contour lengths of the P3EHT components are 9.6, 15.7, and 30.4 nm, only slightly larger than the width of the domain. This supports the claim, though does not sufficiently prove, that the polythiophene chains are elongated perpendicular to the lamellar interface in the melt.

At room temperature, the thiophene chains crystallize (as shown in DSC) and samples retain lamellar morphologies (Figure 5.5a), though an expansion of the block copolymer lamellar domain spacing is evident from the shift of the primary peak of all polymer samples to lower q. Domain sizes for block copolymers in the semicrystalline state can be found in Table 2. It has been suggested[5,34] that an increase in domain spacing, as observed in the P3EHT-PMA system, should be expected if crystallite stems are oriented parallel to the lamellar normal. In short, crystal stems oriented perpendicular to the block copolymer interface results in an increase upon crystallization as the scaling varies from $N^{2/3}$ (in the strongly segregated limit) to linear with N. In contrast, crystallization in the parallel orientation can proceed with little variation to the interfacial area. From this concept, the slight expansion upon crystallization in P3EHT-PMA would therefore suggest that crystallite stems are oriented perpendicular to the lamellar interfaces.

To confirm this hypothesis, block copolymer domains were shear aligned and the crystallite orientation was determined with wide-angle x-ray scattering (WAXS). The alignment

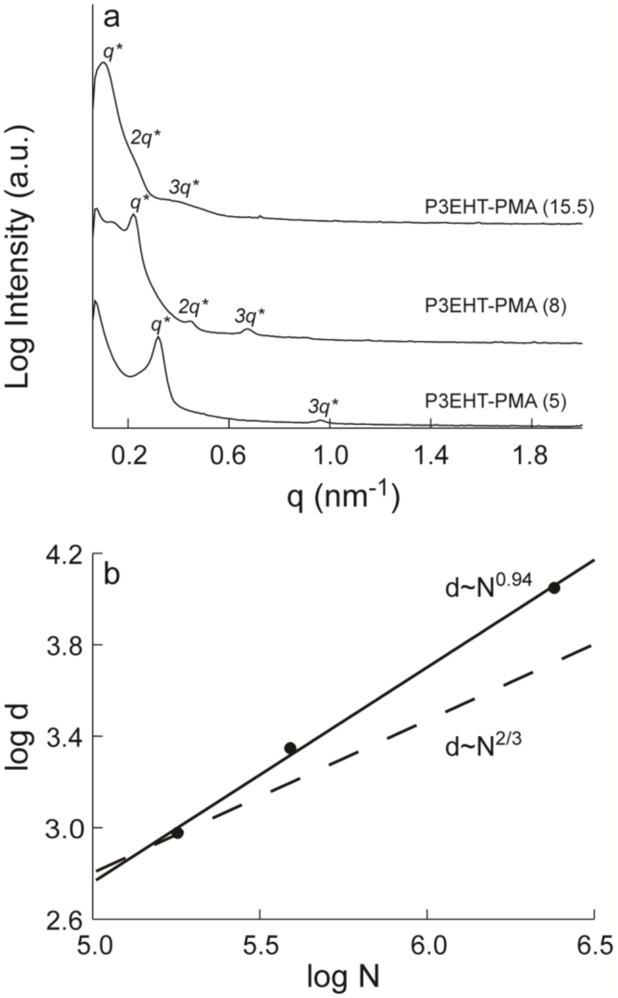

Figure 5.4: Melt phase small-angle x-ray scattering of P3EHT-PMA block copolymers

Melt phase characterization for P3EHT-PMA block copolymers. (a) Small-angle x-ray scattering (SAXS) patterns for all block copolymers. Integer spacings of the primary scattering peak, *q**, indicate that all block copolymers adopt a lamellar morphology. Primary scattering peaks shift to lower *q* with increasing molecular weight indicating an expansion in the lamellar spacing. (b) Domain scaling of block copolymers extracted from *q** in the melt from Bragg's law ($d = 2\pi/q^*$). The solid line represents the best fit line with an exponent of 0.94. As a reference, the dashed line is presented as the expected scaling for a block copolymer in the strongly-segregated limit (SSL).[70] Block copolymers exhibit stronger scaling with degree of polymerization than expected for the SSL approaching the linear spacing expected for rigid rod block copolymers.

Table 5.2: Summary of block copolymer structure in the semicrystalline state

Sample	$f_{P3EHT}{}^{a}$	d (nm)	d_{3EHT} (nm)	S (nm^2)^b
P3EHT-PMA (12.3)	0.40	25	9.8	0.75
P3EHT-PMA (17.0)	0.47	36	13.9	0.72
P3EHT-PMA (37.8)	0.41	65	24.5	0.88

[a] As determined by ^{1}H NMR spectroscopy of the purified block copolymer. Volume fractions presented for semicrystalline phase using the density (1.07 g/cm^3) presented in previous work for the homopolymer.[11] [b] The interfacial area per chain calculated from $S = M_n/(N_{Av} \cdot \rho_{P3EHT} \cdot d_{P3EHT})$

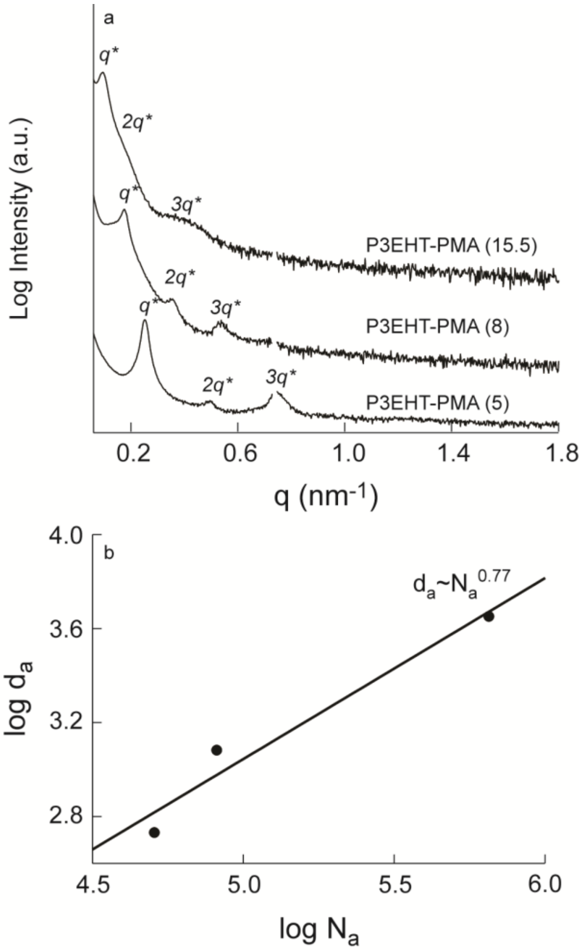

Figure 5.5: Solid state small-angle x-ray scattering of P3EHT-PMA block copolymers

Solid state characterization. (a) Small-angle x-ray scattering line cuts for block copolymers in the solid state. Peaks shift to lower q relative to the melt phase indicating an expansion of the lamellar domain size. Block copolymers retain lamellar morphology upon crystallization. (b) Domain spacing in the melt phase.

of block copolymer domains was determined by small-angle x-ray scattering performed in the flow and load directions of the melt-pressed samples (Figure 5.6). The primary peak for P3EHT-PMA (37.8) was too near the beam stop in this configuration such that the orientation could not be unambiguously determined. However, P3EHT-PMA (12.3) and P3EHT-PMA (17.0) clearly show aligned block copolymer domains upon melt pressing. Load direction patterns were isotropic and exhibited only a single, weak primary peak. In contrast, the flow direction exhibited patterns with multiple higher order peaks and intensity localized parallel to the press axis. Plots of the intensity as a function of angle around the primary peak at 0.32 nm^{-1} for P3EHT-PMA (12.3) and 0.22 nm^{-1} for P3EHT-PMA (17.0) are provided for the flow direction (Figure 5.6c and f). While the load direction shows low scattering intensity and no angular dependence, the scattered intensity in the flow direction is localized around angles near 90° and 270°. From the 2-D diffraction patterns and azimuthal profiles, it can be inferred lamellae are oriented parallel to the applied load.

While the preferential ordering of block copolymer domains is evident from the SAXS data, the orientation of crystallites within these domains is determined with WAXS for samples crystallized from the inhomogeneous melt at 45°C. For clarity, we will discuss crystallite orientation in the lowest molecular weight sample as the degree of crystallinity in these samples is highest. WAXS patterns (Figure 5.7a) in the load direction are nearly identical to that of P3EHT homopolymer suggesting isotropic orientation of crystallites. Though a small degree of anisotropy appears in the intensity as a function of azimuthal angle (Figure 5.7c), this appears to be due to noise as any orientation in the unit cell should be at least two-fold symmetric and the difference in intensities is small. In contrast, the peaks in the flow direction (Figure 5.7b) are highly localized at orientations perpendicular to the block copolymer lamellar interfaces. Profiles of the intensity as a function of angle around both the (100) and (010) reflections (Figure 5.7d and e) support this assertion. No splitting is observed in the azimuthal profiles indicating that both crystalline axes are orienting perpendicular to the lamellar interfaces with no tilt angle. Additionally, diffraction measurements performed with a slightly longer sample to detector distance clearly show both block copolymer scattering and the (100) dimension to be centered at exactly 90° to each other. From the localization of intensity, the crystallites are oriented with stems perpendicular to the interface. This orientational assignment is further confirmed when the 2-D pattern is compared with a fiber pattern obtained by tensile drawing of P3EHT from the melt in which diffraction peaks for the (100), (010), and mixed peaks are present perpendicular to the draw axis.

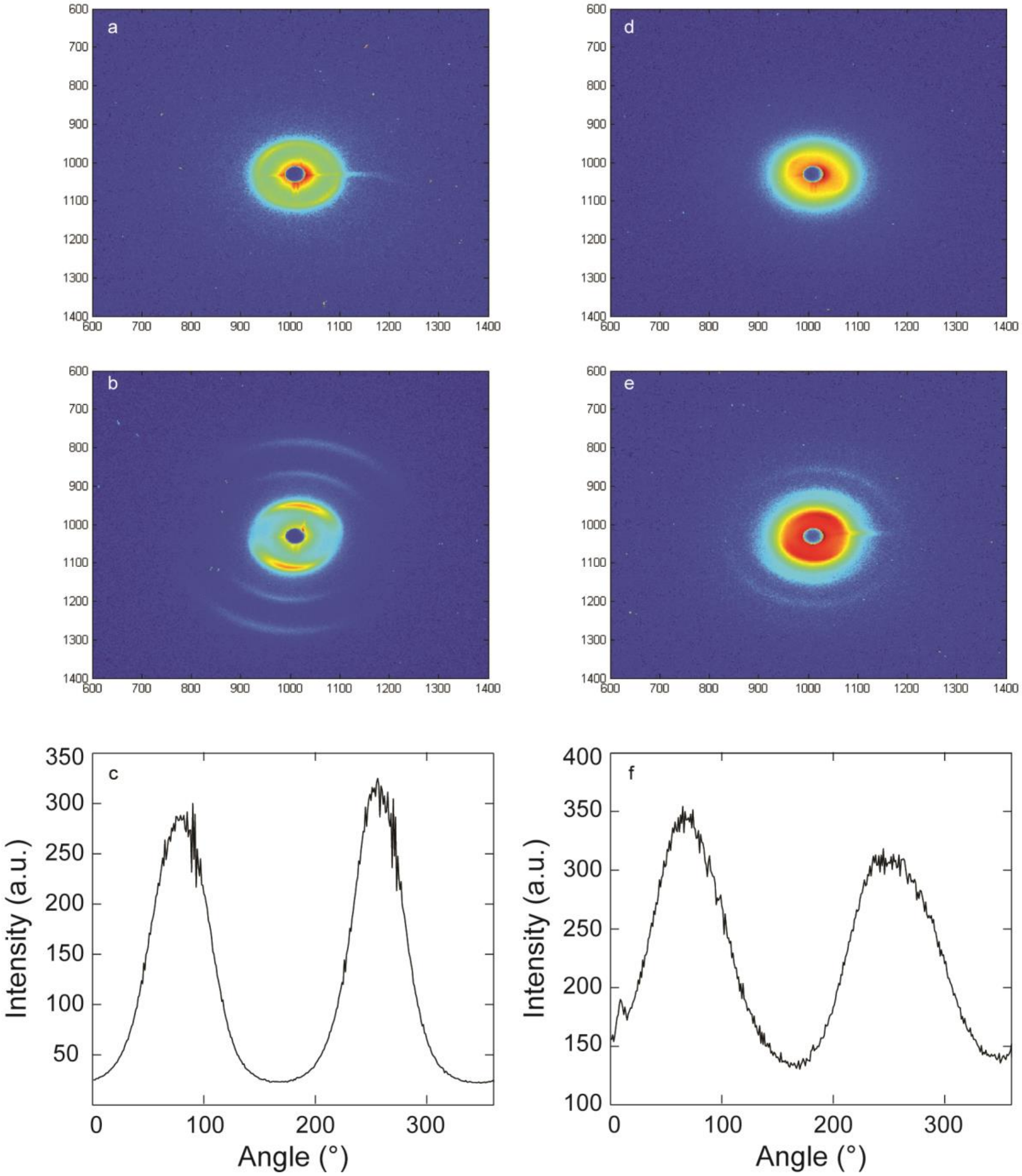

Figure 5.6: 2-D small-angle x-ray scattering patterns

2-D SAXS patterns in the load and flow directions with samples oriented with press axis approximately 90°. (a)-(c) Load, flow, and azimuthal intensity around the primary peak for P3EHT-PMA (12.3). (d)-(f) Load, flow, and azimuthal intensity around primary peak for P3EHT-PMA (17.0). Both block copolymers show minimal diffraction in the load directions, but strong scattering in the flow with multiple higher order peaks present as well. The intensity is primarily centered about 90° and 270° indicating that lamellar are oriented with lamellae parallel to the load.

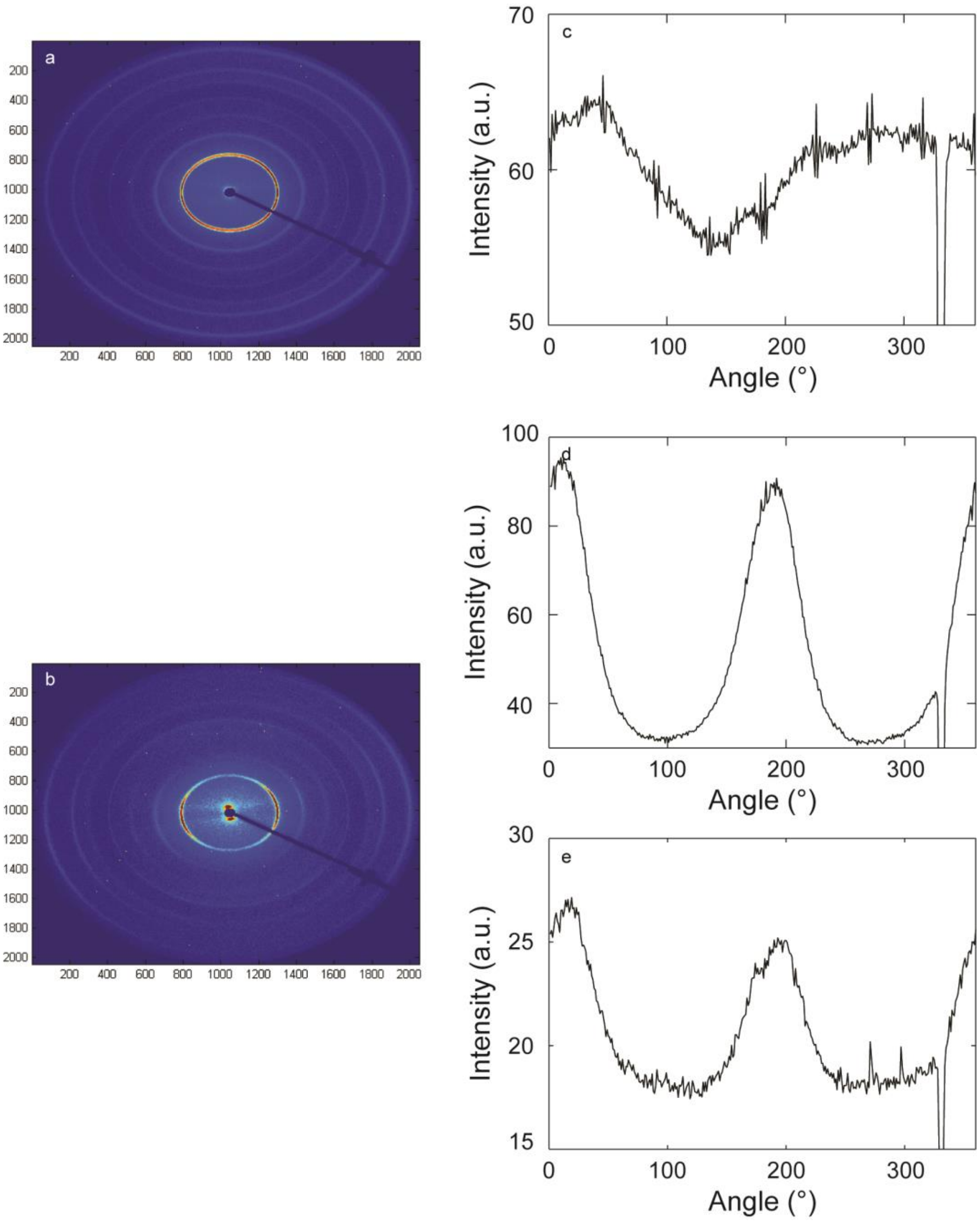

Figure 5.7: 2-D wide-angle x-ray scattering patterns

2-D WAXS patterns of P3EHT-PMA (12.3) in the (a) load and (b) flow directions in approximately the same orientation as samples in Figure 5.6. While the load direction is isotropic, the flow direction shows strong anisotropy along the horizontal. Additionally, in (b), at small angles, scattering arising from the block copolymer domains can be observed to be anisotropic and perpendicular to that of peaks at higher angles corresponding to the crystalline unit cell. (c) Azimuthal intensity around the (100) in the load direction. The azimuthal intensity around the (d) (100) and I (010) in the flow direction exhibits strong anisotropy in the intensity around 0° and 180°, perpendicular to the orientation found in SAXS.

5.3.3 Chain Folding in Confinement

The perpendicular orientation observed in the WAXS has been treated theoretically, and chain folding in the semicrystalline state has been determined to be an equilibrium requirement that decreases the entropic penalty for stretching the amorphous block.[71-72] Although large degrees of chain folding has been observed in semicrystalline block copolymers in the past,[73-74] another class of semiflexible polymers, polypeptides block copolymers, show that the number of chain folds depends on stiffness as well as the chain architecture.[75-76] Importantly, this interplay between chain stiffness and the entropy of stretching the amorphous polymer can define the interfacial area in block copolymer lamellae.

Calculation of chain folding has been presented from simple geometric arguments as a ratio of the area occupied per chain at the block copolymer interface and the cross-sectional area occupied per chain in the crystalline phase.[73] Without knowing the exact crystal structure of P3EHT, we cannot calculate this ratio exactly. However, the crystal structure has been solved for P3HT, and although the area per chain is expected to be larger for P3EHT due to the increase in the unit cell dimensions, from the density measured in the solid state for comparable degrees of crystallinity (1.07 compared to 1.1 g/cm^3),[77] the difference in the density of the crystalline phase (and subsequently the difference in the area occupied per chain in the crystalline phase) is expected to be small. The interfacial areas in the semicrystaline state are presented in Table 2. The values do not vary greatly, though the largest molecular weight polymer does exhibit an increase from ~0.75 to 0.9 nm^2. The cross-sectional area of P3HT using the orthorhombic unit cell from literature[78] is 0.64 nm^2, which when compared with the interfacial areas per chain calculated from the SAXS data suggest that the tethered chain ends do not occupy enough area to accommodate a folded structure. Therefore, crystallization must proceed between adjacent molecules tethered at the block copolymer interface. This picture is consistent with the observation that the chains are highly stretched in the melt (from scaling arguments in the melt) and underscores the importance of understanding the structure of the inhomogeneous melt.

5.4 Conclusions

Block copolymers of poly(3-(2-ethylhexyl)thiophene)-*b*-poly(methyl acrylate) self-assemble into alternating lamellae in the melt, the structure of which confines crystallization of the thiophene moiety to sub-100 nm domains. In this phase, the 3EHT chains adopt highly stretched, apparent from the nearly linear domain scaling with the overall degree of polymerization as well as by comparison of the contour length with the domain size. Such scaling is common in rod-coil block copolymers, though from the chain dimensions of the polymers used in this study, the 3EHT chains should be classified as semiflexible. From SCFT models, the domain scaling of semiflexible block copolymers in the melt should scale in the same manner as predicted by the strong segregation limit ($d \sim N^{2/3}$), suggesting that multiple forces may be resulting in larger than expected scaling exponent.[79] It is proposed that this highly stretched state reduces the entropic driving force for melting, increasing the melting transition temperature in some block copolymers. Furthermore, crystallization from the inhomogeneous melt leads to an orientation in which crystallite stems are perpendicular to the block copolymer lamellar interface. We propose that this orientation proceeds as a direct consequence of the highly stretched nature of thiophene chains and the subsequent chain crowding near the block copolymer interface.

Acknowledgements. This material is based upon work supported by the National Science Foundation under Grant No. 1206296. X-ray scattering was performed at beam line 1-4 at the Stanford Synchrotron Radiation Lightsource, a Directorate of SLAC National Accelerator Laboratory and an Office of Science User Facility operated for the U.S. Department of Energy Office of Science by Stanford University and beam line 7.3.3 of the Advanced Light Source (ALS) at Lawrence Berkeley National Laboratory. We thank Dr. Bryan Beckingham for helpful discussion.

5.8 References and Notes

1. Segalman, R. A.; McCulloch, B.; Kirmayer, S.; Urban, J. J. Block Copolymers for Organic Optoelectronics. *Macromolecules* **2009,** *42* (23), 9205.

2. Yang, Y.; Mielczarek, K.; Aryal, M.; Zakhidov, A.; Hu, W. Nanoimprinted Polymer Solar Cell. *ACS Nano* **2012,** *6* (4), 2877.

3. Leibler, L. Theory of Microphase Separation in Block Copolymers. *Macromolecules* **1980,** *13*, 1602.

4. Bates, F. S.; Fredrickson, G. H. Block Copolymer Thermodynamics: Theory and Experiment. *Annu Rev Phys Chem* **1990,** *41*, 525.

5. Hamley, I. W., *The Physics of Block Copolymers*, Oxford University Press, Inc.: New York, 1998.

6. Cohen, R. E.; Cheng, P. L.; Douzinas, K. C.; Kofinas, P.; Berney, C. V. Path-dependent Morphologies of a Diblock Copolymer of Polystyrene/Hydrogenated Polybutadiene. *Macromolecules* **1990,** *23* (1), 324.

7. Loo, Y. L.; Register, R. A.; Ryan, A. J. Modes of Crystallization in Block Copolymer Microdomains: Breakout, Template, and Confined. *Macromolecules* **2002,** *35* (6), 2365.

8. Loo, Y. L.; Register, R. A., Crystallization within Block Copolymer Mesophases. In *Development in Block Copolymer Science and Technology*, Hamley, I. W., Ed. John Wiley & Sons, Ltd.: Chichester, 2004; pp 213.

9. He, W. N.; Xu, J. T. Crystallization assisted self-assembly of semicrystalline block copolymers. *Prog Polym Sci* **2012,** *37*, 1350.

10. Ho, V.; Boudouris, B. W.; McCulloch, B. L.; Shuttle, C. G.; Burkhardt, M.; Chabinyc, M. L.; Segalman, R. A. Poly(3-alkylthiophene) Diblock Copolymers with Ordered Microstructures and Continuous Semiconducting Pathways. *J Am Chem Soc* **2011,** *133* (24), 9270.

11. Patel, S. N.; Javier, A. E.; Beers, K. M.; Pople, J. A.; Ho, V.; Segalman, R. A.; Balsara, N. P. Morphology and Thermodynamic Properties of a Copolymer with an Electronically Conducting Block: Poly(3-ethylhexylthiophene)-block-poly(ethylene oxide). *Nano Lett* **2012,** *12* (9), 4901.

12. Moon, H. C.; Bae, D.; Kim, J. K. Self-assembly of Poly(3-dodecylthiophene)-block-poly(methyl methacrylate) Copolymers Driven by Competition between Microphase Separation and Crystallization. *Macromolecules* **2012,** *45* (12), 5201.

13. Lin, S. H.; Wu, S. J.; Ho, C. C.; Su, W. F. Rational Design of Versatile Self-Assembly Morphology of Rod-Coil Block Copolymer. *Macromolecules* **2013,** *46* (7), 2725.

14. Osaka, I.; McCullough, R. D. Advances in Molecular Design and Synthesis of Regioregular Polythiophenes. *Accounts Chem Res* **2008,** *41* (9), 1202.

15. Dang, M. T.; Hirsch, L.; Wantz, G. P3HT:PCBM, Best Seller in Polymer Photovoltaic Research. *Adv Mater* **2011,** *23*, 3597.

16. Marcus, R. A. On the Theory of OxidationReduction Reactions Involving Electron Transfer. I. *J Chem Phys* **1956,** *24* (5), 966.

17. Beljonne, D.; Cornil, J.; Coropceanu, V.; da Silva Filho, D. A.; Geskin, V.; Lazzaroni, R.; Leclere, P.; Bredas, J. L., On the Transport, Optical, and Self-Assembly Properties of p-Conjugated Materials: A Combined Theoretical/Experimental Insight. In *Conjugated Polymers: Theory, Synthesis, Properties, and Characterization*, 3rd ed.; Skotheim, T. A.; Reynolds, J. R., Eds. CRC Press: Boca Raton, 2007.

18. Coropceanu, V.; Cornil, J.; da Silva Filho, D. A.; Olivier, Y.; Silbey, R.; Bredas, J. L. Charge Transport in Organic Semiconductors. *Chem Rev* **2007,** *107* (4), 926.

19. Street, R. A.; Northrup, J. E.; Salleo, A. Transport in polycrystalline polymer thin-film transistors. *Phys Rev B* **2005,** *71*, 165202.

20. Xiao, X.; Wang, Z.; Hu, Z.; He, T. Single Crystals of Polythiophene with Different Molecular Conformations Obtained by Tetrahydrofuran Vapor Annealing and Controlling Solvent Evaporation. *J Phys Chem B* **2010,** *114*, 7452.

21. Kim, D. H.; Han, J. T.; Park, Y. D.; Jang, Y.; Cho, J. H.; Hwang, M.; Cho, K. Single-Crystal Polythiophene Microwires Grown by Self-Assembly. *Adv Mater* **2006,** *18*, 719.

22. Sundar, V. C.; Zaumseil, J.; Podzorov, V.; Menard, E.; Willett, R. L.; Someya, T.; Gershenson, M. E.; Rogers, J. A. Elastomeric Transistor Stamps: Reversible Probing of Charge Transport in Organic Crystals. *Science* **2004,** *303*, 1644.

23. da Silva Filho, D. A.; Kim, E. G.; Bredas, J. L. Transport Properties in the Rubrene Crystal: Electronic Coupling and Vibrational Reorganization Energy. *Adv Mater* **2005,** *17* (8), 1072.

24. Anthony, J. E.; Brooks, J. S.; Eaton, D. L.; Parkin, S. R. Functionalized Pentacene: Improved Electronic Properties from Control of Solid-State Order. *J Am Chem Soc* **2001,** *123* (38), 9482.

25. Xia, Y.; Kalihari, V.; Frisbie, C. D. Tetracene air-gap single-crystal field-effect transistors. *Appl Phys Lett* **2007,** *90*, 162196.

26. Tseng, H. R.; Phan, H.; Luo, C.; Wang, M.; Perez, L. A.; Patel, S. N.; Ying, L.; Kramer, E. J.; Nguyen, T. Q.; Bazan, G. C.; Heeger, A. J. *Adv Mater* **2014,** DOI: 10.1002/adma.201305084.

27. Jimison, L. H.; Toney, M. F.; McCulloch, I.; Heeney, M.; Salleo, A. Charge-Transport Anisotropy Due to Grain Boundaries in Directionally Crystallized Thin Films of Regioregular Poly(3-hexylthiophene). *Adv Mater* **2009,** *21*, 1.

28. Hartmann, L.; Tremel, K.; Uttiya, S.; Crossland, E.; Ludwigs, S.; Kayunkid, N.; Vergnat, C.; Brinkmann, M. 2D Versus 3D Crystalline Order in Thin Films of Regioregular Poly(3-hexylthiophene) Oriented by Mechanical Rubbing and Epitaxy. *Adv Funct Mater* **2011,** *21*, 4047.

29. Hirata, E.; Ijitsu, T.; Soen, T.; Hashimoto, T.; Kawai, H. Domain structure and crystalline morphology of AB and ABA type block copolymers of ethylene oxide and isoprene cast from solution. *Polymer* **1974,** *16*, 249.

30. Douzinas, K. C.; Cohen, R. E. Chain Folding in EBEE Semicrystalline Diblock Copolymers. *Macromolecules* **1992,** *25*, 5030.

31. Nojima, S.; Kata, K.; Yamamoto, S.; Ashida, T. Crystallization of Block Copolymers. 1. Small-Angle X-ray Scattering Study of an eCaprolactone-Butadiene Diblock Copolymer. *Macromolecules* **1992,** *25* (8), 2237.

32. Zhu, L.; Cheng, S. Z. D.; Calhoun, B. H.; Ge, Q.; Quirk, R. P.; Thomas, E. L.; Hsiao, B. S.; Yeh, F.; Lotz, B. Crystallization Temperature-Dependent Crystal Orientations within Nanoscale Confined Lamellae of a Self-Assembled Crystalline-Amorphous Diblock Copolymer. *J Am Chem Soc* **2000,** *122*, 5957.

33. Sun, Y. S.; Chung, T. M.; Li, Y. J.; Ho, R. M.; Ko, B. T.; Jeng, U. S.; Lotz, B. Crystalline Polymers in Nanoscale 1D Spatial Confinement. *Macromolecules* **2006,** *39*, 5782.

34. Hamley, I. W.; Fairclough, J. P. A.; Terrill, N. J.; Ryan, A. J.; Lipic, P. M.; Bates, F. S.; Towns-Andrews, E. Crystallization in Oriented Semicrystalline Diblock Copolymers. *Macromolecules* **1996,** *29*, 8835.

35. Ryan, A. J.; Hamley, I. W.; Bras, W.; Bates, F. S. Structure Development in Semicrystalline Diblock Copolymers Cystallizing from the Ordered Melt. *Macromolecules* **1995,** *28*, 3860.

36. Rangarajan, P.; Register, R. A.; Fetters, L. J. Morphology of Semicrystalline Block Copolymers of Ethylene-(Ethylene-alt -propylene). *Macromolecules* **1993,** *26* (17), 4640.

37. Rangarajan, P.; Register, R. A.; Fetters, L. J.; Bras, W.; Naylor, S.; Ryan, A. J. Crystallization of a Weakly Segregated Polyolefin Diblock Copolymer. *Macromolecules* **1995,** *28* (14), 4932.

38. Chen, W. Y.; Zheng, J. X.; Cheng, S. Z. D.; Li, C. Y.; Huang, P.; Zhu, L.; Xiong, H.; Ge, Q.; Guo, Y.; Quirk, R. P.; Lotz, B.; Deng, L.; Wu, C.; Thomas, E. L. Onset of Tethered Chain Overcrowding. *Phys Rev Lett* **2004,** *93*, 028301.

39. Hsiao, M. S.; Zheng, J. X.; Van Horn, R. M.; Quirk, R. P.; Thomas, E. L.; Chen, H. L.; Lotz, B.; Cheng, S. Z. D. Poly(ethylene oxide) Crystal Orientation Change under 1D Nanoscale Confinement using Polystyrene-block-poly(ethylene oxide) Copolymers: Confined Dimension and Reduced Tethering Density Effects. *Macromolecules* **2009,** *42*, 8343.

40. Zheng, J. X.; Xiong, H.; Chen, W. Y.; Lee, K.; Van Horn, R. M.; Quirk, R. P.; Lotz, B.; Thomas, E. L.; Shi, A. C.; Cheng, S. Z. D. Onsets of Tethered Chain Overcrowding and Highly Stretched Brush Regime via Crystalline-Amorphous Diblock Copolymers. *Macromolecules* **2006,** *39*, 641.

41. Fetters, L. J.; Lohse, D. J.; Richter, L. J.; Witten, T. A.; Zirkel, A. Connection between Polymer Molecular Weight, Density, Chain Dimensions, and Melt Viscoelastic Properties. *Macromolecules* **1994,** *27* (17), 4639.

42. Fytas, G.; Nothofer, H. G.; Scherf, U.; Vlassopoulos, D.; Meier, G. Structure and Dynamics of Nondilute Polyfluorene Solutions. *Macromolecules* **2002,** *35* (2), 481.

43. Gettinger, C. L.; Heeger, A. J.; Drake, J. M.; Pine, D. J. A photoluminescence study of poly(phenylene vinylene) derivatives: The effect of intrinsic persistence length. *J Chem Phys* **1994,** *101*, 1673.

44. Gettinger, C. L.; Heeger, A. J.; Drake, J. M.; Pine, D. J. The Effect of Intrinsic Rigidity on the Optical Properties of PPV Derivatives. *Mol Cryst Liq Crys A* **1994,** *256* (1), 507.

45. McCulloch, B.; Ho, V.; Hoarfrost, M. L.; Stanley, C.; Do, C.; Heller, W. T.; Segalman, R. A. Polymer Chain Shape of Poly(3-alkylthiophenes) in Solution Using Small-Angle Neutron Scattering. *Macromolecules* **2013,** *46* (5), 1899.

46. Semenov, A. N.; Vasilenko, S. V. Theory of the nematic-semectic-A transition in a melt of macromolecules consisting of a rigid and a flexible block. *J Exp Theor Phys* **1986,** *63* (1), 70.

47. Reenders, M.; ten Brinke, G. Composition and Orientational Ordering in Rod-Coil Diblock Copolymer Melts. *Macromolecules* **2002,** *35*, 3266.

48. Pryamitsyn, V.; Ganesan, V. Self-assembly of rod-coil block copolymers. *J Chem Phys* **2004,** *120* (12), 5824.

49. Olsen, B. D.; Segalman, R. A. Nonlamellar phases in asymmetric rod-coil block copolymers at increased segregation strengths. *Macromolecules* **2007,** *40* (19), 6922.

50. Olsen, B. D.; Segalman, R. A. Self-assembly of rod-coil block copolymers. *Mat Sci Eng R* **2008,** *62*, 37.

51. Singh, C.; Goulian, M.; Liu, A. J.; Fredrickson, G. H. Phase Behavior of Semiflexible Diblock Copolymers. *Macromolecules* **1994,** *27*, 2974.

52. Kumar, N. A.; Ganesan, V. Communication: Self-assembly of semiflexible-flexible block copolymers. *J Chem Phys* **2012,** *136* (10).

53. Illavsky, J. Nika - software for 2D data reduction. *J Appl Crystallogr* **2012,** *45*, 324.

54. Ho, C. C.; Lee, Y. H.; Dai, C. A.; Segalman, R. A.; Su, W. F. Synthesis and Self-assembly of Poly(diethylhexyloxy-p-phenylenevinylene)-b-poly(methyl methacrylate) Rod-Coil Block Copolymers. *Macromolecules* **2009,** *42* (12), 4208.

55. Lohwasser, R. H.; Thelakkat, M. Synthesis of Amphiphilic Rod–Coil P3HT-b-P4VP Carrying a Long Conjugated Block Using NMRP and Click Chemistry. *Macromolecules* **2012,** *45* (7), 3070.

56. Li, Z.; Ono, R. J.; Wu, Z. Q.; Bielawski, C. W. Synthesis and self-assembly of poly(3-hexylthiophene)-block-poly(acrylic acid). *Chem Commun* **2011,** *47* (197-199).

57. Loewe, R. S.; Ewbank, P. C.; Liu, J.; Zhai, L.; McCullough, R. D. Regioregular, Head-to-Tail Coupled Poly(3-alkylthiophenes) Made Easy by the GRIM Method: Investigation of the Reaction and the Origin of Regioselectivity. *Macromolecules* **2001,** *34* (13), 4324.

58. Jeffries-El, M.; Sauv, G.; McCullough, R. D. Facile Synthesis of End-Functionalized Regioregular Poly(3-alkylthiophene)s via Modified Grignard Metathesis Reaction. *Macromolecules* **2005,** *38* (25), 10346.

59. Ho, V.; Boudouris, B. W.; Segalman, R. A. Tuning Polythiophene Crystallization through Systematic Side Chain Functionalization. *Macromolecules* **2010,** *43* (19), 7895.

60. Boudouris, B. W.; Ho, V.; Jimison, L. H.; Toney, M. F.; Salleo, A.; Segalman, R. A. Real-Time Observation of Poly(3-alkylthiophene) Crystallization and Correlation with Transient Optoelectronic Properties. *Macromolecules* **2011,** *44* (17), 6653.

61. Lemstra, P. J.; Schouten, A. J.; Challa, G. Secondary Crystallization of Isotactic Polystyrene. *J Polym Sci, Part B: Polym Phys* **1974,** *12*, 1565.

62. Strobl, G. Crystallization and melting of bulk polymers: New observations, conclusions and a thermodynamic scheme. *Prog Polym Sci* **2006,** *31*, 398.

63. Heck, B.; Siegenfuhr, S.; Strobl, G.; Thomann, R. A law controlling polymer recrystallization showing up in experiments on s-polypropylene. *Polymer* **2007,** *48*, 1352.

64. Beckingham, B. S.; Ho, V.; Segalman, R. A. **2014,** in preparation.

65. Sakurai, T.; Nojima, S. Significant increase in the melting temperatre of poly(ε-caprolactone) blocks confined in the crystallized lamellar morphology of poly(ε-caprolactone)-block-polyethylene copolymers. *Polym J* **2011,** *43*, 370.

66. Olsen, B. D.; Jang, S. Y.; Luning, J. M.; Segalman, R. A. Higher order liquid crystalline structure in low-polydispersity DEH-PPV. *Macromolecules* **2006,** *39* (13), 4469.

67. Neher, D. Polyfluorene Homopolymers: Conjugated Liquid-Crystalline Polymers for Bright Blue Emission and Polarized Electroluminescence. *Macromol Rapid Comm* **2001,** *22* (17), 1365.

68. The density of amorphous P3EHT was determined by picnometry of a molten sample quenched in liquid nitrogen and brought to room temperature for the measurement. The slow crystallization of P3EHT suggests that the samples should be nearly completely amorphous following this procedure and should not introduce significant error, but we concede that this density of “amorphous” P3EHT should be taken as at best an upper limit on the density.

69. Fetters, L. J.; Lohse, D. J.; Colby, R. H., Chain Dimensions and Entanglement Spacings. In *Physical Properties of Polymer Handbook*, 2nd ed.; Mark, J. E., Ed. Springer: New York, 2007.

70. Semenov, A. N. Contribution to the theory of microphase layering in block-copolymer melts *J Exp Theor Phys* **1985,** *61* (4), 733.

71. DiMarzio, E. A.; Guttman, C. M.; Hoffman, J. D. Calculation of Lamellar Thickness in a Diblock Copolymer, One of Whose Components Is Crystalline. *Macromolecules* **1980,** *13* (5), 1194.

72. Whitmore, M. D.; Noolandi, J. Theory of Crystallizable Block Copolymer Blends. *Macromolecules* **1988,** *21* (5), 1482.

73. Ishikawa, S. Microphase Separation and Crystallization of Crystalline-Amorphous Type Block Copolymer - 8. Calculation of Folding Number in the Crystalline Domain. *Eur Polym J* **1995,** *31* (10), 1005.

74. Ashman, P. C.; Booth, C.; Cooper, D. R.; Price, C. Crystallinity and fusion of ethylene oxide/propylene oxide block copolymers: 2. Type PEP copolymers. *Polymer* **1975,** *16* (12), 897.

75. Douy, A.; Gallot, B. Block copolymers with a polyvinyl and a polypeptide block: factors governing the folding of the polypeptide chains. *Polymer* **1982,** *23* (7), 1039.

76. Łosik, M.; Kubowicz, S.; Smarsly, B.; Schlaad, H. Solid-state structure of polypeptide-based rod-coil block copolymers: Folding of helices. *Eur. Phys. J. E* **2004,** *15* (4), 407.

77. Lee, C. S.; Dadmun, M. D. Important thermodynamic characteristics of poly(3-hexyl thiophene). *Polymer* **2014,** *55* (1), 4.

78. Prosa, T. J.; Winokur, M. J.; Moulton, J.; Smith, P.; Heeger, A. J. X-ray Structural Studies of Poly(3-alkylthiophenes): An Example of an Inverse Comb. *Macromolecules* **1992,** *25*, 4364.

79. Matsen, M. W. Melts of semiflexible diblock copolymer. *J Chem Phys* **1996,** *104* (19), 7758.

Chapter 6: Conclusions and Future Outlook

From the work in this thesis it is clear that although the phase behavior in solid-state is complex, the self-assembly of poly(3-alkylthiophene) (P3AT) containing block copolymers can be understood within the framework of our well-established understanding of block copolymer thermodynamics (Section 1.3.3). In particular, kinetically-trapped nanofibrillar morphologies which have been prevalent in the literature to date can be circumvented if the crystallization temperature of the conjugated unit is controlled in a predictive manner (Chapter 4). This conclusion fits with our well-established understanding of polyethylene, poly(ethylene oxide), and poly(ε-caprolactone) block copolymers, though application of these fundamental concepts to P3AT-containing block copolymers has previously been lacking. From such a fundamental understanding, it can be seen that the self-assembly of future optoelectronically-active systems into periodic nanoscale domains can be realized if the melting transition temperature (and potentially the liquid crystalline clearing temperature) is not prohibitively high. In this way, the probability of achieving ordered microphases other than alternating lamellae can be increased by simply decreasing the melting transition temperature with side chain substitution or copolymerization (Chapter 2), and extension to novel low band gap, donor-acceptor type polymers may be realized in the future as well. However as shown in Chapter 2, care must be taken when controlling the melting transition temperature as the optical band gap and the absorption coefficient in the solid state can be affected by the crystalline structure adopted according to the packing constraints imposed by the sterics of the side chain.

Such exquisite control over the morphology of organic electronic device active layers allows for the development of fundamental structure-property relationships as well as outlets for the introduction of novel functionality to current devices. As the most prevalent example, the ability to control the morphology precisely across the entire active layer and with pure component phases provides idealized structure for examining the nanoscale structure-property relationships in devices. Achieving such a morphology with the current fabrication of bulk heterojunction devices is a difficult, if not impossible, proposition as phase separation is tied intrinsically to crystallization of domains in most currently-used blends. The morphological characterization of bulk heterojuctions is also difficult due to the small length scale of features and short range order, a complication which can be avoided with block copolymers that form ideal nanoscale periodic structures. As has been shown in this thesis (Chapter 4 and 5), structural characterization of semiconducting block copolymers can be easily performed with transmission electron microscopy and x-ray scattering techniques which allows for easy comparison with modeling or theory. Furthermore, block copolymer morphologies may open the window to novel architectures in current organic electronic devices as the functionalities of the nanostructured morphologies is limited only by the feasibility of the chemistry. The partitioning of chemical functionalities within nanometer domains is easily realized as domains will necessarily phase separate into distinct regions providing interdigitated pathways for multiple processes across the active layer.

Though application of the knowledge presented in this work to functional nanostructured devices is tempting, there remain important aspects of both the melt and solid state which need to be further investigated before we are justified in applying our knowledge to arbitrary conjugated systems. In the melt-phase, self-assembly of the polymers in this work represent only one regime for semiflexible-flexible coil block copolymers, namely those which are weakly liquid crystalline. In contrast with the rigid rod-coil work, non-lamellar block copolymer morphologies are observed in P3AT-containing systems as a result of the reduced driving force for orienting molecules within the semiconducting domain. However, theoretical works predict that the phase behavior should be biased towards lamellar interfaces for semiflexible polymers if liquid crystallinity is dominant regardless of chain topology or volume fraction. Specifically, this requires a polymer for which nematic phases are stable over a large region of phase space but which the contour length is comparable to or greater than the persistence length. Importantly, this region of phase space may be populated by many commonly-used semiconducting polymers. Therefore, in order to correctly predict the phase behavior of future semiconducting block copolymers given any combination of values for the strength of liquid crystalline interactions and persistence lengths, one must fundamentally understand each regime.

Although this thesis has presented fundamental design rules for control of solid state order for conjugated-amorphous diblock copolymers in which the non-conjugated block is not optoelectronically-active, much work still needs to be done on systems for which both blocks are semiconducting. Such chemistry is necessary for the fabrication of donor-acceptor block copolymers for OPV applications or *p*- and *n*-type semiconductors for OFETs, but the challenges presented in Section 1.2 are compounded when examining semiconducting-semiconducting systems. In this conditions, though the conformational symmetry will be reduced, the crystallization temperatures (if semicrystalline polymers are used) of both blocks will become relevant for the final morphology. Furthermore, as was observed in Chapter 5, the chain shape of the melt from which the polymer crystallizes affects the structure and properties, and pinning the interfacial area with the crystalline structure of one of the components may affect the solidification (both degree of crystallization and the orientation) of the second crystallizing block. In some cases, this templating has been observed to hinder the crystallization, but in others, the interface acts as a nucleation point for growth of the second block. Moreover, it is unclear if and how the relative crystallite orientation at this interface would affect exciton or charge transfer between semiconducting domains.

In spite of the complexities that may arise in exploration of this class of molecules, this thesis underscores that our current understanding of non-conjugated crystalline polymers can be readily applied to optoelectronically-active materials as long as the fundamental parameters (*e.g.* persistence length, thermal transition temperatures) that define the polymers are considered in advance. It is hoped that in the future the organic electronics community will adopt such concepts as polymer chain shape, crystallization, and phase separation, well-established in the polymer physics literature, to help understand and manipulate the structure of organic electronic active layers at multiple length scales.